

Chapter 1

General introduction

Photonic technology requires the development of new materials to generate, guide, switch, multiplex, and amplify light. In this thesis the incorporation of erbium ions in silica using ion implantation is studied. Trivalent erbium shows an optical transition at $1.54\ \mu\text{m}$, an important optical telecommunication wavelength. Erbium implantation may be used to dope planar optical waveguides in order to fabricate an optical amplifier operating at $1.54\ \mu\text{m}$. Several new and unexpected phenomena related to this new technology of ‘optical doping’ by ion implantation are studied.

1. Introduction

Photonic technology is emerging in the present information era. By using optical data transfer through optical fibers, transmission rates as high as 10 Gbit/s can be achieved [1], much higher than can be attained by using electronic transmission. The enormous bandwidth of optical communication systems enables the development of the information superhighway system, which will have a large impact on the future information society. This new technology requires the synthesis of new materials for generation, guiding, switching, multiplexing and amplification of light.

Erbium-doped materials have gained an important role in photonic telecommunication technology [1,2]. In the trivalent state, Er shows a broad optical transition around $1.54\ \mu\text{m}$ [3], coinciding with the wavelength at which silica-based optical fibers have their minimum transmission loss (see Fig. 1). Therefore, Er is ideally suited as an active element for the generation and amplification of light in telecommunication systems. The technological importance of this concept is illustrated by the fact that Er-doped fiber amplifiers (EDFA) became a commercially available product only three years after the first demonstration of EDFAs operating at $1.54\ \mu\text{m}$ [5,6]. While optical fibers and fiber amplifiers are used for long-distance communication, planar integrated optics may be used for optical signal processing on a local scale (see Fig. 2) [7]. Such processing may include splitting, switching, and multiplexing of signals. The advantages of optical communication would be man-

FIGURE 1: Transmission loss spectrum through a standard silica-based optical fiber, with a GeO₂-doped core. (From Miya *et al.* Ref. 4). The minimum loss is located around 1.5 μm . This wavelength coincides with an optical transition in the Er³⁺ ion.

tained throughout the entire network, if these tasks could be done all in the optical domain. An example of a planar device that may find an important application is an optical amplifier: an integrated planar amplifier with a moderate gain of a factor 2 (3 dB) could compensate for the intensity decrease in a 50-50 Y-branch splitter.

Various methods have been used to fabricate Er-doped planar optical waveguides, and in some cases optical gain has been demonstrated [8-12]. This thesis reports on the use of ion implantation for doping waveguides with optically active Er. Ion implantation is a widely used technique in silicon-based micro-electronic technology, since it offers excellent control over the position and dose of the introduced dopants [13]. Because ion implantation is a non-equilibrium technique, novel structures and metastable phases and solutions may be fabricated. Dopant concentrations above the solubility limit can be incorporated in a host material, which in the case of optical doping means that optical gain may be achieved in shorter device lengths. Ion implantation can be used to dope standard substrates for which the technology for waveguide fabrication has already been developed. Analogous to electrical doping, we refer to the incorporation of optically active elements in optical materials as ‘optical doping’.

The work in this thesis was performed using sodalime silicate glass as host material. High concentrations of Er can be incorporated in this multicomponent glass due to the high concentration of non-bridging oxygen [14]. Effects related to the high Er concentration, such as Er-Er interactions, are studied in this thesis. Fiber-compatible optical waveguides can be fabricated in sodalime glass by the Na⁺ \leftrightarrow K⁺ ion exchange process [15-17] using a KNO₃ melt. In this process, Na⁺ ions in a 6 μm

FIGURE 2: View of a hybrid planar optical waveguide structure on silicon. (From Henry *et al.* Ref. 7). This is an example of a transceiver for bidirectional communication, which includes silica waveguides, Y-splitters, detectors, a laser, fiber alignment utilities and electrical contacts. The 3 dB intensity decrease in the 50 % splitter branches may be compensated for using an integrated optical amplifier.

thick surface layer are replaced by K^+ ions, which increase the refractive index. In order to dope silica with Er ions to such depths, implantation energies up to several MeV are required. This is a new energy regime for ion implantation research, and in this thesis several new and unexpected phenomena related to the use of such high irradiation energies are investigated.

2. Physics of trivalent erbium ions

Erbium is a rare-earth metal, with atomic number 68. The electronic structure of Er^{3+} is $[Xe]4f^{11}$, of which the partially filled $4f$ shell is electronically shielded by the outerlying filled $5s^25p^6$ shells from the Xe configuration [3]. Figure 3 shows the energy levels of the free Er^{3+} ion, which arise from spin-spin and spin-orbit coupling in different possible electron configurations within the $4f$ shell. These degenerate levels all have equal parity. Hence, electric dipole transitions (i.e. transitions involving one photon) are not allowed in the free ion.

When Er^{3+} is incorporated in a solid, the presence of the surrounding atoms weakly perturbs the $4f$ states [3]. Due to the Stark effect, the degenerate levels split into manifolds (see Fig. 3). Moreover, mixing with states of opposite parity now makes electric dipole transitions weakly allowed. The spontaneous emission lifetime of the ${}^4I_{13/2} \rightarrow {}^4I_{15/2}$ transition at $1.54 \mu\text{m}$ of Er^{3+} in a solid can be as long as ~ 10 ms. The measured lifetime, however, strongly depends on the presence of impurities and defects in the host.

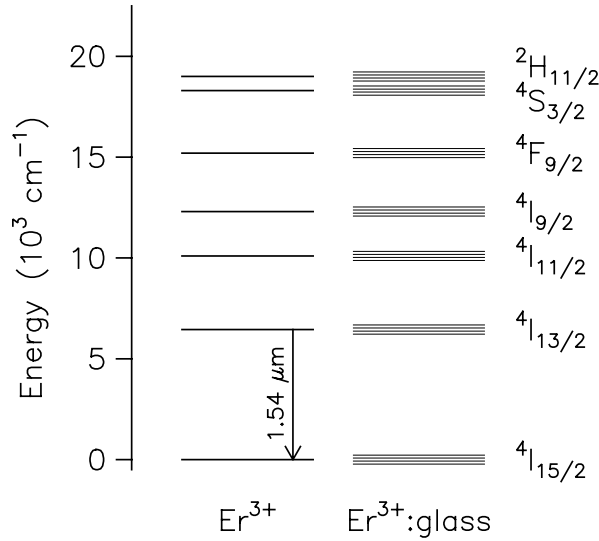


FIGURE 3: Energy levels of the free Er^{3+} ion, and of Er^{3+} incorporated in a solid, in which case the degenerate levels are Stark-split into manifolds. The levels are indicated by Russel-Saunders notation (see Ref. 3).

After excitation in one of the higher lying states (for instance $4\text{I}_{11/2}$), the metastable $4\text{I}_{13/2}$ manifold is rapidly populated via non-radiative relaxation. From here, stimulated emission through a transition to the ground state can cause amplification of light at $1.54 \mu\text{m}$. This is a three-level amplification scheme, of which the drawback is that population left in the ground state absorbs signal light. It is therefore important that the luminescence lifetime of the $4\text{I}_{13/2}$ manifold is long, so that full population inversion can be reached using standard continuous wave diode pump lasers. The pump efficiency may be further improved when the Er is incorporated in an optical waveguide in which the optical modes are confined to a diameter of typically several micrometers.

3. Erbium ion implantation

When an energetic ion enters a solid, energy is deposited in electronic excitations and atomic displacements. In silica, these processes cause structural damage in the ring network [18-21]. A large amount of research on radiation damage in glass has been performed in the last decades, not only because glass containers are used for storage of radioactive waste materials [18,22], but also due to the recent application of silica glass in optical fiber data transmission systems.

For optical doping it is important to avoid irradiation damage or to remove it. Damage can couple to the Er^{3+} ion, and thereby cause non-radiative decay which lowers the Er luminescence lifetime and efficiency [23]. This is disadvantageous in Er-doped optical amplifiers, because the amplifier efficiency and the minimum

amount of pump power needed for amplification directly depend on the luminescence lifetime. The creation and annihilation processes of structural damage that quenches the luminescence are studied in several chapters of this thesis. Erbium photoluminescence is thus employed as a probe of defects in ion irradiated glasses.

We have also used *in-situ* wafer curvature measurements to study defects and structural deformation in silica. With this technique it is possible to determine the mechanical stress in silica during ion irradiation, and a variety of effects can be resolved and quantified. A precise knowledge of these effects is important in optical doping by means of ion implantation, because the building up of mechanical stress during irradiation can result in dramatic macroscopic deformation of silica glass.

4. This thesis

In this thesis, several different aspects of optical doping of silicate glass by erbium ion implantation are investigated.

Part I (Chapters 2 to 6) investigates the optical properties of Er-implanted silicate glass. In Chapter 2, the Er photoluminescence (PL) spectra and lifetimes are studied, as well as the effect of post implantation annealing. It is shown that the density of optically active Er increases with Er implantation fluence, while the PL efficiency decreases. Changes in PL lifetime are attributed to changes in non-radiative decay rate. The value of the radiative decay rate is determined in Chapter 3, where it is found that the PL lifetime of Er that is implanted close to the sample surface, changes when a transparent liquid film is applied to the surface. This is understood in terms of changes in the optical density of states which according to Fermi's Golden Rule determines the radiative decay rate of Er^{3+} .

In Chapter 4 concentration quenching effects, resulting from Er-Er interactions, are studied. Such interactions lead to Er-Er energy migration and quenching at a low density of impurities such as hydroxyl groups. A second Er-Er interaction leading to luminescence quenching, cooperative upconversion, is studied in Chapter 5. Cooperative upconversion occurs when a high density of Er ions is excited, as is the case in Er-doped optical waveguide amplifiers. The effect of upconversion on optical gain is also studied in this chapter. In Chapter 6, the optical gain performance of Er-implanted planar waveguides is discussed, taking into account all the measured parameters in Chapters 2 to 5.

In **Part II** (Chapters 7 and 8) the creation and relaxation of mechanical stress during MeV ion irradiation is studied. Chapter 7 shows that SiO_2 trenches, which are routinely used in industry as implantation masks, dramatically deform and collapse during irradiation with MeV heavy ions. *In-situ* measurements of the curvature of thin samples are used to determine the mechanical stress in the irradiated oxide. It is shown that SiO_2 becomes soft under an ion beam, resulting in viscous flow at room temperature, and that an anisotropic in-plane expansion effect is present. In

Chapter 8, a systematic study is described in order to understand the microscopic mechanisms of these phenomena.

The work described in this thesis provides the first systematic study of materials parameters related to optical doping of silica glass by ion implantation, with special emphasis on the possible fabrication of an Er-doped planar optical amplifier. Some of the results will be relevant for other waveguide materials and other rare earths as well.

References

- [1] A. M. Glass, *Physics Today* **46** (10), 34 (1993).
- [2] E. Desurvire, *Physics Today* **47** (1), 20 (1994).
- [3] S. Hübner, *Optical Spectra of Transparent Rare-Earth Compounds* (Academic Press, New York, 1978).
- [4] T. Miya, Y. Terunuma, T. Hosaka, T. Miyashita, *Electron. Lett.* **15**, 106 (1979).
- [5] E. Desurvire, J. R. Simpson, and P. C. Becker, *Opt. Lett.* **12**, 888 (1987).
- [6] R. J. Mears, L. Reekie, I. M. Jauncey, and D. N. Payne, *Electron. Lett.* **23**, 1026 (1987).
- [7] C. H. Henry, G. E. Blonder, and R. F. Kazarinov, *J. Lightwave Technol.* **7**, 1530 (1989).
- [8] J. Shmulovich, Y. H. Wong, G. Nykolak, P. C. Becker, R. Adar, A. J. Bruce, D. J. Muehlner, G. Adams, and M. Fishteyn, OSA Optical Amplifier Meeting, 1993, PD18-1.
- [9] T. Kitagawa, K. Hattori, K. Shuto, M. Yasu, M. Kobayashi, and M. Horiguchi, Tech. Dig. Topical Meeting on Optical Amplifiers and Applications, Santa Fe, NM, 1992, PD-1; T. Kitagawa, K. Hattori, M. Shimizu, Y. Ohmori, M. Kobayashi, and M. Horiguchi, *Electron. Lett.* **28**, 1818 (1992).
- [10] K. Shuto, K. Hattori, T. Kitagawa, and M. Horiguchi, Proc. 19th Europ. Conf. on Opt. Comm., Montreux, Switzerland, 1993, 53.
- [11] T. Feuchter, E. K. Mwarania, J. Wang, L. Reekie, and J. S. Williams, *IEEE Phot. Techn. Letts.* **4**, 542 (1992).
- [12] P. Becker, R. Brinkmann, M. Dinand, W. Sohler, and H. Suche, *Appl. Phys. Lett.* **61**, 1257 (1992).
- [13] *Handbook of Ion Implantation and Technology*, edited by J. F. Ziegler, (North Holland, Amsterdam, 1992).
- [14] W. J. Miniscalco, *J. Lightwave Technol.* **9**, 234 (1991).
- [15] R. V. Ramaswamy, and R. Srivastava, *J. Lightwave Technol.* **6**, 984 (1988).
- [16] J. J. G. M. van der Tol, J. W. Verhoof, M. B. J. Diemeer, and E. C. M. Pennings, *Electron. Lett.* **27**, 379 (1991).
- [17] S. I. Najafi, *Appl. Opt.* **27**, 3728 (1988).
- [18] Hj. Matzke, in *Ion Beam Modification of Insulators*, edited by P. Mazzoldi and

- G. W. Arnold (Elsevier, Amsterdam, 1987), Chapter 12.
- [19] R. A. B. Devine, Nucl. Instrum. Methods **B91**, 378 (1994).
- [20] W. Primak, *Studies in Radiation Effects in Solids* (Gordon and Breach, New York, 1975), Volume 4.
- [21] P. Mazzoldi and G. W. Arnold, in *Ion Beam Modification of Insulators*, edited by P. Mazzoldi and G. W. Arnold (Elsevier, Amsterdam, 1987), Chapter 5.
- [22] B. Grambow, MRS Bulletin, **XIX**, No. 12 (1994), p20-23.
- [23] A. Polman and J. M. Poate, J. Appl. Phys. **73**, 1669 (1993).

Part I

Optical properties

Chapter 2

Erbium ion implantation in sodalime silicate glass

Sodalime silicate glass has been implanted with 500 keV Er ions at fluences between 8.6×10^{14} and 1.8×10^{16} /cm², with the aim to optically dope the material in the near surface region. The ion range was 100 nm, and Er concentrations in the range of 0.09-1.9 at.% were obtained. The characteristic photoluminescence (PL) of Er³⁺ around 1.54 μ m is observed at room temperature in as-implanted glass. The PL intensity increases by an order of magnitude after annealing above 500°C, as a result of annihilation of implantation-induced defects. Annealing causes an increase in PL lifetime. As a function of Er fluence, the PL intensity first increases, but levels off above $\sim 6 \times 10^{15}$ Er/cm² (~ 0.6 at.% Er peak concentration). The PL lifetime decreases from 13 to 1.5 ms for increasing Er concentration. The decrease in PL efficiency with concentration is attributed to concentration quenching caused by Er-Er interactions. For high Er concentrations and high pump intensities (~ 3 kW/cm²) an additional, intensity dependent quenching mechanism (possibly cooperative upconversion) is observed.

1. Introduction

Erbium-doped materials have recently become of great interest because of their use as an optical gain medium [1]. Erbium shows an optical transition (intra-4*f*) around 1.5 μ m (Fig. 1), a standard wavelength in silica-based optical fiber communication systems. Optical fibers have been doped with Er to fabricate lasers, and in 1987 the first Er-doped fiber amplifiers operating around 1.5 μ m were reported [2]. While fiber-compatibility is important for long-distance communication systems, on a local scale where optical switching and multiplexing are performed using *planar* waveguide structures [3], it would be desirable to integrate a planar Er-based amplifier. For example, a planar amplifier with a moderate gain (~ 3 dB) could compensate for the intensity decrease in a one-to-two beam splitter.

Various methods have been used to fabricate Er-doped planar silica waveguides,

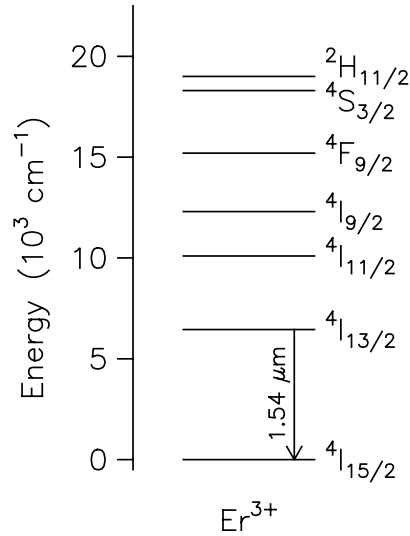


FIGURE 1: Energy-level diagram of the Er^{3+} free ion (see Ref. 12). When Er^{3+} is incorporated in a solid, the levels are split into manifolds due to the Stark effect.

and in some cases optical gain has been demonstrated [4-6]. We use ion implantation to dope sodalime silicate glass with Er. An important advantage of this glass over other materials is that low-loss fiber-compatible planar waveguides can be fabricated by the relatively simple $\text{Na}^+ \leftrightarrow \text{K}^+$ ion-exchange process [7-10]. A further advantage of using a multi-component glass is that it may accommodate larger concentrations of Er [1,11] than, for example, pure silica in which precipitation effects have been observed at concentrations of 0.1 at.% [12].

In this chapter we investigate 500 keV Er-implanted sodalime silicate glass. The dependencies of photoluminescence spectra, intensity, and lifetime on Er concentration and post-implantation anneal temperature are studied. Annealing above 500°C is required to annihilate the implantation-induced defects. For high Er concentration the luminescence is quenched, possibly due to Er-Er interactions.

2. Experimental

Commercially available sodalime silicate glass (Fisher Premium), 1 mm thick, was implanted at room temperature with 500 keV Er ions. The ion current density on sample was $\sim 0.5 \mu\text{A}/\text{cm}^2$, and the implanted fluences ranged from 8.6×10^{14} to $1.8 \times 10^{16} / \text{cm}^2$. To avoid electrical charging of the glass during ion irradiation, a 420 Å thick Al film was evaporated on the glass surface. It was etched off in a NaOH solution after implantation. Thermal annealing was performed in a tube-furnace at a base pressure below 5×10^{-7} mbar, at temperatures ranging from 300 to 650°C . All anneals were done for one hour.

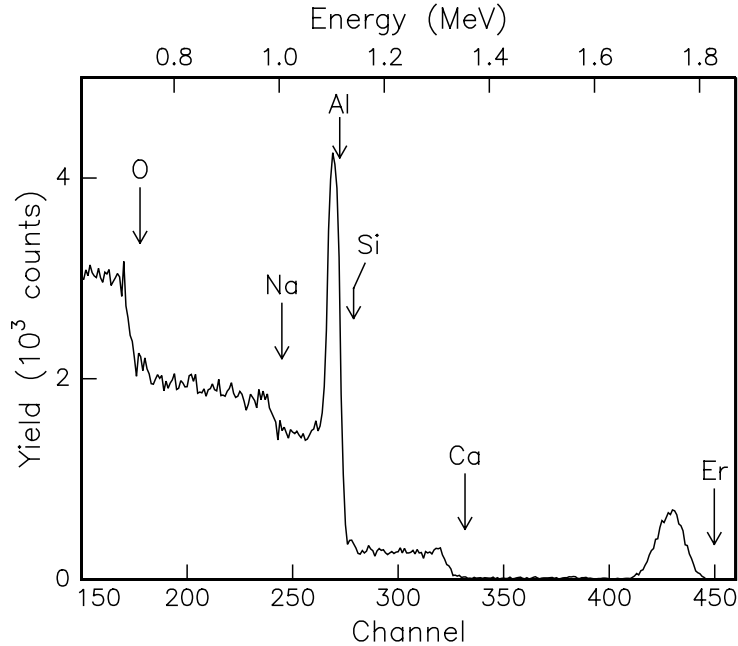


FIGURE 2: RBS spectrum of Er-implanted (5.4×10^{15} Er/cm²) sodalime silicate glass with a 420 Å Al coating. The arrows indicate surface channels of the various glass constituents.

Erbium concentration profiles were determined by Rutherford backscattering spectrometry (RBS) using 2.0 MeV $^4\text{He}^+$ and a scattering angle of 169° . Photoluminescence (PL) spectroscopy was carried out at room temperature, with the 514.5 nm line of an Ar-ion laser as excitation source. This line is absorbed in the $^2H_{11/2}$ manifold of Er^{3+} (see Fig. 1). Powers between 70 and 350 mW were used in a ~ 0.3 mm diameter spot, for which no beam heating of the samples was observed. The luminescence signal was spectrally analysed with a 48-cm monochromator, and detected with a liquid-nitrogen-cooled Ge detector, yielding a spectral resolution of 2.3 nm. The pump beam was chopped at 12 Hz and spectra were recorded using a lock-in amplifier. Time-resolved luminescence decay measurements were performed using a 1.5 ms, 1.4 W pump pulse with a cutoff time shorter than 150 μs . Decay data were recorded and averaged using a digitizing oscilloscope system.

3. Results

Figure 2 shows an RBS spectrum of sodalime silicate glass after implantation of 5.4×10^{15} Er/cm². The sharp peak at channel 269 corresponds to the Al coating. This coating causes a shift over 5 channels of the edges in the spectrum with respect to the indicated surface channels. The composition of the multi-component glass as determined from this spectrum, agrees with the specified composition (in mol%: 72.2

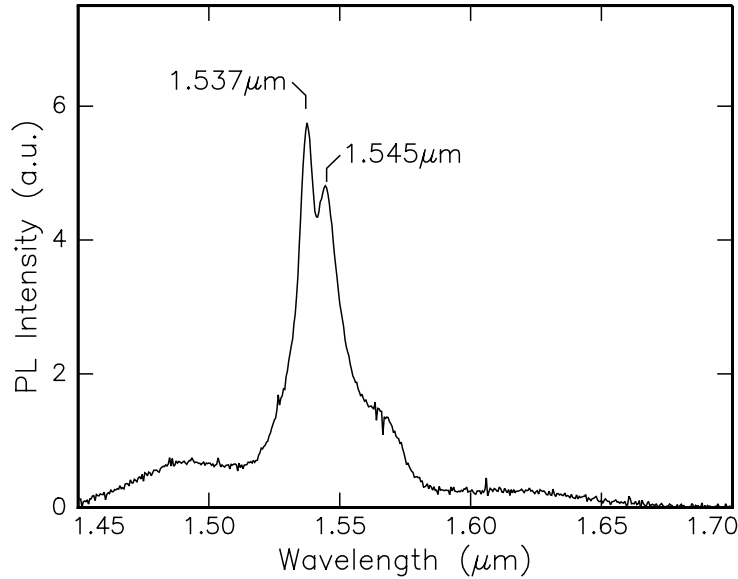


FIGURE 3: Room-temperature photoluminescence spectrum of Er-implanted ($3.7 \times 10^{15} / \text{cm}^2$) sodalime silicate glass after thermal annealing at 512°C . Pump power = 70 mW, $\lambda_{\text{pump}} = 514.5 \text{ nm}$, spectral resolution = 2.3 nm.

SiO_2 , 14.3 Na_2O , 6.4 CaO , 1.2 K_2O , and small quantities of Al_2O_3 , MgO , and others, see Ref. 7). Earlier experiments [13] have shown that ion implantation of alkali silicate glass can cause a depletion of alkali atoms in the surface region. However, no Na loss is observed in our experiments, which may be a consequence of the presence of the Al coating. The Er profile is nearly Gaussian shaped, and peaks at about 100 nm depth from the glass surface, with a full width at half maximum (FWHM) of 90 nm, assuming a sodalime silicate glass density of $7.8 \times 10^{22} \text{ at./cm}^3$. The peak concentration is 0.6 at.%. Samples implanted at other fluences show similarly shaped profiles, with peak concentrations ranging from 0.09 to 1.9 at.%.

Figure 3 shows a PL spectrum of Er-implanted ($3.7 \times 10^{15} / \text{cm}^2$) sodalime silicate glass, after annealing at 512°C for 1 hour. The spectrum shows peaks at the wavelengths (λ) of 1.537 and 1.545 μm and broad shoulders extend from roughly 1.45 to 1.67 μm . This emission is characteristic for the intra- $4f$ transitions between the $^4I_{13/2}$ and $^4I_{15/2}$ manifolds of Er^{3+} (see Fig. 1) [14]. The width of the spectrum is 19 nm FWHM. Spectra were also measured for samples implanted at other fluences and annealed at different temperatures. The shape of these spectra does not significantly deviate from the spectrum shown in Fig. 3.

The PL intensity depends strongly on the temperature of the annealing treatment after implantation. Figure 4 shows peak intensities, measured at $\lambda = 1.537 \mu\text{m}$, for samples annealed at temperatures in the range of $300\text{-}600^\circ\text{C}$. Data are shown for samples with Er peak concentrations of 0.15, 0.4, and 1.9 at.%. As can be seen, unannealed samples show a relatively low PL intensity. Thermal annealing at

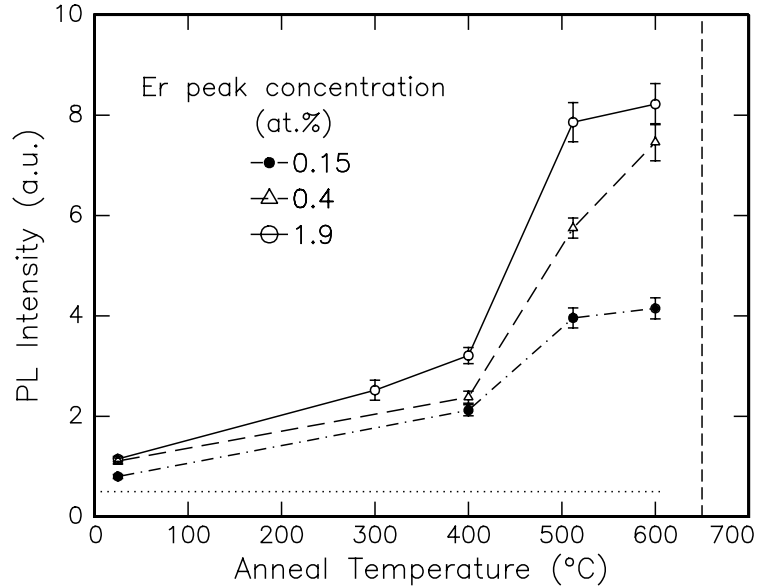


FIGURE 4: Room-temperature photoluminescence peak intensity at $\lambda = 1.537 \mu\text{m}$ as a function of anneal temperature for samples implanted with 1.3 , 3.7 , and $18 \times 10^{15} \text{Er/cm}^2$ (0.15, 0.4, and 1.9 at.% peak concentration). The lines serve as guides for the eye. The dotted line shows the background luminescence of unimplanted samples. The dashed vertical line at 650°C marks the point at which the glass surface starts to deform.

temperatures up to 512°C increases the PL intensity. A smaller further increase is observed for 600°C annealing. It should be noted that the unimplanted glass also shows a very low PL signal, as a result of trace levels of Er in the bulk ($<0.1 \text{ppm}$). This background signal was the same for all samples, and is indicated in Fig. 4 by the dotted line. The dashed vertical line at 650°C indicates the temperature at which macroscopic deformation of the glass was observed. The typical softening point for sodalime glass is 690°C [15].

It is clear from Fig. 4 that the maximum PL intensity after 512°C annealing does not scale linearly with the Er fluence. Increasing the Er peak concentration from 0.15 to 1.9 at.% only doubles the PL intensity. Figure 5 shows the PL intensity of implanted samples annealed at 512°C as a function of Er fluence (open data points). The PL intensity increases almost linearly with fluence for fluences smaller than $2 \times 10^{15} \text{Er/cm}^2$. At higher Er fluences the intensity increase levels off, and a saturation is observed above $\sim 6 \times 10^{15} / \text{cm}^2$, corresponding to an Er peak concentration of $\sim 0.6 \text{at.}\%$.

Figure 6 shows PL decay measurements for samples with Er peak concentrations of 0.15, 0.4, and 1.9 at.%, annealed at 512°C . As can be seen, the PL decay depends strongly on the Er concentration. Firstly, the lifetime decreases with increasing concentration. The e^{-1} decay times for the curves in Fig. 6, together with data for other Er fluences, are plotted as solid data points against the right-hand scale in

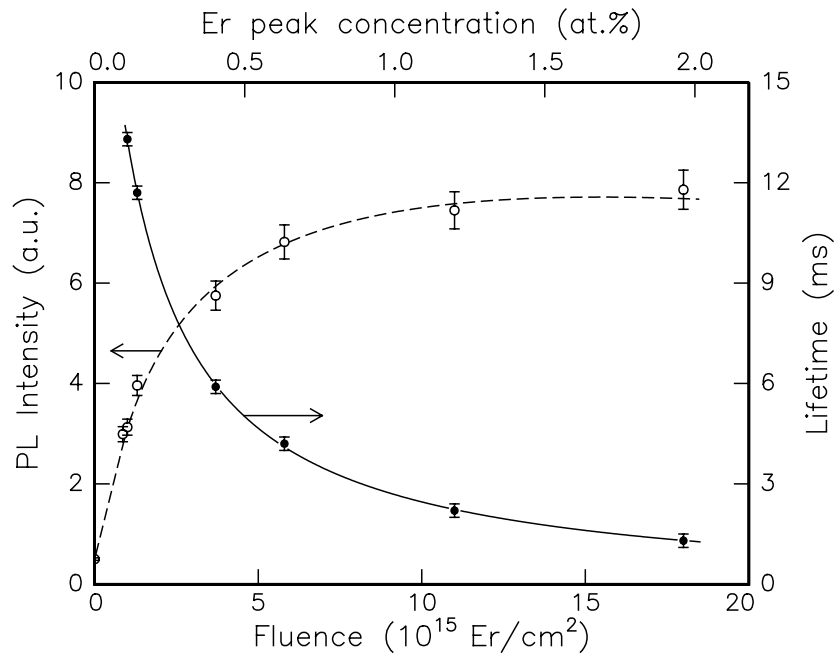


FIGURE 5: Photoluminescence peak intensity (open data points, left axis) and lifetime (solid data points, right axis) at $\lambda = 1.537 \mu\text{m}$ as a function of Er fluence. All samples were annealed at 512°C in vacuum. The Er peak concentrations are indicated on the top axis. The solid line is a guide for the eye, the dashed line is calculated from the solid line using Eq. (1).

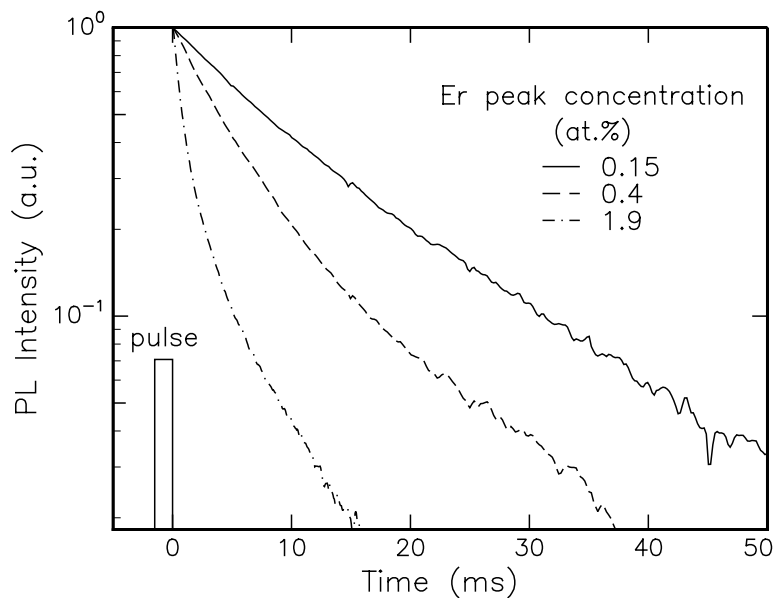


FIGURE 6: PL decay curves after a 1.5 ms excitation pulse. The samples were implanted with 1.3 , 3.7 , and $18 \times 10^{15} \text{ Er/cm}^2$ (0.15, 0.4, and 1.9 at.% peak concentration) and annealed at 512°C . The luminescence intensity at $\lambda = 1.537 \mu\text{m}$ is plotted on a logarithmic scale. The excitation pulse is indicated schematically.

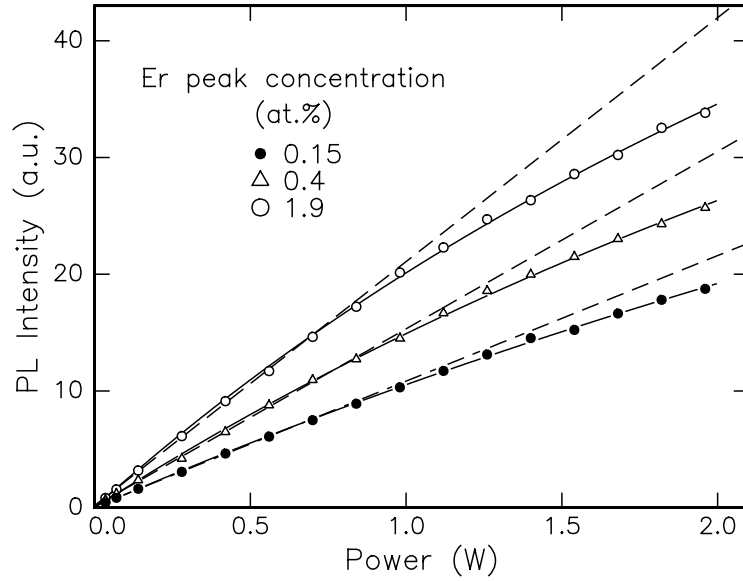


FIGURE 7: PL intensity at $\lambda = 1.537 \mu\text{m}$ measured as function of pump power at 514.5 nm . The samples were implanted with 1.3 , 3.7 , and $18 \times 10^{15} \text{ Er/cm}^2$ and were annealed at 512°C . The dashed lines are linear extrapolations of the first six data points. The solid line drawn for $0.15 \text{ at.}\%$ is calculated using Eq. (2); the other two solid lines guide the eye. A power of 2.0 W corresponds to an intensity of $\sim 3 \text{ kW/cm}^2$.

Fig. 5. Secondly, the shape of the decay curves changes. For low concentrations, the decay is nearly single exponential, but as the Er concentration increases, the curves deviate from single exponential behavior. This is partly a result of the fact that the Er concentration profiles are Gaussian shaped: the PL decay curve is composed of signals with different decay times corresponding to different concentrations. However, attempts to fit the curves in Fig. 6 by integrating over the Gaussian profile using a function relating lifetime to concentration, did not yield results consistent for all decay curves. Therefore, other processes leading to non-exponential decay at high concentration must also play a role. This will be addressed in Chapter 4.

Figure 7 shows the dependence of PL intensity on pump power, measured for three Er peak concentrations (0.15 , 0.4 , and $1.9 \text{ at.}\%$) after annealing at 512°C . The dashed lines show the linear extrapolation of the first six data points. At higher pump intensity the measured curves start to deviate from the linear extrapolation. At 2.0 W (corresponding to an intensity of $\sim 3 \text{ kW/cm}^2$) the signal from the sample with $0.15 \text{ at.}\%$ Er peak concentration is 12% lower than the linear extrapolation. This deviation increases with Er fluence, and for $1.9 \text{ at.}\%$ Er the PL signal is 20% lower than the linear extrapolation. The PL lifetimes (data not shown) do not depend on pump power up to 2.0 W .

4. Discussion

The experimental results show that sodalime silicate glass can be optically doped with Er by ion implantation. The spectral shape (Fig. 3) is a result of transitions between different Stark levels of the $^4I_{13/2}$ and $^4I_{15/2}$ manifolds [14], in combination with homogeneous and inhomogeneous broadening. The $^4I_{13/2}$ manifold is populated through successive non-radiative relaxation from the $^2H_{11/2}$ pump level. The spectrum is broader than observed for Er-implanted pure silica [12], which is characteristic for a multi-component host glass [11]. An advantage of the relatively large spectral width is that optical amplification will be possible over a large bandwidth. The low-wavelength shoulder peaks at $1.48 \mu\text{m}$, a wavelength at which commercial pump lasers are available. This may allow for resonant pumping.

Ion implantation in glass creates structural damage, either by nuclear collisions, or by electronic excitations [13]. Structural defects can quench the parity-forbidden (intra- $4f$) – and therefore long-lived – radiative transition, as they cause non-radiative decay channels [16]. As a result the PL decay time and intensity decrease. In first approximation, for a concentration C_a of optically active (trivalent) Er, the measured lifetime (τ) and PL intensity (I) are given by

$$\frac{1}{\tau} = W_r + W_{nr} \quad \text{and} \quad I \propto \frac{\tau}{\tau_r} C_a, \quad (1)$$

where $W_r = 1/\tau_r$ and W_{nr} are the radiative- and non-radiative decay rates respectively. Assuming that W_r is constant,^a Eq. (1) shows that a high non-radiative decay rate leads to a low lifetime (τ) and a proportionally low PL intensity. This proportionality is observed for the samples used in Fig. 4. For each sample the PL lifetime after annealing at 512°C is twice as long as after 400°C annealing (data not shown), which indeed corresponds to the observed doubling of PL intensity above 400°C . The fact that the changes in intensity fully correspond to the observed lifetime changes implies that the active fraction of Er (C_a) does not change on annealing. The lifetime increase on annealing is attributed to annihilation of ion-beam induced defects in the silicate network [13,16,17]. The required annealing temperature to optimize the Er luminescence ($\sim 500^\circ\text{C}$) is lower than that for Er-implanted pure silica [12]. This may be related to the fact that sodalime silicate glass has a lower transformation temperature than pure silica [15].

The saturation of the PL intensity for increasing Er fluence (Fig. 5) can be attributed to changes in the non-radiative decay rate. The intensity from a sample with $1.8 \times 10^{16} \text{ Er/cm}^2$ is almost equal to the intensity at $6 \times 10^{15} \text{ Er/cm}^2$, although three times more Er was implanted. The lifetime, however, has decreased by a factor of three, thereby keeping the product τC_a in Eq. (1) constant. The dashed line in Fig. 5 was derived from the solid line through the lifetime data, by calculating

^aAn experiment proving that W_r is constant is presented in Chapter 3.

the product τC_a . It shows perfect agreement with the PL intensity data over the full concentration range. The decrease in PL lifetime for high concentration is attributed to processes in which the excitation migrates through the glass by resonant exchange between closely spaced Er ions until a quenching center is met. These effects have been studied in detail in other materials doped with rare earths [18,19] and usually become significant at concentrations above 0.1 at.%. This concentration quenching effect limits the concentration of Er that can be incorporated usefully in sodalime silicate glass. Concentration quenching effects in Er-implanted silica will be investigated in detail in Chapter 4.

For future use of these heavily doped silica glass films in planar optical waveguides, the behavior as a function of pump intensity is an important parameter (Fig. 7). As a first estimate the sublinear increase of PL with pump intensity is a result of the depletion of Er ions in the ground state. The fraction of excited Er ions, N_2 , in a simple two-level system pumped at a rate R is

$$N_2 = \frac{R\tau}{1 + R\tau}, \quad \text{with} \quad R = \frac{I_p}{h\nu} \sigma_a. \quad (2)$$

Here, $h\nu$ is the energy of the pump photons, I_p denotes the pump intensity, and σ_a the absorption cross section. Equation (2) shows that N_2 (and therefore the 1.54- μm PL intensity) is sublinear in I_p , and that the sublinearity is less for samples with shorter lifetime τ . However, Fig. 7 shows the opposite behavior: the samples with a high concentration i.e. short lifetime deviate more from the straight line than the samples with a low concentration, i.e. long lifetime. This suggests that another non-radiative process, which is related to both pump intensity and Er concentration, must be present. One possible explanation is that cooperative upconversion takes place [18], in which energy is transferred non-radiatively from one excited Er ion to a neighbouring excited Er ion, promoting the latter to the $^4I_{9/2}$ level (see Fig. 1). From $^4I_{9/2}$ the most probable decay is back to the $^4I_{13/2}$ manifold, via the $^4I_{11/2}$ level. As a result, the $\lambda = 1.54 \mu\text{m}$ PL is quenched at high pump intensities. Upconversion effects will be studied in more detail in Chapter 5. From the data in Fig. 7 an upper limit of the absorption cross section for Er^{3+} in sodalime silicate glass at 514.5 nm can be obtained by fitting Eq. (2) through the data for the lowest Er concentration. This yields $\sigma_a = 2 \times 10^{-21} \text{ cm}^2$, a typical value for Er in a multi-component glass [11].

5. Conclusions

Erbium implanted (500 keV) sodalime silicate glass shows clear photoluminescence (PL) around 1.54 μm with a relatively large spectral width of 19 nm. Thermal annealing at a temperature above 500°C, causing annihilation of implantation-induced defects, is necessary to optimize PL properties. The PL intensity first increases with Er fluence, but saturates above $\sim 6 \times 10^{15} / \text{cm}^2$. The saturation is explained by a

decrease of PL lifetime with increasing concentration. The lifetime decrease is attributed to concentration quenching, as a result of energy exchange among closely spaced Er ions. The dependence of PL intensity on pump intensity shows evidence for an additional quenching mechanism related to high concentrations of excited Er^{3+} , possibly cooperative upconversion. With these parameters, Er-implanted sodalime silicate glass waveguides with a length of typically several cm may produce optical gain.

References

- [1] B. J. Ainslie, *J. Lightwave Technol.* **9**, 220 (1991).
- [2] E. Desurvire, J. R. Simpson, and P. C. Becker, *Opt. Lett.* **12**, 888 (1987).
- [3] C. H. Henry, G. E. Blonder, and R. F. Kazarinov, *J. Lightwave Technol.* **7**, 1530 (1989).
- [4] J. Shmulovich, A. Wong, Y. H. Wong, P. C. Becker, A. J. Bruce, and R. Adar, *Electron. Lett.* **28**, 1181 (1992).
- [5] T. Kitagawa, K. Hattori, M. Shimizu, Y. Ohmori, and M. Kobayashi, *Electron. Lett.* **27**, 334 (1991).
- [6] T. Kitagawa, K. Hattori, K. Shuto, M. Yasu, M. Kobayashi, and M. Horiguchi, *Tech. Dig. Topical meeting on Optical Amplifiers and their Applications*, Santa Fe, NM, 1992, PD-1; T. Kitagawa, K. Hattori, K. Shuto, M. Yasu, M. Kobayashi, and M. Horiguchi, *Electron. Lett.* **28**, 1818 (1992).
- [7] S. Iraj Najafi, *Appl. Opt.* **27**, 3728 (1988).
- [8] R. V. Ramaswamy, and R. Srivastava, *J. Lightwave Technol.* **6**, 984 (1988).
- [9] M. M. Abouelleil, G. A. Ball, W. L. Nighan, and D. J. Opal, *Opt. Lett.* **16**, 1949 (1991).
- [10] J. J. G. M. van der Tol, J. W. Verhoof, M. B. J. Diemeer, and E. C. M. Pennings, *Electron. Lett.* **27**, 379 (1991).
- [11] W. J. Miniscalco, *J. Lightwave Technol.* **9**, 234 (1991).
- [12] A. Polman, D. C. Jacobson, D. J. Eaglesham, and J. M. Poate, *J. Appl. Phys.* **70**, 3778 (1991).
- [13] P. Mazzoldi and G. W. Arnold in *Ion beam modification of insulators*, P. Mazzoldi and G. W. Arnold, eds. (Elsevier, Amsterdam, 1987), Chapter 5.
- [14] S. Hübner, *Optical Spectra of Transparent Rare-Earth Compounds* (Academic Press, New York, 1978).
- [15] H. Scholze, *Glass* (Springer Verlag, Heidelberg, 1990).
- [16] A. Polman, D. C. Jacobson, and J. M. Poate, *Mat. Res. Soc. Symp. Proc.* **235**, 377 (1992).
- [17] A. Polman, D. C. Jacobson, A. Lidgard, and J. M. Poate, *Nucl. Instrum. Methods* **B59/60**, 1313 (1991).
- [18] J. C. Wright, in *Radiationless Processes in Molecules and Condensed Phases*,

- edited by F. K. Fong, (Springer Verlag, Heidelberg, 1976), Chapter 4.
[19] W. Ryba-Romanowski, J. Lumin. **46**, 163 (1990).

Chapter 3

Measuring and modifying the spontaneous emission rate of erbium near an interface

Erbium implanted sodalime silicate glass was covered with a range of transparent liquids. The spontaneous emission rate of Er^{3+} around $1.54 \mu\text{m}$ shows clear changes depending on the liquid refractive index and Er depth. A rigorous quantum mechanical calculation shows that the effect of the interface on the spontaneous emission rate is fully described by the classical density of optical modes as a function of distance from the interface. The data provide the first direct determination of the radiative transition rate (45 s^{-1}) at $1.54 \mu\text{m}$ of Er^{3+} which is widely used in optical amplifiers.

1. Introduction

Spontaneous emission is interpreted as a consequence of interaction between matter and electromagnetic radiation. Previous experiments, using for instance Rydberg atoms or semiconductor structures, have demonstrated that spontaneous emission can be influenced in cavities or near mirrors [1-7]. In this chapter we will show an extremely simple way to modify the spontaneous emission rate, merely by bringing liquid films with distinctive refractive indices in contact with a silica glass surface which is locally doped with luminescent Er^{3+} ions. Trivalent erbium shows clear photoluminescence (PL) around $1.54 \mu\text{m}$ [8], an important wavelength in optical telecommunication [9].

The theoretical description of spontaneous emission is usually based on concepts from quantum electrodynamics such as vacuum fluctuations and a creation/annihilation formalism. The inclusion of a dielectric interface requires special attention [10]. In this case, the variation in the spontaneous emission rate can be accounted for by the local classical density of states (DOS), which appears in Fermi's Golden Rule. In this chapter, a straight forward calculation of the local density of states is performed,

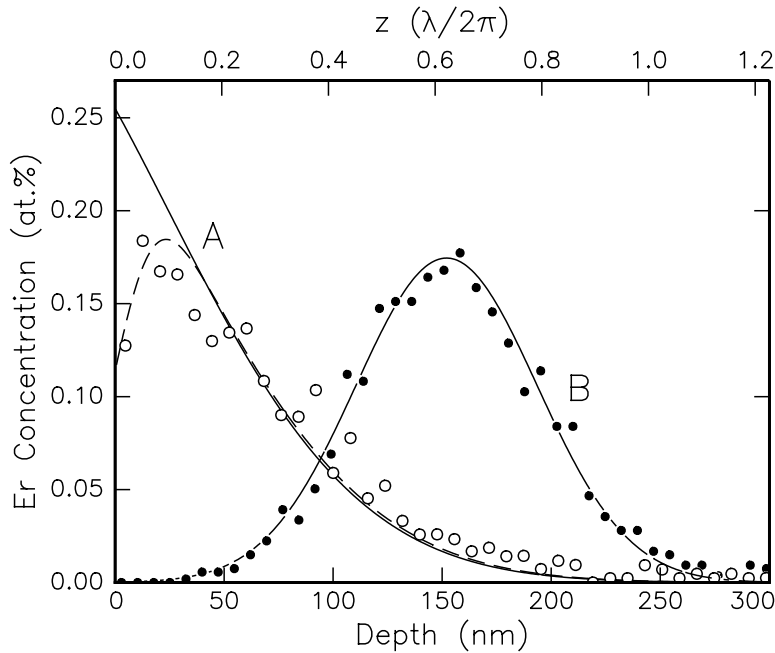


FIGURE 1: Erbium concentration profiles as determined with RBS (open and solid datapoints). The drawn lines are deconvoluted for the detection resolution. The top axis shows the distance in units of $\lambda/2\pi$ (where $\lambda = 1.537\ \mu\text{m}$ is the spontaneous emission wavelength in vacuum).

given the Fresnel equations for transmission and refraction at a dielectric interface. The analysis describes our data on the modification of the spontaneous emission rate as a function of refractive index, and serves to determine for the first time the radiative lifetime of Er in silicate glass. This parameter is of great importance for Er-doped optical gain materials in telecommunication technology.

2. Experiment

Two samples of bulk sodalime silicate glass (refractive index $n_0 = 1.50$) were implanted with 500 keV Er ions. Sample *A* was covered with a 120 nm thick Al film as a stopping layer; sample *B* was not covered during implantation. After implantation, the Al layer was etched off, and a thermal anneal at 512°C was performed. Erbium depth profiles for both samples, as determined using 2 MeV $^4\text{He}^+$ Rutherford backscattering spectrometry (RBS), are shown in Fig. 1. The open data points for sample *A* show a profile peaked at the glass surface, with a half width at half maximum of 70 nm. The measured profile is a convolution of the detection resolution and the actual profile. The drawn line shows the deconvoluted profile, which is discontinuous at the surface where the Er concentration is ~ 0.25 at.%. The solid data points in Fig. 1 show a Gaussian profile for sample *B*, centered at 150 nm depth, and with an Er peak concentration of 0.17 at.%. The full width at half maximum

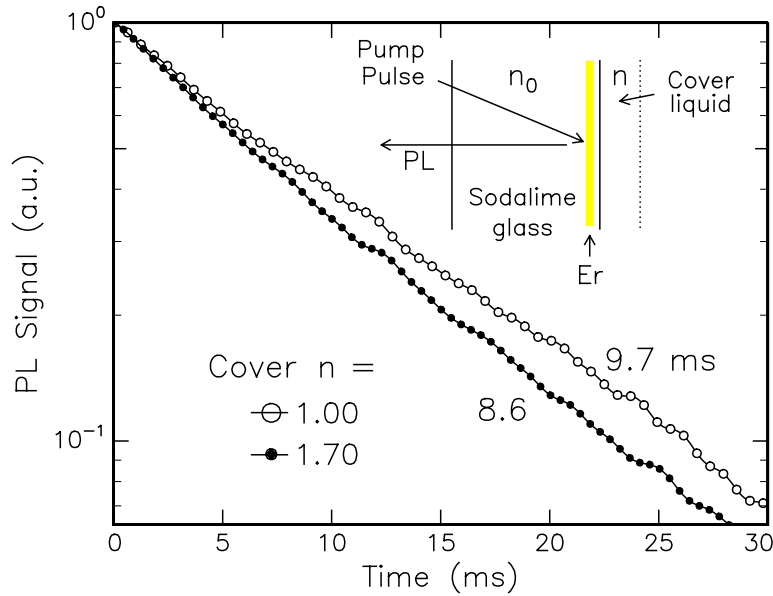


FIGURE 2: Photoluminescence decay traces of the $1.537\ \mu\text{m}$ emission from sample *A* on a logarithmic scale. The solid data points were measured with a methylene-iodide film ($n = 1.70$) covering the surface, the open data points without a covering material. The inset shows how the luminescence signal was collected at the back of the sample, that has the Er-doped front side covered with a liquid with refractive index n .

is 100 nm. Photoluminescence (PL) spectroscopy was carried out at room temperature. The 514.5 nm line of an Ar-ion laser was used to excite the Er, and the luminescence was spectrally analyzed with a monochromator and a liquid-nitrogen cooled Ge detector. Photoluminescence decay measurements were performed after excitation with a 1.5 ms pulse, using a digital averaging oscilloscope. Further details on sample preparation and PL measurements can be found in Chapter 2. Various liquid films, with refractive indices ranging from 1.3 to 1.7, and thicknesses in the order of a mm, were brought in contact with the sample surface on the front, while the luminescence signal was collected on the back side (see inset in Fig. 2).

3. Experimental results

Clear photoluminescence (PL) around $1.54\ \mu\text{m}$, characteristic [8] for the ${}^4I_{13/2} \rightarrow {}^4I_{15/2}$ intra- $4f$ transition of Er^{3+} is observed [11] in both samples *A* and *B*. Figure 2 shows the PL decay measured at $1.537\ \mu\text{m}$ for sample *A* in air (open data points). A single exponential decay, with a $1/e$ decay-time of 9.7 ms is found. The curve marked by solid data points in Fig. 2 shows the PL decay after a film of methylene-iodide with refractive index of $n = 1.70$ was brought in contact with the glass surface. In this case a $1/e$ -time of 8.6 ms is observed, a reduction by 13 %. After the surface

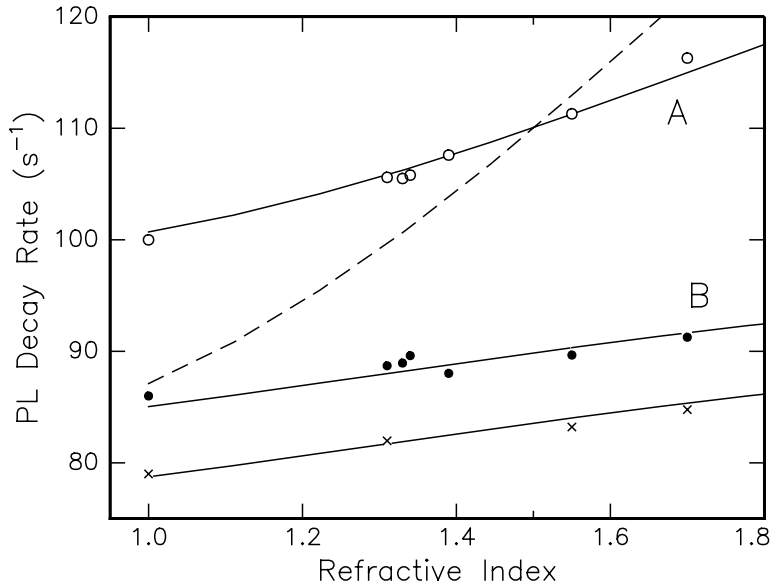


FIGURE 3: Measured PL decay rates as a function of refractive index n of the cover liquids. The index of the soda-lime glass is $n_0 = 1.50$. Data are shown for both samples *A* (open data points) and *B* (solid data points). The \times -symbols represent data from sample *B* measured one year later. The solid lines are calculations using Eq. (8), the dashed line shows a calculation for sample *A* assuming only radiative decay ($W_{nr} = 0$).

was cleaned again, the $1/e$ -time returned to 9.7 ms. Additional measurements were performed, using other liquids with different refractive indices in the range of 1.3-1.7. Photoluminescence decay rates were determined from the data by inverting the $1/e$ decay times. They are shown in Fig. 3 as open data points, together with the data measured on sample *B* (solid points), which has a deeper Er profile. Also for this sample an increase of the PL decay rate is observed as a function of the refractive index of the cover liquid, but the effect is smaller than for sample *A*. These measurements provide an extremely simple demonstration of modification of the PL decay rate by varying the optical surrounding. The effect is strongest for high refractive index contrasts, and Er profiles close to the surface.

4. Theoretical results

In the dipole approximation the coupling between an atom and the electromagnetic radiation field is given by

$$\mathcal{H}_{int} = -\hat{\boldsymbol{\mu}}(\mathbf{R}) \cdot \hat{\mathbf{E}}(\mathbf{R}), \quad (1)$$

where $\hat{\boldsymbol{\mu}}(\mathbf{R})$ is the dipole moment operator of the atom positioned at \mathbf{R} and $\hat{\mathbf{E}}(\mathbf{R})$ is the electric field operator. The spontaneous emission rate is given by Fermi's

Golden Rule

$$W(\mathbf{R}) = \frac{2\pi}{\hbar^2} |\langle f | \mathcal{H}_{int} | i \rangle|^2 \delta(\omega_i - \omega_f), \quad (2)$$

in which $|i\rangle$ and $|f\rangle$ are the initial and final states with energies $\hbar\omega_{i,f}$. First we look at the i -th cartesian component of the electric field.

$$W_i(\mathbf{R}) = \frac{2\pi}{\hbar^2} |\langle a | \hat{\mu}_i | b \rangle|^2 \sum_{\{\ell\}} \langle 0 | \hat{E}_i(\mathbf{R})^\dagger | \ell \rangle \langle \ell | \hat{E}_i(\mathbf{R}) | 0 \rangle \delta(\omega - \omega_\ell), \quad (3)$$

where $|a\rangle$ and $|b\rangle$ denote ground state and excited state of the atom separated by energy $\hbar\omega$, and $|0\rangle$ and $|\ell\rangle$ the initial state and final states of the field separated by an energy $\hbar\omega_\ell$. The field operator consists of creation operators and an expansion in normalized eigenvectors of the geometry. We use

$$\hat{E}_i(\mathbf{R}) = \sum_{\lambda} \left[(\hbar\omega_{\lambda}/2\varepsilon(\mathbf{R}))^{1/2} \left(ia_{\lambda}^{\dagger} \varphi_{\lambda,i}(\mathbf{R}) \exp(-i\omega_{\lambda}t) + h.c. \right) \right], \quad (4)$$

in which $\varphi_{\lambda,i}(\mathbf{R})$ is i -th cartesian component of the λ -th normalized eigensolution of the classical Maxwell wave equation. Insertion of Eq. (4) in (3) using the commutation rules for the creation and annihilation operators gives

$$W_i(\mathbf{R}) = \frac{\pi\omega}{\hbar\varepsilon(\mathbf{R})} |\langle b | \hat{\mu}_i | a \rangle|^2 \cdot \rho_i(\omega, \mathbf{R}), \quad (5)$$

with

$$\rho_i(\omega, \mathbf{r}) \equiv 2\omega \sum_{\lambda} \varphi_{\lambda,i}(\mathbf{r}) \delta(\omega^2 - \omega_{\lambda}^2) \varphi_{\lambda,i}(\mathbf{r}), \quad (6)$$

Here, $\rho_i(\omega, \mathbf{r})$ is the i -th contribution to a local classical density of states [12]

$$\rho(\omega, \mathbf{r}) \equiv \sum_i \rho_i(\omega, \mathbf{r}). \quad (7)$$

For an absolute determination of $W(\mathbf{R})$ the field operator in Eq. (1) should be used for the local field. From dielectric theory it is well known that the local field seen by an atom is not the same as the macroscopic field. Since the local field is due to the microscopic environment around the atom it is not influenced by the liquid films that are applied in our experiment. Thus, the only parameter that is varied in our experiment is the macroscopic $\rho(\omega, \mathbf{r})$.

The classical density of states (6) can be calculated numerically to any desired precision. For this calculation the complete set of incoming plane waves with one single frequency is summed, using reflection and refraction as given by the Fresnel coefficients. For our problem only the isotropic combination of directions and polarisations is relevant, because the Er ions are randomly distributed in the glass matrix.

Figure 4 shows the result of this calculation of the classical density of optical modes, as a function of the distance from an interface, where the refractive index

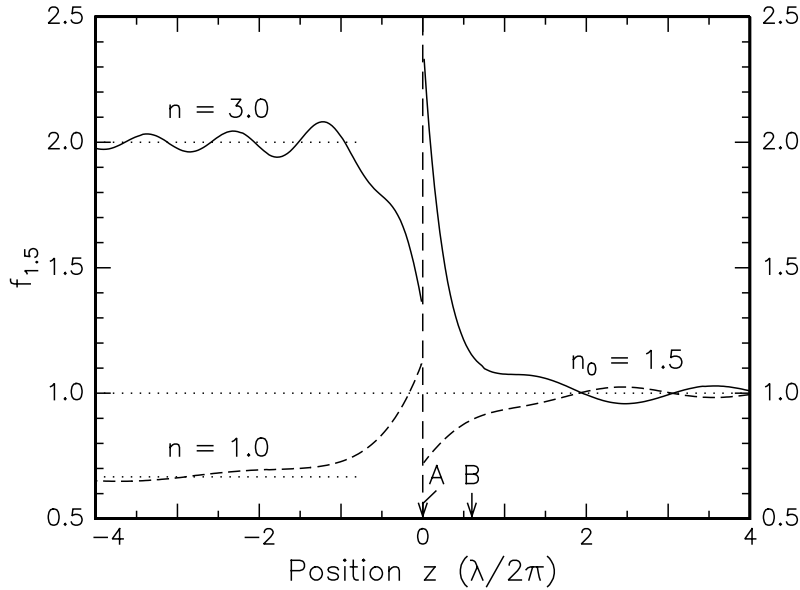


FIGURE 4: Polarisation- and angle-averaged local classical density of optical modes, on both sides of an interface between infinite half-worlds. The refractive index on one side is $n_0 = 1.50$. Calculations are shown for $n = 1.00$ and 3.00 on the other side. The arrows indicate the locations of the Er profiles.

steps from n_0 to n . The density $f_{1.5}$ is normalized to 1 for a bulk material with refractive index $n_0 = 1.5$. Two cases are shown: in one case the index steps from 1.5 to 1.0 at the interface, and in the other case from 1.5 to 3.0. The distance is given in units of $\lambda/2\pi$, where λ is the emission wavelength in vacuum. As can be seen, the DOS is discontinuous at a dielectric interface. This discontinuity is caused by the polarization component parallel to the interface. The oscillations on either side of the interface have a periodicity of $\lambda/2n$ and are due to interference between incoming and reflecting waves. For large distances away from the interface the DOS is proportional to the refractive index. This classical DOS also determines the vacuum field fluctuations: Fig. 4 indeed agrees with the result of a recent calculation of vacuum-field fluctuations [10].

5. Discussion

The factor $f_{1.5}(n, z)$ from Fig. 4 determines the radiative decay rate for Er at distance z from the interface when a liquid with refractive index n covers the glass, relative to the rate in bulk sodalime glass. The distance z can be integrated out by weighted averaging over the Er concentration profile from Fig. 1. In addition to radiative decay, Er may show non-radiative decay, which is not sensitive to changes in the optical DOS. Therefore the total PL decay rate is written as

$$W_{\text{tot}}(n) = W_{\text{nr}} + f_{1.5}(n) \cdot W_{\text{r}}, \quad (8)$$

where W_{nr} is the non-radiative decay rate, and W_{r} the radiative rate in absence of the interface ($n = 1.5$).

The dashed line in Fig. 3 shows the result of a calculation of $W(n)$ using $W_{\text{nr}} = 0$ and $W_{\text{r}} = 110 \text{ s}^{-1}$ for sample *A*. As can be seen, the measured data show a much weaker dependence on n than the calculation. Therefore a non-radiative component has to be introduced: the solid line is obtained using $W_{\text{r}} = 45 \text{ s}^{-1}$ and $W_{\text{nr}} = 65 \text{ s}^{-1}$. As can be seen, this describes the data quite well. The PL efficiency for this sample is $W_{\text{r}}/(W_{\text{r}} + W_{\text{nr}}) = 0.41$. A similar calculation for the data for sample *B*, with the deeper Er profile, is also shown in Fig. 3. The radiative rate is again found to be 45 s^{-1} , indicating that the calculated z -dependence of the DOS agrees with the experimentally observed depth dependence. The non-radiative decay rate in this case is 45 s^{-1} , slightly lower than for sample *A*. This is explained by the fact that the Er concentration in sample *A* is higher than in sample *B*, resulting in concentration quenching which increases W_{nr} [13,14]. In addition there may be quenching centra related to the surface.

These data provide the first experimental determination of the radiative lifetime and quantum efficiency of the ${}^4I_{13/2} \rightarrow {}^4I_{15/2}$ optical transition of Er^{3+} in a silica glass at $1.54 \mu\text{m}$, which is important in modern opto-electronic devices. Other attempts to determine these parameters have failed. For instance, because the multiphonon relaxation rate of the ${}^4I_{13/2}$ manifold is negligible due to the relatively low phonon energies in silica, the efficiency cannot be determined from the temperature dependence of the PL decay [15,16]. Theoretical estimates of the radiative decay rate using Judd-Ofelt theory [8] to determine the matrix elements $\langle a|\hat{\mu}|b\rangle$ in Eq. (5), may yield uncertainties of up to 100 %, in addition to the fact that the local-field correction has to be evaluated. The non-radiative decay found in the present work is attributed to coupling to acceptor states in the host such as hydroxyl impurities. These luminescence quenching effects will be investigated in Chapter 4.

6. Post-implantation annealing

6.1 Experiment and results

As an application, we show how the method explained in this chapter can in fact be used to study the effect of structural defects in the silica network on the Er luminescence transition. The PL decay measurements using cover liquids were repeated on two new samples, which were both implanted while covered with a layer of 120 nm Al stopping layer as is explained for sample *A* in Sect. 2 of this chapter. After etching the Al film, the Er concentration was measured using RBS. The profile peaked at the glass surface at 0.14 at.%. One sample was annealed for one hour at 400°C , and the other at 512°C .

Figure 5 shows PL decay traces measured in the geometry as shown in the inset

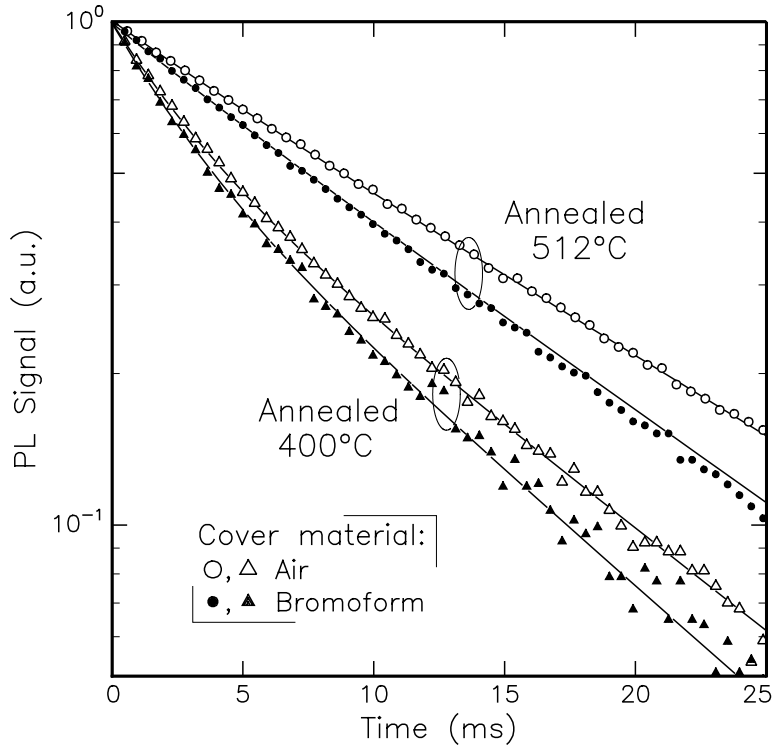


FIGURE 5: Normalized photoluminescence decay traces of the $1.537 \mu\text{m}$ emission from Er-implanted sodalime glass samples on a logarithmic intensity scale. Measurements were performed as is shown in the inset in Fig. 2. Triangles show data for a sample annealed at 400°C , held in air ($n = 1.00$, open data points) and covered with bromoform ($n = 1.54$, filled data points). Circles and dots correspond to a sample annealed at 512°C , also with the glass surface in contact with air (circles) or bromoform (dots).

in Fig. 2. The open data (both circles and triangles) were measured with samples not covered, and the filled data points correspond to the case that the samples were covered with bromoform, a liquid with refractive index 1.54. The triangles in Fig. 5 show data for the sample which was annealed at 400°C , and the circles were measured on the sample which was annealed at 512°C . As can be seen, the PL lifetime after annealing at 512°C is much longer than after annealing at 400°C . In both samples, the PL decays faster with the liquid on the surface than when the surface is in contact with air. This behavior is similar to that observed in Fig. 2 in Sect. 3. In the 512°C annealed sample, the PL decay is almost single exponential, whereas in the 400°C annealed sample (triangles) the decay is clearly not single exponential.

6.2 Analysis and discussion

The data presented in Fig. 5 will be used to demonstrate that thermal annealing only affects non-radiative decay processes of Er^{3+} in silica, while the radiative decay

Anneal	W_r	$W_{nr,1}$	$W_{nr,2}$	α_1/α_2
400°C	49 s ⁻¹	55 s ⁻¹	322 s ⁻¹	4.64
512°C	49 s ⁻¹	34 s ⁻¹	219 s ⁻¹	4.10

TABLE I: Parameters used to calculate the solid lines in Fig. 5 with Eq. (9). W_r , $W_{nr,1}$, $W_{nr,2}$, and α_1/α_2 are ‘free’ parameters for radiative and non-radiative decay rates, and the ratio of prefactors. The radiative decay rate W_r remains the same after annealing, while the ‘spectrum’ of non-radiative decay rates changes.

rate remains unchanged. The data can be described assuming two sets or classes of Er^{3+} in the glass, showing two different non-radiative decay rates:

$$I(n, t) = k \sum_{j=1}^2 \alpha_j \eta_j(n) e^{-(f_{1.5}(n)W_r + W_{nr,j})t}, \quad (9a)$$

where $\eta_j(n)$ is a PL quantum efficiency factor

$$\eta_j(n) = \frac{f_{1.5}(n)W_r}{f_{1.5}(n)W_r + W_{nr,j}}. \quad (9b)$$

In these equations, the prefactor α_j determines the relative contribution of each Er class, η_j is the luminescence quantum efficiency of each Er class, and k is a normalization factor defined such that $I(n, t = 0) \equiv 1$. The factor $f_{1.5}(n)$, defined in Sect. 5, represents the effect of the optical density of states, and amounts to $f_{1.5}(n = 1.00) = 0.79$ for a sample in air and $f_{1.5}(1.54) = 1.02$ for a bromoform covered sample (See Fig. 4). As the exponent in Eq. (9) contains the sum of the rates of radiative and non-radiative decay, these rates cannot be determined separately from one single measurement. However, by simultaneously fitting Eq. (9) through both the air and the bromoform data for one annealing temperature, taking into account the change in $f_{1.5}$, values for W_r and W_{nr} can be determined.

Table I shows the values of the parameters which are used to calculate both the solid lines through the triangles for the sample that was annealed at 400°C, and the values of the set of parameters obtained for the sample that was annealed at 512°C (circles). As can be seen in Fig. 5, the calculated solid lines describe all data quite well. Both the ‘air’ data and the ‘bromoform’ data after annealing at 400°C are fitted using $W_r = 49 \text{ s}^{-1}$ and non-radiative decay rates of 55 and 322 s⁻¹. This shows that the observed change in PL decay when the liquid is put on the surface is indeed explained by the change in the optical density of states ($f_{1.5}$).

Both the ‘air’ data and the ‘bromoform’ data for the 512°C annealed sample are also described using one set of values for radiative and non-radiative decay rates and ratio α_1/α_2 . Note that the value for the radiative decay rate, $W_r = 49 \text{ s}^{-1}$, is the

same as was found after 400°C annealing. The non-radiative decay rates (34 and 219 s⁻¹) are much lower after annealing at 512°C than after annealing at 400°C.

This experiment provides direct proof that the large increase in PL lifetime due to the annealing is fully explained by a decrease in non-radiative decay rate. This is consistent with the data in Chapter 2, where the PL intensity after annealing at 512°C was found to be twice as high as after annealing at 400°C. Indeed, the PL efficiency as defined in Eq. (9b) increases roughly twofold using the values for 512°C and 400°C in Table I. The decrease in non-radiative decay rate on annealing is attributed to the annihilation of implantation induced defects in the silica which quench Er luminescence.

Finally, we will use this density of states method to show an effect of structural relaxation of the silica network at room temperature. The PL decay measurements using cover liquids were repeated in sample *B* (see Sect. 2) one year after the first experiment (Sect. 3). The results are included in Fig. 3 with ×-symbols. As can be seen, the emission rates over the entire index range decreased by 6 s⁻¹. A freshly produced sample still reproduced the original data. The slopes of the calculated curves through the ×-data and the dots are identical indicating that W_r is unchanged, whereas the downward shift of the curve indicates a decrease in W_{nr} . This is explained by annihilation of structural defects that quench the luminescence. Indeed it is known that such structural relaxation processes in glasses can occur over very long time scales.

7. Conclusions

We have demonstrated that the spontaneous emission rate at 1.54 μm of Er³⁺ in glass can be modified simply by applying liquids on the surface. We have shown theoretically that the changes in the spontaneous emission rate can be fully described by changes in the local classical density of states. By comparing the calculated density of states with the measured decay rates, we were able to distinguish radiative and non-radiative decay components in the luminescence of Er³⁺. This was used to show that lifetime changes of Er-implanted silica upon thermal annealing are due to changes in non-radiative decay rates, while the radiative decay rate remains unchanged.

The measurements and calculations presented in this chapter may impact several fields. The notion that, although the PL lifetime of Er in sodalime glass is relatively long (10 ms), the purely radiative lifetime is more than twice as high, has implications for the design of Er-based lasers and optical amplifiers in silica fibers and planar waveguides [9]. The local density of states also affects the cross sections for stimulated emission. Furthermore, in view of the simplicity of the measurement and the analysis reported here, it becomes possible to study spontaneous emission and non-radiative quenching of other luminescent ions in other materials as well.

References

- [1] A. M. Vredenberg, N. E. J. Hunt, E. F. Schubert, D. C. Jacobson, J. M. Poate, and G. J. Zyzik, *Phys. Rev. Lett.* **71**, 517 (1993).
- [2] R. G. Hulet, E. S. Hilfer, and D. Kleppner, *Phys. Rev. Lett.* **55**, 2137 (1985).
- [3] D. J. Heinzen, J. J. Childs, J. E. Thomas, and M. S. Feld, *Phys. Rev. Lett.* **58**, 1320 (1987).
- [4] F. De Martini, G. Innocenti, G. R. Jacobovitz, and P. Mataloni, *Phys. Rev. Lett.* **59**, 2955 (1987).
- [5] K. H. Drexhage, *J. Lumin.* **1,2**, 693 (1970).
- [6] Z. Huang, C. C. Lin, and D. G. Deppe, *IEEE. J. Quantum Electron.* **29**, 2940 (1993).
- [7] E. Yablonovitch, T. J. Gmitter, and R. Bhat, *Phys. Rev. Lett.* **61**, 2546 (1988).
- [8] S. Hübner, *Optical Spectra of Transparent Rare-Earth Compounds* (Academic, New York, 1978).
- [9] E. Desurvire, *Physics Today* **47** (1), 20 (1994).
- [10] H. Khosravi and R. Loudon, *Proc. R. Soc. Lond. A* **433**, 337 (1991).
- [11] See Chapter 2 of this thesis; E. Snoeks, G. N. van den Hoven, and A. Polman, *J. Appl. Phys.* **73**, 8179 (1993).
- [12] B. A. van Tiggelen and E. Kogan, *Phys. Rev. A* **49**, 708 (1994).
- [13] See Chapter 4 of this thesis; E. Snoeks, P. G. Kik, and A. Polman, submitted to *Optical Materials*.
- [14] J. C. Wright, in *Radiationless processes in Molecules and Condensed Phases*, edited by F. K. Fong (Springer, Heidelberg, 1976), Chapter 4.
- [15] W. Ryba-Romanowski, *J. Lumin.* **46**, 163 (1990).
- [16] J. M. Flaherty and B. Di Bartolo, *J. Lumin.* **8**, 51 (1973).

Chapter 4

Concentration quenching

A comparison is made of photoluminescence properties of six sodalime and alkali-borosilicate glasses implanted with Er to concentrations as high as 1.4×10^{21} at./cm³. Clear photoluminescence (PL) spectra around $1.54 \mu\text{m}$, due to the ${}^4I_{13/2} \rightarrow {}^4I_{15/2}$ transition in Er^{3+} are observed, of which the shape depends on the host glass composition. PL lifetimes in the range of $0.9 - 12.6$ ms are found, depending on glass and Er concentration. In borosilicate glass, implantation-induced defects remain after annealing and cause quenching of the Er luminescence due to a direct coupling to the Er. Such defects are not present in Er-implanted sodalime glass after annealing. In both glasses the luminescence lifetime decreases strongly with concentration due to a concentration quenching effect in which energy migration takes place by energy transfer between Er ions, followed by quenching at hydroxyl groups. Concentration quenching via this mechanism is less strong in the borosilicates than in the sodalime glasses, but because of the quenching effect of implantation-induced defects in borosilicates these glasses are not suitable for optical doping by ion implantation.

1. Introduction

Erbium-doped materials have recently become of great interest because of their use as an optical gain medium [1]. Trivalent Er shows an optical transition (intra-4*f*) around $1.54 \mu\text{m}$, a standard wavelength in silica-based optical fiber communication systems. Er-doped fiber amplifiers operating around $1.54 \mu\text{m}$ are now commercially available, and a need has arisen for *planar* amplifiers that can be integrated with planar optical devices such as splitters, switches, and multiplexers [2]. Sodium silicate glasses are suitable substrates for these applications, because fiber compatible waveguides can be fabricated using an ion-exchange process where Na^+ from the glass is replaced by ions that raise the refractive index such as K^+ or Ag^+ [3-5].

To achieve sufficient gain in a few centimeters, as opposed to the meters used for Er-doped fiber amplifiers, the Er concentration needs to be on the order of an atomic percent. Ion implantation can be used to incorporate such high concentrations with

well-controlled doping profiles in the center of an optical waveguide, where the pump intensity is high. In this way, population inversion between the first excited and the ground state can be achieved if the luminescence lifetime is sufficiently long. However, high concentrations can give rise to undesirable effects like concentration quenching and cooperative upconversion [6-8], which reduce the lifetime.

This chapter will focus on concentration quenching, resulting from interaction between excited and unexcited Er ions. Due to this interaction, energy can migrate through the glass until a quenching center is met and the excitation is lost. The efficiency of this process depends on the mean Er-Er distance, the energy exchange rate, and the density of quenching sites. A comparison is made of photoluminescence properties of six different Er-implanted sodalime silicates and alkali-borosilicate glasses, with the aim to find the glass with the lowest luminescence quenching. This glass may then be used to design a planar optical amplifier operating at $1.54\ \mu\text{m}$.

The experiments show two types of Er-fluence dependent luminescence quenching: a) concentration quenching due to energy migration at high Er concentration followed by de-excitation at a quenching site (hydroxyl groups), b) an additional effect only observed in alkali-borosilicate glass, namely quenching by direct coupling of Er ions to implantation-induced defects in the glass.

2. Experimental

In this study, six commercially available silicate glasses were investigated: three different sodalime glasses (Fisher Premium, Pilkington, and a Ca-rich sodalime glass), and three different sodium containing borosilicates (IOT-BGG 31, Corning 0211, and Pyrex). The glass compositions, which are tabulated in Table I, are taken from the literature [4,5,9], except for the Ca-rich sodalime and Pilkington sodalime silicates. For the latter two, compositions were determined using Rutherford backscattering spectrometry (RBS) [10], because the specifications were not available. As can be seen in Table I, all glasses contain Na at different concentrations as the most important network modifying cation, and B is found in BGG 31, Pyrex, and Corning 0211. Note that B_2O_3 is a network former, like SiO_2 . The concentration of hydroxyl groups ($-\text{OH}$) in all six glasses was estimated using infrared (IR) transmission and reflection measurements between 2000 and $4000\ \text{cm}^{-1}$ ($2.5 - 5.0\ \mu\text{m}$), using a Perkin-Elmer 811 IR spectrometer.

All six glasses were implanted with 400 or 500 keV Er ions at room temperature. The ion current density on sample was $\sim 0.5\ \mu\text{A}/\text{cm}^2$, and the implanted fluences ranged from 8.6×10^{14} to $1.8 \times 10^{16}\ /\text{cm}^2$, corresponding to Er peak concentrations up to 2.0 at.%. RBS measurements show that the Er concentration depth-profiles are Gaussian shaped, with a mean depth of $\sim 100\ \text{nm}$, and a full width at half maximum of $\sim 100\ \text{nm}$. To avoid electrical charging of the glasses during ion irradiation, a $420\ \text{\AA}$

	FP ^a	Pilk ^b	Ca-rich ^c	BGG 31 ^d	Pyrex ^e	CRN 0211 ^f
Si	25.6	25.0	24.6	17.6	25.4	22.4
Na	9.8	11.5	6.5	6.8	2.5	4.7
Ca	2.4	3.0	7.0	-	-	-
K	0.6	-	-	<0.01	0.2	3.1
Al	0.5	-	-	7.1	0.9	0.8
B	-	?	?	6.0	7.0	5.3
Mg	0.6	-	-	-	-	-
Ti	-	-	<0.4	-	-	0.8
Zn	-	-	1.0	-	-	1.8
As	-	-	-	0.06	-	-
F	-	-	-	4.2	-	-
O	60.4	60.3	60.1	58.3	64.0	61.2

^a Fisher Premium sodalime silicate, Ref. 4

^b Pilkington sodalime silicate, from RBS data

^c Ca-rich sodalime silicate, from RBS data

^d Integrierte Optik-Technologie alkali-borosilicate, Ref. 5

^e Pyrex 7740 alkali-borosilicate (Corning), Ref. 9

^f Corning 0211 alkali-borosilicate, Ref. 4

TABLE I: Compositions of the used silicates in at.%. The question marks indicate that B cannot be detected with RBS.

thick Al film was evaporated onto the glass surface. It was etched off in a NaOH solution after implantation. Thermal annealing was performed in a tube-furnace at a base pressure below 5×10^{-7} mbar, at temperatures up to 600°C. All anneals were done for one hour.

Photoluminescence (PL) spectroscopy was carried out at room temperature, with the 514.5 or the 488.0 nm line of an Ar-ion laser as excitation source. Powers of 350 mW were used in a ~ 0.3 mm diameter spot, for which no beam heating of the samples was observed. The luminescence signal was spectrally analysed with a 48-cm monochromator, and detected with a liquid-nitrogen-cooled Ge detector, yielding a spectral resolution of 2.3 nm. The pump beam was chopped at 12 Hz and spectra were recorded using a lock-in amplifier. Time-resolved luminescence decay measurements were performed using a 1.5 ms, 1.4 W pump pulse with a cutoff time shorter than 150 μ s, and averaged using a digital oscilloscope.

3. Results and discussion

3.1 Photoluminescence

First, we will compare the photoluminescence of six different silicate glasses implanted with Er to a fixed peak concentration of 0.2 at.%. All samples were an-

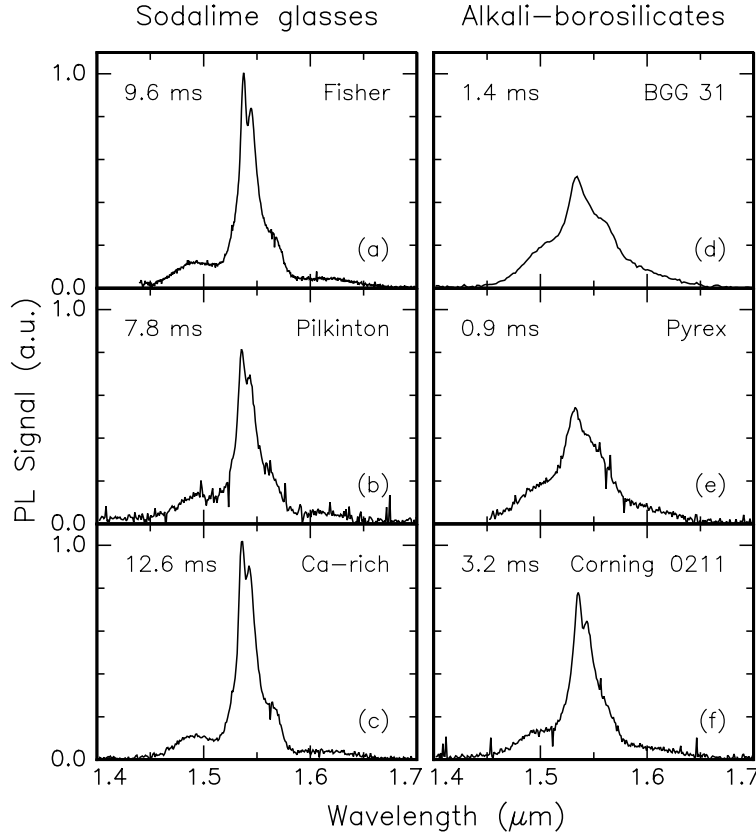


FIGURE 1: Room temperature PL spectra of different Er-implanted sodium containing silicate glasses: Fisher Premium (a), Pilkinton (b), and Ca-rich (c) are sodalime glasses; BGG 31 (d), Pyrex (e), and Corning 0211 (f) are alkali-borosilicates. The Er concentration was 0.2 at.% in each case, and the PL lifetimes at $1.535 \mu\text{m}$ are indicated in the figures. All samples were annealed at $500 - 600^\circ\text{C}$.

nealed to obtain maximum PL intensity and lifetime. The annealing temperature dependence of the PL intensity in each examined glass was qualitatively the same as shown in Chapter 2 for Fisher Premium sodalime. The maximum PL intensity was reached after annealing above 500°C , except for BGG 31 where 400°C was sufficient, and Pyrex where 600°C was required.

Figure 1 shows the PL spectra of the Er-implanted samples, normalized to integrated signal. All samples show broad PL spectra around $1.54 \mu\text{m}$, characteristic for the ${}^4I_{13/2} \rightarrow {}^4I_{15/2}$ intra- $4f$ transition of Er^{3+} [11]. The spectra in BGG 31 and Pyrex are clearly broader than the spectra in the other hosts. This is ascribed to the relatively low concentration of network modifiers (Na, Ca, K, Mg) in these glasses in addition to the presence of B (a network former). This leads to a more inhomogeneous distribution of Er sites, leading to more inhomogeneous broadening of the spectra.

The PL lifetimes (τ) measured at $1.535 \mu\text{m}$ after annealing are indicated in the

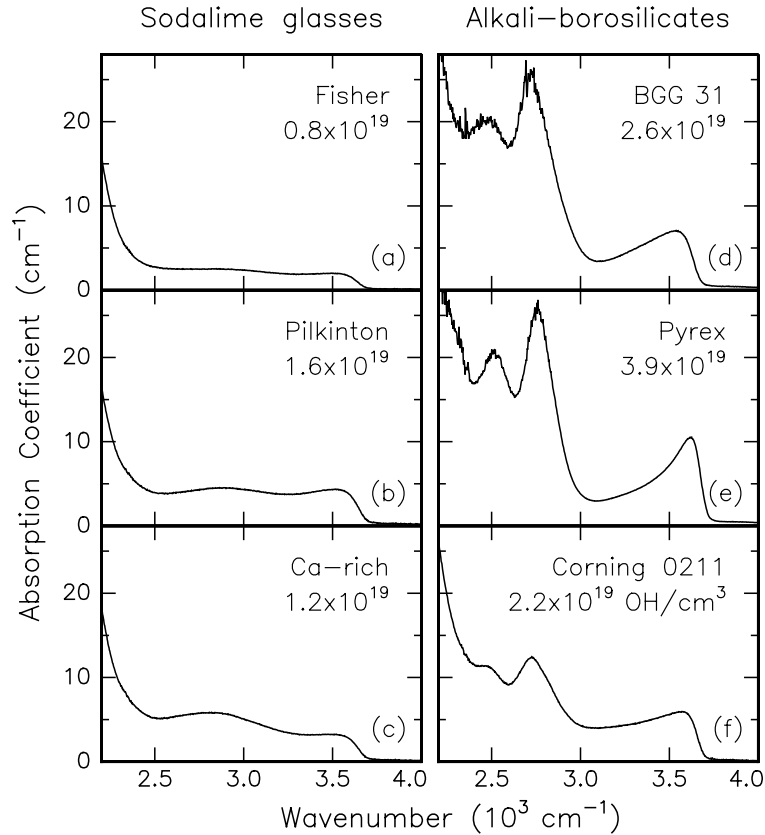


FIGURE 2: Infrared absorption spectra in each of the unimplanted glasses: Fisher Premium (a), Pilkinton (b), and Ca-rich sodalime (c); BGG 31 (d), Pyrex (e), and Corning 0211 (f). The OH densities given in the figure for each glass in units of $\text{—OH}/\text{cm}^3$ are calculated using an absorption cross section of $1.2 \times 10^{-19} \text{ cm}^2$.

top left-hand corners of Figs. 1a-f. As can be seen, the PL lifetime depends strongly on host material: 12.6 ms is measured in the Ca-rich sodalime glass, and only 0.9 ms in Pyrex. The measured PL decay rate is the sum of radiative and non-radiative decay rates. In Chapter 3 we showed that the radiative decay rate of Er implanted in sodalime glass is $W_r = 45 \text{ s}^{-1}$ (corresponding to 22 ms), independent of Er concentration and annealing treatment [12,13]. Because of the shielding of the $4f$ electrons by the outer lying $5s^25p^6$ shells [11], it can be assumed that the radiative decay rate in similar multicomponent silica-based materials is approximately the same. Therefore, the observed strong variation of PL lifetime with host is ascribed to relatively large differences in non-radiative decay rate, as will be discussed hereafter.

3.2 Hydroxyl impurities

Figure 2 shows IR-absorption spectra in the range from 2200 to 4000 cm^{-1} for all the six unimplanted glasses. The strong absorption below 2400 cm^{-1} is due to excitation

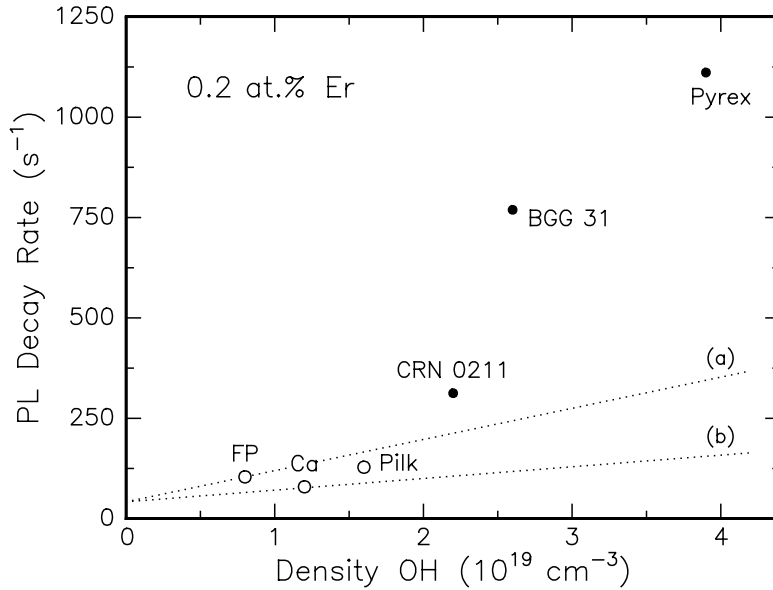


FIGURE 3: Correlation between the PL decay rate of the six different Er-implanted (400 or 500 keV, 1.4×10^{20} Er/cm³) silicate glasses (after annealing), and the density of free —OH in these glasses. Circles are used for sodalime glasses, and large dots for alkali-borosilicates. The dotted lines are calculated with Eq. (1), using $W_r = 42$ s⁻¹, $N_{\text{Er}} = 1.4 \times 10^{20}$ at./cm³, and either $C_{\text{Er,Er}} = 2.3 \times 10^{-51}$ m⁶/s (a) or 0.86×10^{-51} m⁶/s (b).

of Si-O vibrations [9,14]. For the borosilicates (Figs. 2d-f) three clear absorption bands at 2500, 2700, and 3600 cm⁻¹ are visible. The bands at 2700 and 3600 cm⁻¹ are also seen in the three sodalime glasses (Figs. 2a-c), but much weaker. All bands are ascribed to absorption by hydroxyl groups, and in particular the 3600 cm⁻¹ (2.8 μm) band is due to the stretch vibration of free —OH [9,14,15]. Using an absorption cross section of 1.2×10^{-19} cm² for this band [16], an estimate of the density of free —OH (N_{OH}) can be made from the measured absorption coefficient at 3600 cm⁻¹. The results of these estimates are indicated in Fig. 2 for each glass in units of —OH/cm³. The —OH concentrations range from 0.8×10^{19} OH/cm³ in Fisher Premium sodalime glass to 3.9×10^{19} OH/cm³ in Pyrex.

It is known that free —OH is one of the important quenching centers in Er-doped glasses [17-19]. The energy of the ${}^4I_{13/2} \rightarrow {}^4I_{15/2}$ transition in Er³⁺ (~ 6500 cm⁻¹) corresponds to the energy of the second harmonic of the —OH stretching vibration. Therefore, if an Er³⁺ ion is coupled to —OH, non-radiative relaxation of the ${}^4I_{13/2}$ Er³⁺ level can occur by excitation of two —OH vibrational quanta.

Figure 3 shows the Er PL decay rate (i.e. $1/\tau$) plotted against the density of free —OH in the six glasses, using the data depicted in Figs. 1 and 2. Although the data show a trend relating the measured Er PL lifetimes in the various glasses to the estimated density of free —OH, no clear correlation is found. This will be dis-

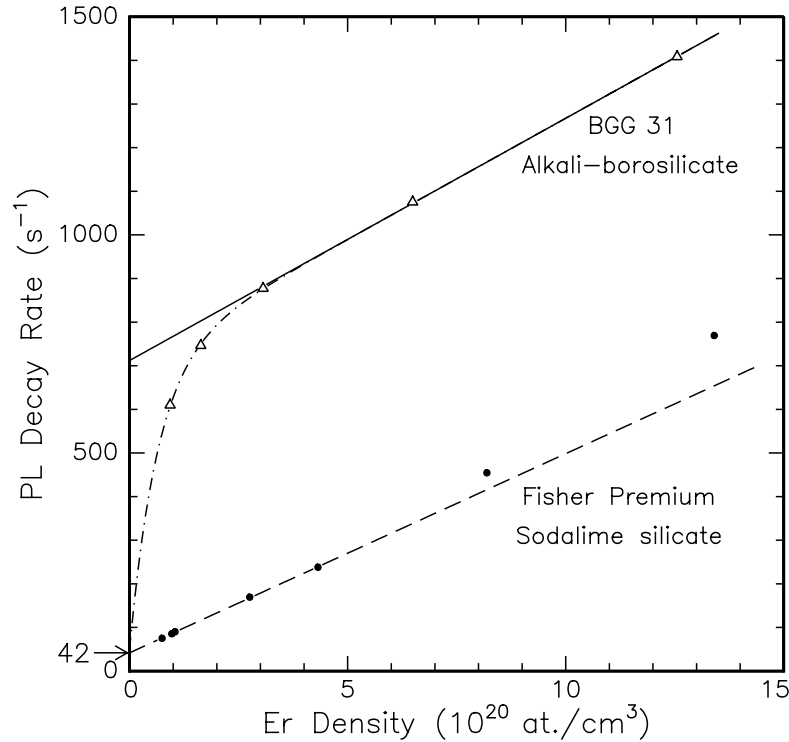


FIGURE 4: Erbium photoluminescence decay rate versus Er peak density (after annealing). The dots show data for Er in Fisher Premium sodalime glass. The dashed line is a linear fit through the data below 5×10^{20} Er/cm 3 , and intercepts the y -axis at $42 s^{-1}$. The triangles show data for Er implanted BGG 31 alkali-borosilicate glass after annealing. The solid line is a linear fit through the data above 2×10^{20} Er/cm 3 , and the $- \cdot -$ line is a fit based on a model which includes the effect of irradiation damage.

cussed in detail further on, using additional data on the Er-concentration dependence of the PL lifetimes.

3.3 Concentration quenching and defects

In two glasses – Fisher Premium as an example of a sodalime glass, and BGG 31 to represent the alkali-borosilicates – the Er implant fluence was varied from 8×10^{13} to 1.8×10^{16} Er/cm 2 (peak concentration of 2.0 at.%). Photoluminescence decay rates were measured at room temperature after annealing.

3.3.1 Sodalime glass

The dots in Fig. 4 show the PL decay rate (i.e. $1/\tau$) of Er in Fisher Premium sodalime glass as a function of Er concentration (the atomic density at the peak of the Gaussian implantation profile), after annealing at 512°C . The data show that the PL decay rate increases almost linearly with Er density.

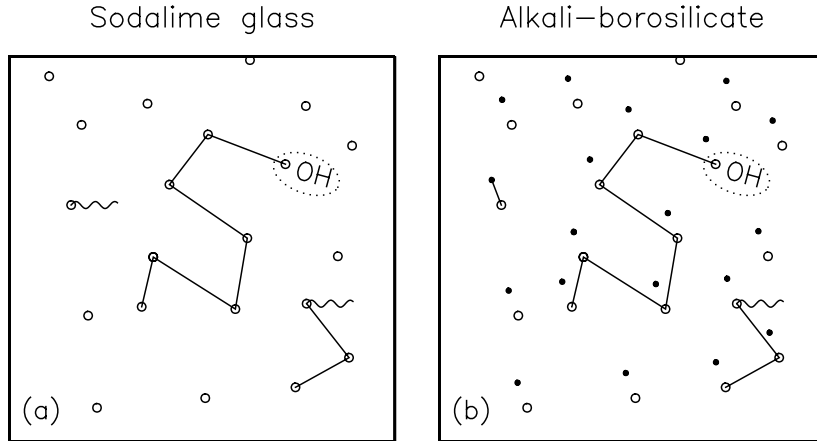


FIGURE 5: Schematic representations of the possible luminescence decay mechanisms in Er-implanted silica glass. (a) After excitation, each Er ion (circle) has a probability to emit a photon (wavy arrow), or to transfer the excitation to a neighboring Er ion (straight line). Rapid quenching takes place at a small fraction of Er ions that are closely bound to an —OH group. In (b), a third decay mechanism is added; the probability for each Er ion to directly loose the excitation to an implantation-induced defect (black dot). As is discussed in the text, (a) corresponds to Er-implanted sodalime glass, while (b) refers to effects in Er-implanted borosilicate glass.

This concentration quenching effect and the role of defects and impurities can be understood from Fig. 5, which shows a schematic picture of the three ways how an excited Er ion can de-excite: 1) by emission of a photon (wavy arrow), 2) by non-radiative relaxation through coupling to a quenching site (for instance —OH), or 3) by energy transfer to a neighboring Er ion (straight lines) [20]. In the latter way the excitation can migrate through the glass, and when an Er ion is met which is coupled to an —OH group the excitation is lost.

For a homogeneous distribution of Er ions, and a low density of quenching sites, and assuming that the energy exchange between Er ions takes place via dipole-dipole interaction, the total concentration-dependent decay rate is given by [8,21-23]

$$W = W_r + W_i + 8\pi C_{\text{Er,Er}} N_q N_{\text{Er}}. \quad (1)$$

Here W_r is the radiative decay rate, W_i is the internal non-radiative quench rate, $C_{\text{Er,Er}}$ is an Er-Er interaction constant [8], and N_q and N_{Er} are the density of quenching sites and Er ions, respectively. Note that $W_r + W_i$ is the decay rate in absence of migration. It is assumed in Eq. (1) that the absorption spectrum of a quenching site is identical to the absorption spectrum of an Er^{3+} ion in sodalime glass. This simplification may be made in the case that the quenching mechanism is via excitation of vibrations in —OH closely bound to a limited number of Er ions.

Equation (1) is used to fit the data for Er in sodalime glass in Fig. 4. Below 5×10^{20} at./ cm^3 excellent agreement is achieved: the dashed line is the result of a

linear fit with a slope of $(4.6 \pm 0.4) \times 10^{-25} \text{ m}^3/\text{s}$. The extrapolated PL decay rate for zero Er density is $41.9 \pm 1.1 \text{ s}^{-1}$. This value is very close to the experimental value of the radiative decay rate $W_r = 45 \text{ s}^{-1}$, found in Chapter 3. This implies that the internal non-radiative decay rate $W_i \approx 0$,^a which means that in absence of quenching due to migration all Er ions (except those coupled to —OH) decay in a purely radiative fashion. The data in Fig. 4 can be described assuming a constant density of quenching centers N_q , which implies that this density is independent of Er fluence, and therefore these quenchers are *not* related to the damage created by the ion beam.

To supply support for the latter conclusion, samples were prepared in which irradiation damage was provided independently from the Er concentration in the following way. A sample was first implanted with a low fluence of Er at 500 keV ($1.4 \times 10^{15} \text{ Er/cm}^2$, corresponding to $1.0 \times 10^{20} \text{ Er/cm}^3$), and subsequently irradiated with 1.8 MeV Au to fluences in the $1 \times 10^{14} - 1 \times 10^{16} \text{ Au/cm}^2$ range. The projected range of the Au ions is well beyond the Er profile, so that ion irradiation damage is provided all through the Er-doped region,^b without changing the chemical environment of the Er. All samples were annealed at 512°C after the irradiations were completed. The crosses (\times) in Fig. 6 show the Er PL decay rates of the Au co-irradiated samples as a function of total irradiation fluence (Er+Au). As can be seen, the PL decay rate remains almost constant with Au fluence. For comparison, Fig. 6 also includes the Er PL decay rate as a function of fluence in the case that only 500 keV Er is implanted (filled data points, same data as in Fig. 4). As the additional Au fluence, which produces a similar amount of irradiation damage per ion as the Er,^b does not cause a large increase in the Er PL decay rate, it is confirmed that the strong increase of PL decay rate with increasing Er fluence is *not* explained by accumulation of beam-induced damage, but by an Er concentration quenching effect, i.e. migration followed by quenching at a fixed density of quenching sites.

If it is assumed that all free —OH contributes to quenching, then $N_q = N_{\text{OH}} = 8 \times 10^{18} / \text{cm}^3$ (as estimated in Sect. 3.2) can be inserted in Eq. (1). From the slope of the fit, $C_{\text{Er,Er}} = 2.3 \times 10^{-51} \text{ m}^3/\text{s}$ is then extracted. This implies that for an Er concentration of approximately $\sim 3 \times 10^{18} \text{ Er/cm}^3$ the Er-Er energy transfer rate equals the radiative decay rate. The value for $C_{\text{Er,Er}}$ will be compared with other data in Sect. 4.

A final detail observed in Fig. 4 is that for Er densities above $5 \times 10^{20} \text{ at./cm}^3$ the measured PL decay rates in sodalime glass deviate from the linear behavior predicted by Eq. (1). This effect may be related to the fact that at high fluence ion

^a Using $W_r = 45 \text{ s}^{-1}$, W_i would be -3 s^{-1} , which is unphysical, and possibly related to the fact that the linear behavior in Eq. (1) is only valid when the density of quenching sites is low compared to the density of Er, which is not the case in the limit $N_{\text{Er}} \rightarrow 0$.

^b The nuclear energy loss per ion of both Er and Au averaged in the Er-doped region is $300 \text{ eV}/\text{\AA}$, and the electronic energy loss 30 and $140 \text{ eV}/\text{\AA}$, respectively. (Monte Carlo simulation TRIM89, Ref. 24.)

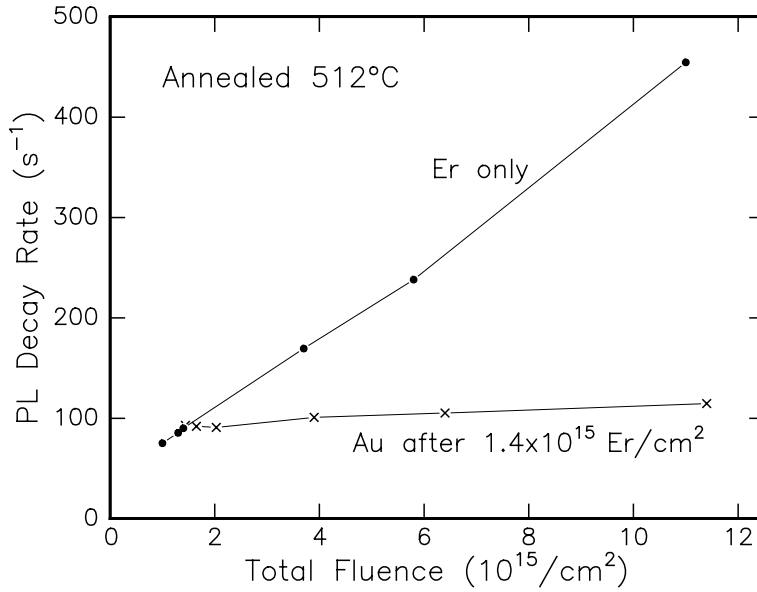


FIGURE 6: Erbium PL decay rates in sodalime glass as a function of total implanted fluence, after annealing. The solid data points shows the Er PL decay rate when only 500 keV Er is implanted. The crosses (\times) show the Er decay rate in a sample first implanted with $1.4 \times 10^{15} \text{ Er/cm}^2$ and subsequently with 1.8 MeV Au to fluences ranging from 1×10^{14} to $1 \times 10^{16} \text{ Au/cm}^2$. All samples were annealed at 512°C after all irradiations were completed.

irradiation the high density of displaced atoms can cause local non-uniformities in the Er concentration. This then would enhance concentration quenching. Microscopic redistribution of impurities in ion irradiated SiO_2 has been observed before; for instance, Ag [25] or Au [26] coalesce into metallic nano-clusters, and metals such as Fe can form oxide clusters in silica [27] when sufficient mobility is provided by an ion beam. Ion-beam induced atomic mobility effects will be discussed in Chapters 7 and 8.

3.3.2 Alkali-borosilicate glass

The triangles in Fig. 4 show the measured PL decay rate of Er implanted BGG 31 alkali-borosilicate glass as a function of Er density after annealing at 400°C . The used Er fluences range from 0.09 to $1.2 \times 10^{16} \text{ ions/cm}^2$. For all concentrations, the decay rate is higher than what is found for Er implanted sodalime glass. As can be seen, above $3 \times 10^{20} \text{ Er/cm}^3$, the PL decay rate depends linearly on the Er density. Below $3 \times 10^{20} \text{ Er/cm}^3$ the decay rate is a steeper function of Er density than above $3 \times 10^{20} \text{ Er/cm}^3$. This behavior is clearly different from what is observed in sodalime glass. The high dose data for Er implanted BGG 31 can be described using Eq. (1). A slope of $(5.6 \pm 0.5) \times 10^{-25} \text{ m}^3/\text{s}$ and $W_r + W_i = 718 \pm 2 \text{ s}^{-1}$ are found (solid line).

However, this model which assumes a constant number of sinks (N_q) and a constant W_i , does not explain the low fluence data.

We suggest that for the case of BGG 31, ion implantation induced defects, of which the density is Er-fluence dependent, play a role in the quenching of the Er luminescence. Therefore a modification in the concentration quenching model has to be made to account for beam induced effects. $C_{\text{Er,Er}}$ and W_r are independent of Er fluence. The parameters N_q and W_i in Eq. (1), however, may possibly increase (decrease is very unlikely) with Er fluence. Let us first consider that N_q – which is the density of quenching centers that couples only to a small fraction of the Er ions – would increase during ion irradiation due to the formation of beam-induced defects. According to Eq. (1), the slope in Fig. 4 would then *increase* with Er density (fluence). The low-fluence data, however, show a *decrease* of the slope, and therefore cannot be explained by an increase in N_q . The other possibility is that W_i increases with Er fluence, i. e. an increase in the internal quench rate of each Er ion with increasing fluence ϕ . This means that Er ions directly couple to irradiation induced defects, and all Er ions have a certain probability to loose the excitation to such a defect. This is schematically indicated in Fig. 5b, where the black dots represent beam-induced defects. Using a ion damage creation model – in which the density of irradiation induced defects follows an exponentially saturating law proportional to $[1 - \exp(-\phi/\phi_c)]$ [28], with ϕ_c a characteristic fluence – W_i can be written as a function of Er fluence:

$$W_i(\phi) = [W_{\text{sat}} - W_r - W_i(0)] [1 - \exp(-\phi/\phi_c)] + W_i(0). \quad (2)$$

Here W_{sat} is the Er PL decay rate in absence of energy migration when irradiation damage has saturated, and $W_i(0)$ the internal quench rate before irradiation damage is done.

The $- \cdot -$ line in Fig. 4 shows the result of a fit using Eqs. (1) and (2). This fit describes the data very well. The fit parameters are: $\phi_c = (6.8 \pm 0.4) \times 10^{14}$ Er/cm², $8\pi C_{\text{Er,Er}} N_q = (5.6 \pm 0.5) \times 10^{-25}$ m³/s, and $W_{\text{sat}} = 715 \pm 3$ s⁻¹. The intercept with the y -axis ($W_r + W_i(0)$) could not be determined accurately due to the fact that no PL lifetime data were available for very low Er fluences. These data imply that in the absence of excitation migration, Er ions decay both radiatively, and non-radiatively due to coupling to irradiation-induced defects. Using the concentration of free —OH in BGG 31, $N_q = 2.6 \times 10^{19}$ /cm³ (see Sect. 3.2), we find $C_{\text{Er,Er}} = 8.6 \times 10^{-52}$ m⁶/s from the fit results. This value for $C_{\text{Er,Er}}$ is lower than in the case of Er in Fisher Premium sodalime glass, which will be discussed in Sect. 4.

The effect of ion irradiation damage on the Er luminescence lifetime which is observed in BGG 31 alkali-borosilicate glass, and not in sodalime glass, is attributed to the presence of boron in the network. Electron-spin-resonance (ESR) studies have shown that B enhances the irradiation sensitivity for electronic damage in silica by orders of magnitude, due to formation of B-related point defects [29]. The suggestion

that B enhances Er PL quenching is supported by Fig. 3, where it can be seen that all three Er-implanted alkali borosilicates (dots) show significantly higher PL decay rates than the sodalime glasses (circles). To illustrate this, the dotted line (a) is drawn in Fig. 3 which shows the PL decay rate as a function of OH density according to Eq. (1) with $C_{\text{Er,Er}} = 2.3 \times 10^{-51} \text{ m}^6/\text{s}$ found for Er in Fisher Premium sodalime glass. A similar line, but then using the value $C_{\text{Er,Er}} = 0.86 \times 10^{-51} \text{ m}^6/\text{s}$ as found for Er in BGG 31 alkali-borosilicate is also shown [dotted line (b)]. As can be seen, neither of these lines describe the high decay rates found experimentally for the borosilicate glasses, indicating that additional irradiation induced damage plays a role in these borosilicates.

4. Comparison to other work

In the previous section it was found that the excitation transfer constant ($C_{\text{Er,Er}}$) in Fisher sodalime glass is $2.3 \times 10^{-51} \text{ m}^6/\text{s}$, and in BGG 31 alkali-borosilicate glass $0.86 \times 10^{-51} \text{ m}^6/\text{s}$. The difference can be explained to some extent by the fact that due to inhomogeneous broadening, the Er PL spectrum in alkali-borosilicate glass is broader than in sodalime glass (Fig. 1). Therefore, the mean overlap integral of the emission and absorption spectrum between nearest neighbors is smaller in BGG 31 than in sodalime, or put differently, the effective distance between well matching Er ions becomes larger. Also, differences in the phonon spectra of the glasses may cause differences in transfer rate. The values of $C_{\text{Er,Er}}$ found here are in the same range as values found by Gapontsev *et al* ($0.7 \times 10^{-51} \text{ m}^6/\text{s}$) by varying the —OH concentration in phosphate glass samples with fixed Er density [17,30].

The results presented in this chapter concern the energy transfer between excited and non-excited Er ions, which leads to lowering of the PL decay time when a small fraction of Er ions is excited. However, in an actual Er-doped optical amplifier, where a high fraction of excited Er ions is needed, a second quenching mechanism becomes important: *cooperative upconversion*. In this process, energy is transferred between two *excited* Er ions, leaving one of both ions de-excited [6-8]. It is shown in Chapter 5 that the de-excitation rate of Er in sodalime glass at a concentration of 0.2 at.% ($\approx 1.4 \times 10^{20} \text{ at./cm}^3$) can increase fourfold due to upconversion. The upconversion coefficient is highest in glasses in which Er shows broad PL spectra, because the upconversion process is resonant only in the long wavelength part of the transition [31]. Therefore, we predict that glasses such as BGG 31 and Pyrex in which Er^{3+} shows broad PL spectra (see Fig. 1), will suffer from relatively strong cooperative upconversion, whereas the sodalime glasses with the narrower spectra will show less upconversion.

The $4f$ levels are relatively fixed, because they are electronically shielded by outer lying $5s^2 5p^6$ shells [11]. Therefore, neither energy migration, nor cooperative upconversion can be completely avoided by choice of host. The final choice

should be made by comparing the effects of migration-quenching and upconversion-quenching. In an Er-based optical amplifier operating at $1.54\ \mu\text{m}$, the rate of de-excitation is found by solving the rate equation for the fraction n of excited Er ions: $dn/dt = -n/\tau - CN_{\text{Er}}n^2$, where C is the upconversion coefficient. In the limit $n \rightarrow 0$, the ‘spontaneous’ de-excitation rate is given by $1/\tau$, and in the limit $n \rightarrow 1$ by the sum $1/\tau + CN_{\text{Er}}$. In sodalime glass, $C = 3 \times 10^{-24}\ \text{m}^3/\text{s}$ [31], and for Er concentrations above $1.5 \times 10^{19}\ \text{at./cm}^3$ ($\sim 0.02\ \text{at.}\%$), $CN_{\text{Er}} > 1/\tau$, i. e. upconversion is the dominant de-excitation mechanism. For planar amplifiers, where concentrations are usually higher than $1.5 \times 10^{19}\ \text{Er/cm}^3$, the most suitable host is therefore the host which shows least upconversion, i. e. narrowest PL spectrum. From the point of view of Er luminescence properties, the three sodalime glasses which were examined in this chapter are equally well suited. When upconversion is not the dominant decay mechanism, for instance in fiber amplifiers, broad PL spectra (as for instance in borosilicates) are more preferred. However, for the borosilicates, ion implantation is not a suitable technique for optical doping due to the effect of implantation-induced damage on the Er luminescence lifetime.

5. Conclusions

Six different silicate glasses (three sodalime glasses and three alkali-borosilicates) were implanted with Er and annealed. For each glass, the PL spectrum around $1.54\ \mu\text{m}$, the PL lifetime, and the concentration of free $-\text{OH}$ were measured. The PL lifetime depends strongly on host glass. This is attributed to differences in non-radiative decay rates; $-\text{OH}$ is one of the quenching sites. For two glasses the Er concentration (implant fluence) was varied in the range of 7×10^{19} - $1.5 \times 10^{21}\ \text{at./cm}^3$. In both cases the PL decay rate increases with Er density.

[a] Sodalime glass. The increase in PL decay rate with Er density is described using a simple concentration quenching model with energy migration due to Er-Er interactions as rate-limiting process. The Er-Er energy transfer coefficient $C_{\text{Er,Er}} = 2.3 \times 10^{-51}\ \text{m}^6/\text{s}$. After annealing, implantation-induced defects cause no quenching in sodalime glass. The extrapolated radiative decay rate is $42\ \text{s}^{-1}$ (corresponding to $\tau = 24\ \text{ms}$).

[b] Alkali-borosilicate glass. The increase in PL decay rate with Er density is due to both implantation-induced defects – of which the density depends on fluence – and Er-concentration dependent energy migration. The energy transfer coefficient is $C_{\text{Er,Er}} = 0.86 \times 10^{-51}\ \text{m}^6/\text{s}$. Implantation-induced damage causes significant internal non-radiative quenching for each Er ion. This damage production is attributed to the presence of boron in the glass, which increases the sensitivity for ionization damage.

Resonant Er-to-Er energy transfer in borosilicate glass is less efficient than in sodalime glass, which is partly due to the higher inhomogeneous broadening of the

4f manifolds in borosilicate glass. Therefore, the effect of concentration quenching is lower in borosilicates than in sodalime glass. However, ion implantation is not a suitable technique to dope borosilicates with optically active ions, due to the effect of irradiation damage leading to low luminescence lifetimes. In the design of planar amplifiers, not only concentration quenching due to energy migration, but also cooperative upconversion should be taken into account. In many cases the latter will be the dominant decay process.

References

- [1] E. Desurvire, *Physics Today* **47** (1), 20 (1994).
- [2] C. H. Henry, G. E. Blonder, and R. F. Kazarinov, *J. Lightwave Technol.* **7**, 1530 (1989).
- [3] J. Viljanen and M. Leppihalme, *Proc. First Europ. Conf. on Integrated Optics* (London, Great Britain, 1981), 18.
- [4] S. I. Najafi, *Appl. Opt.* **27**, 3728 (1988).
- [5] L. Roß, *Glastech. Ber.* **62**, 285 (1989).
- [6] W. J. Miniscalco, *J. Lightwave Technol.* **9**, 234 (1991).
- [7] J. C. Wright, in *Radiationless processes in Molecules and Condensed Phases*, edited by F. K. Fong (Springer, Heidelberg, 1976), Chapter 4.
- [8] F. Auzel, in *Radiationless Processes*, B. DiBartolo, Ed. (Plenum Press, New York, 1980).
- [9] H. Scholze, *Glass* (Springer, Heidelberg, 1990).
- [10] Wei-Kan Chu, J. W. Mayer, and M.-A. Nicolet, *Backscattering Spectrometry* (Academic, New York, 1978).
- [11] S. Hüfner, *Optical Spectra of Transparent Rare-Earth Compounds* (Academic, New York, 1978).
- [12] Chapter 2 of this thesis; E. Snoeks, G. N. van den Hoven, and A. Polman, *J. Appl. Phys.* **73**, 8179 (1993).
- [13] Chapter 3 of this thesis; E. Snoeks, A. Lagendijk, and A. Polman, *Phys. Rev. Lett.* **74** (1995), in press.
- [14] R. Brückner and H. Hessenkemper, *Glastech. Ber.* **66**, 245 (1993).
- [15] H. Scholze, *Glastech. Ber.* **32**, 142 (1959).
- [16] H. Scholze, *Glastech. Ber.* **32**, 81 (1959).
- [17] V. P. Gapontsev, A. A. Izyneev, Yu. E. Sverchov, and M. R. Syrtlanov, *Sov. J. Quantum Electron.* **11**, 1101 (1981).
- [18] Yingchao Yan, A. J. Faber, and H. de Waal, *J. Non-Cryst. Solids* **181**, 283 (1995).
- [19] A. J. Bruce, W. A. Reed, A. E. Neeves, L. R. Copeland, W. H. Grodkiewicz, and A. Lidgard, *Mat. Res. Soc. Symp. Proc.* **244**, 157 (1992).
- [20] Th. Förster, *Discuss. Faraday Soc.* **27**, 7 (1959); Th. Förster, *Ann. Physik* **2**, 55

- (1948).
- [21] P. G. de Gennes, *J. Phys. Chem. Solids* **7**, 345 (1958).
- [22] M. J. Weber, *Phys. Rev. B* **4**, 2932 (1971).
- [23] N. Krasutsky and H. W. Moos, *Phys. Rev. B* **8**, 1010 (1979).
- [24] J. P. Biersack and L. J. Haggmark, *Nucl. Instrum. Methods* **174**, 257 (1980).
- [25] F. Caccavale, G. de Marchi, P. Mazzoldi, C. Meneghini, A. Quaranta, G. W. Arnold, G. Battaglin, and G. Mattei, in *Tech. Dig. Ion Implantation Techn. Conf.*, Catania, Italy, 1994.
- [26] R. H. Magruder III, Li Yang, R. F. Haglund, Jr., C. W. White, Lina Yang, R. Dorsinville, and R. R. Alfano, *Appl. Phys. Lett.* **62**, 1730 (1993).
- [27] A. Perez, M. Treilleux, T. Capra, and D. L. Griscom, *J. Mater. Res.* **2**, 910 (1987).
- [28] F. F. Morehead, Jr. and B. L. Crowder, *Radiat. Eff.* **6**, 27 (1970).
- [29] D. L. Griscom, G. H. Sigel, Jr., and R. J. Ginther, *J. Appl. Phys.* **47**, 960 (1976).
- [30] V. P. Gapontsev, S. M. Matitsin, A. A. Izineev, and V. B. Kravchenko, *Erbium glass lasers and their applications*, in *Optics and Laser Techn.* **14**, Aug. 1992 (Butterworth & Co), 189.
- [31] Chapter 5 of this thesis; E. Snoeks, G. N. van den Hoven, A. Polman, B. Hendriksen, M. B. J. Diemeer, F. Priolo, submitted to *J. Opt. Soc. Am. B*.

Chapter 5

Cooperative upconversion and optical amplification

Sodalime silicate glass has been locally doped with 0.2 at.% erbium by 3.0 and 5.0 MeV ion implantation. Single mode, fiber compatible optical waveguides were then fabricated using $\text{Na}^+ \leftrightarrow \text{K}^+$ ion exchange. Characteristic photoluminescence (PL) around $1.54 \mu\text{m}$ of Er^{3+} is observed, upon excitation at $1.48 \mu\text{m}$. For low pump intensity the PL decay is nearly single exponential with a lifetime of 7.2 ms. At high intensity it becomes non-exponential due to cooperative upconversion, an interaction between excited Er ions. Self consistent modeling of the PL intensity and decay data yields an upconversion coefficient of $(3.2 \pm 0.8) \times 10^{-24} \text{ m}^3/\text{s}$. The effect of upconversion on optical gain is shown and discussed. An extrapolation of measured data shows that 1 dB/cm net gain is possible in the present Er-implanted sodalime glass.

1. Introduction

Erbium-doped materials have become of great interest because of their use as optical gain media [1,2]. Erbium shows an optical transition around $1.54 \mu\text{m}$, a standard wavelength in silica-based optical fiber communication systems. Optical fibers have been doped with Er to fabricate lasers, and in 1987 the first Er-doped fiber amplifiers operating around $1.54 \mu\text{m}$ were reported [3]. More recently, a need has arisen for planar amplifiers that can be integrated with planar optical devices such as optical switches and multiplexers [4]. For example, a planar amplifier with a moderate gain of 3 dB could compensate for the intensity decrease in a Y-splitter. To obtain such gain in a few centimeters long waveguide, as opposed to the meters used for Er-doped fiber amplifiers, the Er concentration needs to be on the order of an atomic percent. However, high Er concentrations can give rise to undesirable effects like reduction of the fluorescence lifetime and cooperative upconversion [5-7], leading to an increase in the pump power required for optical gain. We have shown in chapter 2 that the luminescence lifetime of Er in sodalime silicate glass is higher than 10 ms for Er concentrations up to 0.2 at.% [8]. Above 0.2 at.%, significant concentration

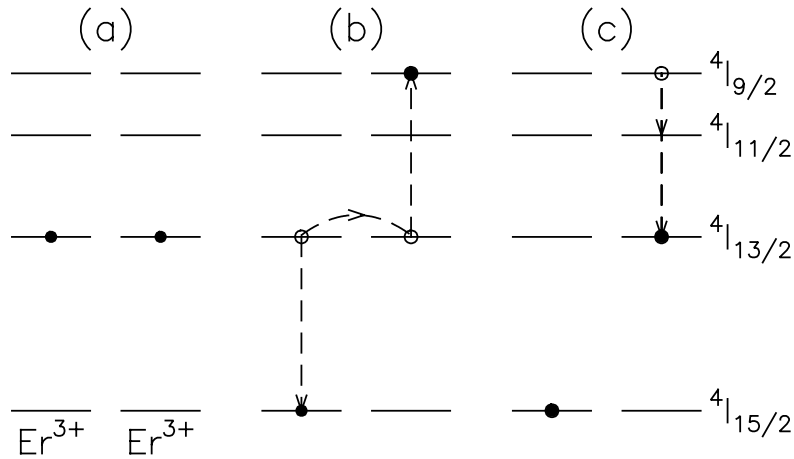


FIGURE 1: Schematic representation of two-particle cooperative upconversion. The horizontal lines represent Stark manifolds of the $4f$ levels of Er^{3+} . The solid dots indicate to which of the four states the Er^{3+} ions are excited. The dashed arrows indicate non-radiative transitions. (a) Two ions are excited to the metastable ${}^4I_{13/2}$ manifold. (b) Energy transfer from one Er ion to the other. (c) The remaining excited Er ion rapidly decays back to the ${}^4I_{13/2}$ manifold.

quenching was observed, due to energy migration which results from a resonant interaction between excited and non-excited Er ions.

In this chapter, we will focus on cooperative upconversion effects. Cooperative upconversion is a process in which two Er ions which are both excited to the ${}^4I_{13/2}$ manifold (see Fig. 1) interact. One Er ion transfers its energy to the other, leaving itself in the ground manifold (${}^4I_{15/2}$), and the other ion in the ${}^4I_{9/2}$ manifold. The remaining excited Er ion rapidly decays back to the ${}^4I_{13/2}$ state via non-radiative decay channels, producing heat, or it decays directly to the ground state by emission of a photon. The upconversion process is nearly resonant, and therefore the upconversion rate depends on the absorption- and emission spectra of Er^{3+} manifolds in the host, and the phonon spectrum of the host. Cooperative upconversion effects are only observable when the pump intensity is high enough to maintain a high concentration of excited Er ions. High pump intensities (up to 10^5 W/cm^2) can be reached using a continuous-wave laser, by confining the light in an optical waveguide with a $1 - 10 \mu\text{m}$ mode diameter. Although upconversion is a very important process in planar amplifiers, hardly any quantitative information concerning upconversion coefficients of Er in silica is available in the literature.

We use ion implantation to dope sodalime silicate glass with Er. By selecting the implantation energy, the Er depth profile can be accurately tuned to the optical mode profile. Also in the lateral direction, Er can be localized in the waveguides by implantation through a mask that can subsequently be used to define waveguides. The advantage of tuning the Er profile to the mode profile is that lower pump powers

are required to obtain optical gain. On a microscopic scale, ion implantation may lead to a locally homogeneous distribution of Er without clustering. Low-loss fiber-compatible channel waveguides can easily be fabricated into sodalime glass using a $\text{Na}^+ \leftrightarrow \text{K}^+$ ion exchange process [9]. A further advantage of this multicomponent glass is that it can accommodate high concentrations of Er without clustering [2,8].

The cooperative upconversion coefficient of Er implanted in sodalime glass is determined in this article, using measurements of the $1.54 \mu\text{m}$ photoluminescence intensity and decay in Er-doped waveguides, following excitation with a $1.48 \mu\text{m}$ source. This pump wavelength, with which Er is directly excited to the metastable $^4I_{13/2}$ manifold, provides the simplest pump scheme for a study of upconversion. The effect of upconversion on optical amplification is shown and discussed.

2. Experimental

Commercially available sodalime silicate glass,^a 1 mm thick, was successively implanted on one side with $0.6 \times 10^{16} \text{ Er/cm}^2$ at 3.0 MeV and $1.2 \times 10^{16} \text{ Er/cm}^2$ at 5.0 MeV while the sample was kept at 300°C to avoid surface roughening [10]. The sample was then annealed at 512°C for 1 hr in air. Subsequently, a thin Al film was deposited and – using photolithographical techniques – $5 \mu\text{m}$ wide channels were etched in the Al. Channel waveguides were then defined by $\text{Na}^+ \leftrightarrow \text{K}^+$ ion-exchange in the Er implanted glass, as well as in unimplanted glass for reference. In this process, the samples were immersed in molten KNO_3 at 375°C for 3.5 hr. After etching off the Al mask, a transparent silicone resin cladding (refractive index 1.43) was deposited, and the endfaces of the sample were polished. The length of the resulting Er-implanted channel waveguides was 3.0 cm. Single mode optical fibers were aligned with the polished endfaces of the waveguides, and fixed using UV-hardening acrylate. The fiber to sample coupling loss was estimated to be 2 – 3 dB at $1.5 \mu\text{m}$.

The geometry of the Er implanted waveguide is shown in Figure 2. The circles show the erbium concentration profile as a function of depth in the waveguide. The profile was determined using Rutherford backscattering spectrometry (RBS) using 4.0 MeV $^4\text{He}^+$ and a scattering angle of 160° . It consists of two overlapping Gaussian distributions, resulting in an average Er concentration of 0.2 at.% ($1.4 \times 10^{20} / \text{cm}^3$) at a depth ranging from ~ 1.0 to $2.1 \mu\text{m}$. The solid line shows the typical refractive index profile after $\text{Na}^+ \leftrightarrow \text{K}^+$ ion exchange, relative to the index of bulk sodalime glass (1.50). Mode-angle spacing measurements on an ion exchanged waveguide in sodalime glass show that the typical index increase at the surface is $\sim 0.8 \%$ [11]. A calculated intensity distribution of the guided optical mode at $1.5 \mu\text{m}$ (through the center of the channel waveguide) as a function of depth is shown in Fig. 2 by the dashed line [12], for the case that a cladding layer is deposited. The lateral width of

^a Fisher Premium sodalime glass, with composition (in mol.%) 72.2 SiO_2 , 14.3 Na_2O , 6.4 CaO , 1.2 K_2O , and small quantities of other oxides.

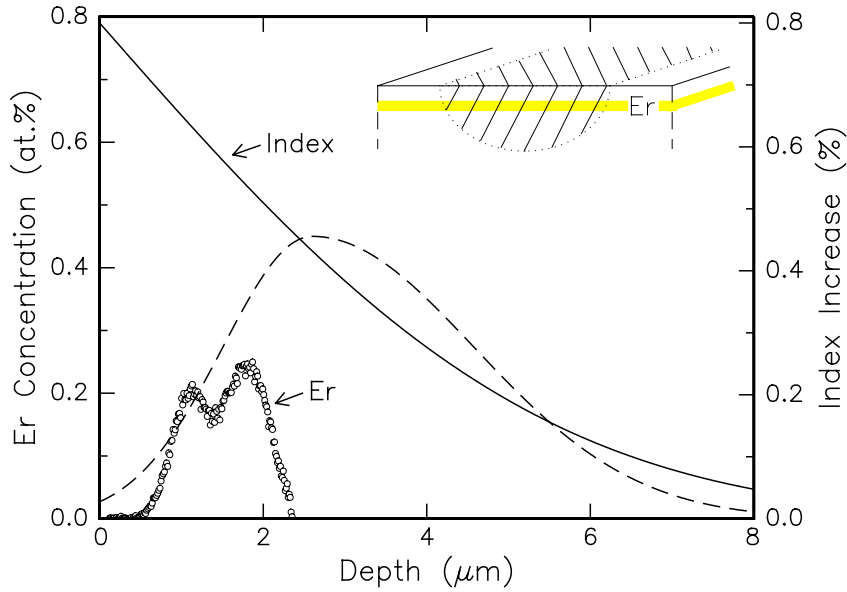


FIGURE 2: Erbium concentration as a function of depth, measured using RBS (circles). The average concentration in the waveguide is 0.2 at.%, corresponding to 1.4×10^{20} at./cm³. For comparison a typical refractive index profile for $\text{Na}^+ \leftrightarrow \text{K}^+$ ion exchanged waveguides is included (drawn line). The dashed line is a calculated normalized optical intensity profile in the center of the channel waveguide for a wavelength of $1.5 \mu\text{m}$. The inset shows a cross sectional view of the waveguide: the shaded area shows the Er implanted region, the hatched area enclosed by the surface and the dotted ellipsoid indicates the ion exchanged region, i.e. the waveguide.

the mode – which depends on the width of the channels on the Al mask during the ion exchange process – was $\sim 10 \mu\text{m}$, comparable to that of standard silica optical fibers. A schematic cross section of the waveguide and the Er doping profile is shown in the inset of Fig. 2.

Photoluminescence (PL) spectroscopy was performed by pumping the waveguides with powers ranging from $18 \mu\text{W}$ to 23mW using a Philips InGaAsP laser operating at $1.48 \mu\text{m}$. The pump light is absorbed high in the $^4I_{13/2}$ manifold of Er^{3+} (see Fig. 1), from where the energy almost instantaneously thermally equilibrates over the $^4I_{13/2}$ sublevels. The Er PL signal was collected perpendicular to the direction of the waveguide using a lens, spectrally analyzed with a 48 cm monochromator, and detected with a liquid-nitrogen-cooled Ge detector or a cooled (-30°C) photomultiplier tube. The pump light was mechanically chopped at 12 Hz, and spectra were recorded using a lock-in amplifier. Time-resolved luminescence decay measurements were performed by switching off the pump light when the PL signal was in steady state. Decay data were recorded using the Ge detector (time resolution $30 \mu\text{s}$) and averaged with a digital storage oscilloscope.

Signal gain measurements were performed using a continuous pump source (at

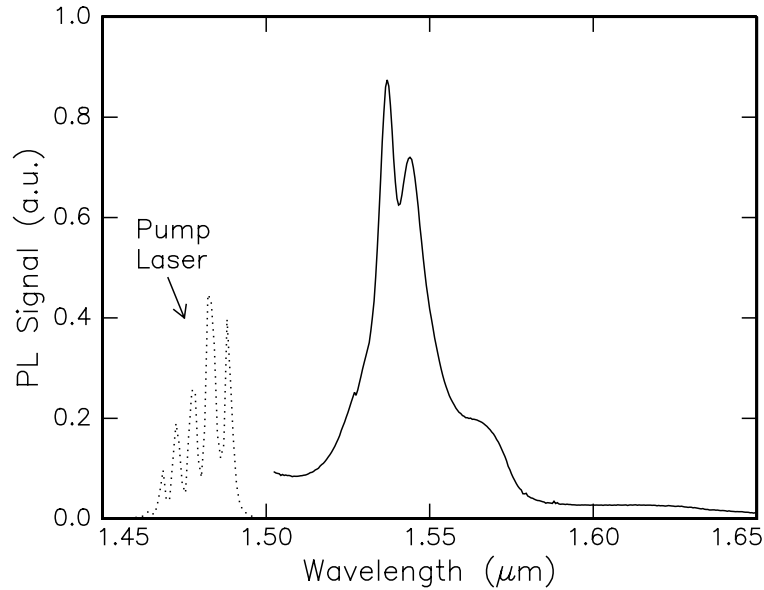


FIGURE 3: Room-temperature photoluminescence spectrum of an Er-implanted sodalime silicate glass channel waveguide (drawn line), measured with a resolution of 0.4 nm. The spectrum of the excitation laser (dotted line) is shown on a strongly reduced scale.

1.48 μm), while a signal from a tunable external cavity laser (in the range of 1.523 – 1.558 μm), chopped at 1 kHz, propagated in opposite direction. Fiber wavelength demultiplexers were used to mix and separate pump and signal wavelength, and signal transmission change data were recorded using an InGaAs detector and lock-in detection. The signal power was varied between 6 nW and 60 μW .

3. Cooperative upconversion

3.1 Results and analysis

Figure 3 shows the PL spectrum between 1.50 and 1.65 μm of the Er-implanted channel waveguide. The spectrum of the 1.48 μm excitation laser is also included in the figure (dotted line). The PL spectrum peaks at 1.537 and 1.545 μm . This emission spectrum is characteristic for intra- $4f$ transitions between the $^4I_{13/2}$ and $^4I_{15/2}$ manifolds of Er^{3+} [13], and is consistent with the data in Chapter 2. The shape of the spectrum around 1.54 μm was independent of pump power, and for none of the employed powers (up to 23 mW, i.e. 30 kW/cm^2)^b luminescence was detected around 800 and 980 nm, associated with the $^4I_{9/2} \rightarrow ^4I_{15/2}$ and $^4I_{11/2} \rightarrow ^4I_{15/2}$ transitions [13] (see Fig. 1). No green or other visible emission was observed either.

^b Pump powers inside the waveguide were obtained by subtracting 2.5 dB insertion loss from the launched pump power.

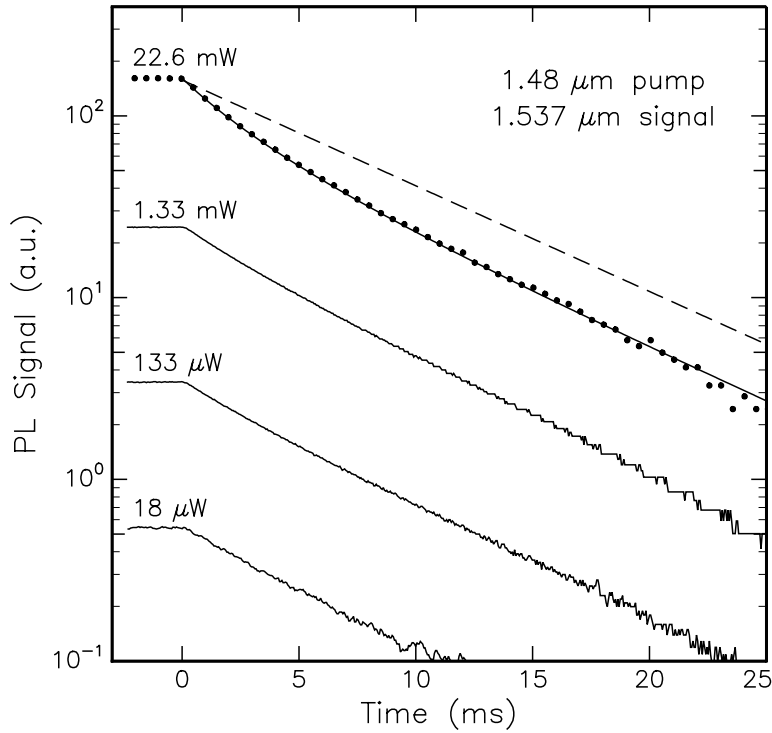


FIGURE 4: PL decay curves following pumping to steady state using $1.48\ \mu\text{m}$ excitation at 0.018, 0.133, 1.33, and 22.6 mW in an Er-implanted sodalime silicate channel waveguide, measured at $1.537\ \mu\text{m}$. The pump was switched off at $t = 0$. A power of 22.6 mW corresponds to an intensity in the waveguide of $\sim 30\ \text{kW}/\text{cm}^2$. A calculation according to Eq. (2), yielding $C = 3.2 \times 10^{-24}\ \text{m}^3/\text{s}$, is shown as a solid line through the dots. The dashed line shows a single exponential decay with $\tau = 7.2\ \text{ms}$.

Figure 4 shows PL decay measurements at $1.537\ \mu\text{m}$, following pumping to steady state using different pump powers in the range from $18\ \mu\text{W}$ to 22.6 mW. As can be seen, almost single exponential decay with a lifetime τ of 7.2 ms is observed for powers up to 1 mW. When the pump power is increased further, a faster component becomes visible in the decay curve. After 22.6 mW excitation, the e^{-1} decay time is 25% shorter than after low power excitation, whereas the slow component in the decay remains 7.2 ms.

The fast components in the PL decay after pumping at high intensities are explained in terms of cooperative upconversion [6], in which one excited Er ion is promoted to the ${}^4I_{9/2}$ state at the cost of the ${}^4I_{13/2}$ excitation of another Er ion (see Fig. 1). Subsequently, either the ${}^4I_{13/2}$ level will be repopulated via non-radiative relaxation from the ${}^4I_{9/2}$ manifold, or a direct (radiative) transition occurs to the ground manifold resulting in 800 or 980 nm emission. As no 800 or 980 nm emission is observed, the lifetimes of the ${}^4I_{9/2}$ and ${}^4I_{11/2}$ manifolds are thought to be short.

In that case rate equations for a two-level system can be used to describe the fraction n_2 of Er^{3+} ions in the ${}^4I_{13/2}$ level:

$$\frac{dn_2}{dt} = R_{\uparrow}(1 - n_2) - R_{\downarrow}n_2 - \frac{n_2}{\tau} - \rho C n_2^2. \quad (1)$$

Here, τ is the spontaneous decay time resulting from radiative and non-radiative decay for the case without upconversion, R_{\uparrow} and R_{\downarrow} are the rates of absorption and stimulated emission of $1.48 \mu\text{m}$ pump light, ρ is the Er density, and C the homogeneous upconversion coefficient. The effect on n_2 due to amplification of spontaneous emission (ASE) is neglected. Upconversion is described by a quadratic term, as it involves two excited Er ions. The following relations were used: $R_{\uparrow} = I_p \sigma_a / h\nu_p$ and $R_{\downarrow} = I_p \sigma_e / h\nu_p$, where $h\nu_p$ is the pump photon energy, σ_a and σ_e the absorption and emission cross sections at $1.48 \mu\text{m}$ [14], and I_p the pump intensity which is estimated using an average mode diameter of $\sim 10 \mu\text{m}$ [12]. Note that the stimulated emission term $R_{\downarrow}n_2$ of pump light has to be included because the pump laser spectrum partly overlaps with the ${}^4I_{13/2} \rightarrow {}^4I_{15/2}$ emission spectrum of Er^{3+} . The measured PL signal is proportional to n_2 . The time evolution of the PL signal after switching off the pump source ($R_{\uparrow} = R_{\downarrow} = 0$) at $t = 0$, is found by solving Eq. (1):

$$n_2(t) = \frac{1}{\tau} \left[\left(\frac{1}{\tau n_2(0)} + \rho C \right) \exp(t/\tau) - \rho C \right]^{-1}, \quad (2)$$

where $n_2(0)$ is the fraction of Er^{3+} which is excited in the ${}^4I_{13/2}$ manifold at $t = 0$. At low pump powers, upconversion effects become negligible, and Eq. (2) reduces to a single exponential with lifetime τ , which was determined to be 7.2 ms. Equation (2), with τ fixed at 7.2 ms, can now be used to fit the decay curves in Fig. 4 for all pump powers with C as free parameter, if $n_2(0)$ is known at each pump power. The decay measurements in Fig. 4 were made after the Er was pumped to steady state. Therefore $n_2(0)$ can be obtained as a function of pump power from measurements of the steady state PL intensity. These data are shown in Fig. 5 (circles), and clearly show a sub-linear behavior, resulting from a combined effect of cooperative upconversion and depletion of the ${}^4I_{15/2}$ ground manifold. In our two-level description, $n_2(0)$ can be derived from Eq. (1) by setting $dn_2/dt = 0$. This yields

$$n_2 = \frac{R_{\uparrow} + R_{\downarrow} + 1/\tau}{2\rho C} \left(\sqrt{1 + \frac{4\rho C R_{\uparrow}}{(R_{\uparrow} + R_{\downarrow} + 1/\tau)^2}} - 1 \right) \equiv n_2(0). \quad (3)$$

A value for the upconversion coefficient C can now be found so that Eqs. (2) and (3) consistently describe the PL intensity (Fig. 5) and PL decay curves (Fig. 4) for all pump powers. The drawn lines in Figs. 4 and 5 are calculated using $C = 3.2 \times 10^{-24} \text{ m}^3/\text{s}$. A constant scaling factor was used to convert from n_2 to the arbitrary PL units in Figs. 4 and 5. As can be seen, good agreement with the data is obtained. The estimated accuracy of the value for C found in this way is $\sim 25\%$.

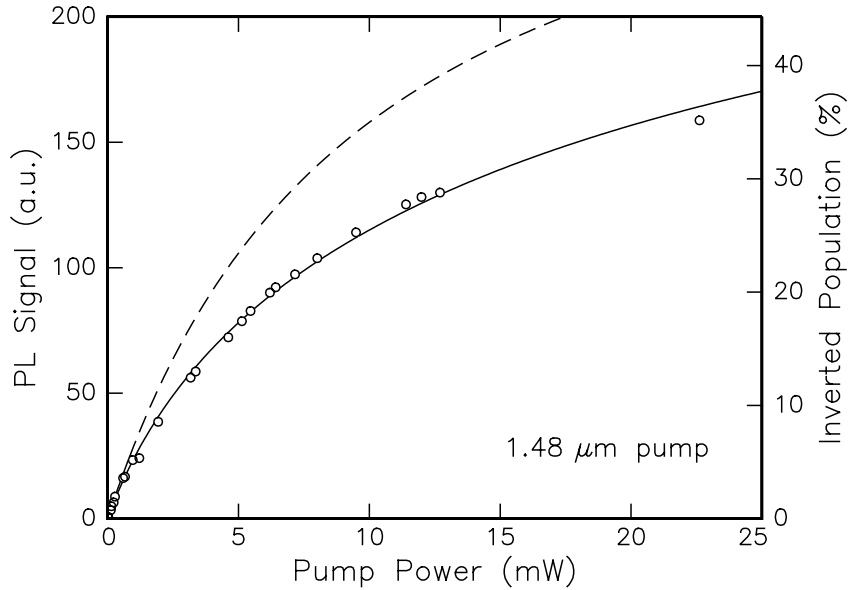


FIGURE 5: PL intensity at $\lambda = 1.536 \mu\text{m}$ measured as a function of pump power inside the waveguide. The highest measured power corresponds to an intensity of $\sim 30 \text{ kW/cm}^2$. The solid line is a calculation based on Eq. (3); the fraction of excited Er ions that follows from the calculation is shown on the right hand axis. For comparison, the dashed line shows a calculation using the same parameters, but with $C = 0$ (no upconversion).

The calculated fraction of excited Er ions, $n_2(0)$, is shown on the right hand axis of Fig. 5. For comparison, the dashed line in Fig. 4 shows a single exponential decay with $\tau = 7.2 \text{ ms}$ in absence of upconversion ($C = 0$). The dashed line in Fig. 5 shows a calculation of the PL intensity, for the case $C = 0$. The sublinear behavior is then only due to depletion of the ground manifold; the effect of upconversion in the data is clearly visible.

3.2 Discussion

Other work, in which Er-doped sodalime glass waveguides were fabricated using RF sputter deposition [15], has yielded a homogeneous upconversion coefficient of $3 \times 10^{-24} \text{ m}^3/\text{s}$, similar to the value we find here. This implies that the local environment and distribution in Er-implanted sodalime glass is the same as that in the sputtered glass. Er-implanted phosphorous silicate glass (P-glass) yielded an upconversion coefficient of $9 \times 10^{-23} \text{ m}^3/\text{s}$ [15], 30 times higher than in Er-implanted sodalime glass. A similar high upconversion coefficient of $\sim 10^{-22} \text{ m}^3/\text{s}$ is reported for highly Er-doped Ge/Al/P-doped fused silica fibers [16]. The difference in upconversion coefficients may be explained by a difference in overlap between the ${}^4I_{13/2} \rightarrow {}^4I_{15/2}$ emission and ${}^4I_{13/2} \rightarrow {}^4I_{9/2}$ absorption spectra, which is higher in these P-doped glasses than in sodalime glass. The upconversion transition to the ${}^4I_{9/2}$ manifold

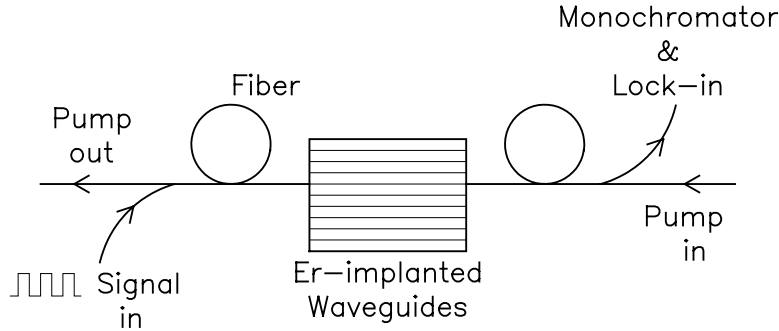


FIGURE 6: Schematic overview of a signal amplification measurement in an Er-implanted planar waveguide. A chopped signal at $1.536\ \mu\text{m}$ propagates in opposite direction as the $1.48\ \mu\text{m}$ pump beam. Fiber wavelength demultiplexers are used to mix and separate pump and signal beams. The signal is measured using a monochromator, detector and a lock-in amplifier.

($\sim 800\ \text{nm}$) is not resonant with twice the peak emission wavelength from the ${}^4I_{13/2}$ manifold ($\sim 1537\ \text{nm}$). Therefore the relative intensity of the long-wavelength tail of the ${}^4I_{13/2} \rightarrow {}^4I_{15/2}$ emission spectrum is important. Indeed, the room temperature PL spectrum of Er in P-glass [17,18] shows a more intense shoulder around $1.600\ \mu\text{m}$ than is the case for Er in sodalime glass [8]. Such a difference is also observed in low-temperature spectra [19].

The data presented in this chapter can be explained using the assumption that the Er is distributed uniformly on the atomic scale (i.e. homogeneous upconversion). In Chapter 2 we have shown that all ions remained optically active for at least up to an implanted Er concentration of 2 at.%, meaning that no Er precipitation occurs. The data for the RF sputtered sodalime glass waveguides were also explained assuming a uniform Er distribution [15]. However, in Er-implanted P-glass the analysis of upconversion effects shows that 20 % of the Er ions is bound as ion pairs [15]. Paired ions undergo much stronger upconversion than homogeneously distributed Er ions. This comparison indicates that, regarding upconversion, the sodalime glass is a much better host for high concentrations of Er than P-glass.

4. Optical amplification

4.1 Results and analysis

Optical amplification measurements were performed by coupling a signal beam at $1.536\ \mu\text{m}$ in the (3 cm long) waveguide, in addition to the pump beam at $1.48\ \mu\text{m}$. The signal beam was chopped, and recorded as a function of pump power using a lock-in amplifier (see Fig. 6). Figure 7 shows the signal transmission change as a function of pump power in the waveguide. The output signal with the pump on is plotted relative to the output signal intensity without pumping. Using $\sim 1\ \text{mW}$

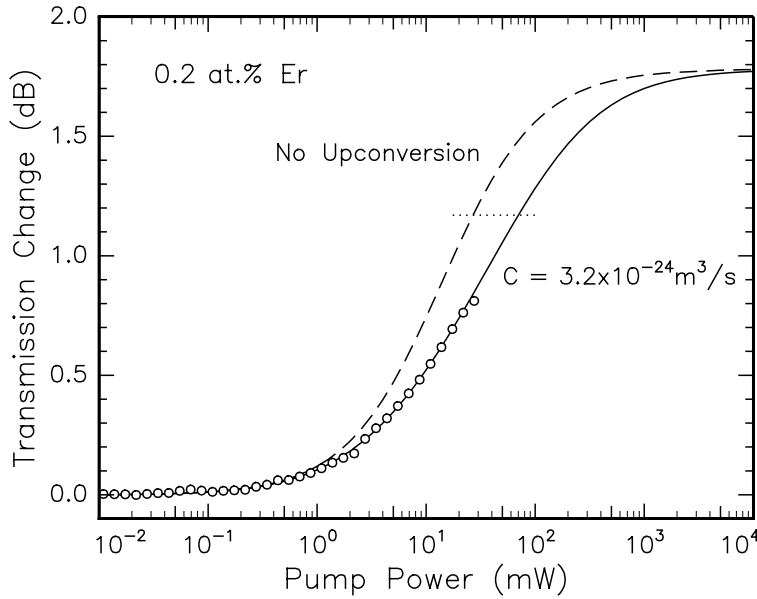


FIGURE 7: Measured transmission change of a $1.536 \mu\text{m}$ signal as a function of $1.48 \mu\text{m}$ pump power in the waveguide (circles). The solid line is a calculation using the measured upconversion coefficient. The dotted line indicates the point at which the signal absorption rate equals the stimulated emission rate. The dashed line shows the calculated gain curve in absence of upconversion.

pump power, a small signal transmission change is measurable, and at 28 mW , a transmission change of 0.8 dB is observed. A gain spectrum was measured (Fig. 8) by varying the signal wavelength between 1.523 and $1.558 \mu\text{m}$. The spectrum peaks at $1.536 \mu\text{m}$, and the full width at half maximum (FWHM) is 17 nm . The transmission change at $1.536 \mu\text{m}$ (using 28 mW pump) was independent of input signal power in the range of $6 \text{ nW} - 60 \mu\text{W}$, indicating that the ${}^4I_{13/2}$ manifold is not measurably depleted by the stimulated emission due to the signal beam. Note that without pumping the total signal loss through the sample is 7.9 dB , consisting of waveguide loss ($2 - 3 \text{ dB}$), coupling losses from fiber to sample ($2 - 3 \text{ dB}$) and from sample to fiber ($2 - 3 \text{ dB}$), and Er absorption ($\approx 1.2 \text{ dB}$). Therefore no net signal gain is achieved with the pump powers that were used.

A numerical model was developed [20], with which the evolution of both a pump and a small signal beam through the Er doped waveguide were calculated. The parameters C , τ , ρ – which were determined in the previous section – were used in the model. The overlap between the Er and the pump intensity distribution is taken as in Sect. 3. The overlap between the Er and the signal intensity distribution was a free parameter in the calculation, thus allowing for differences in guided pump and signal mode diameters. Cross sections for absorption and emission at pump and signal wavelengths were taken from Ref. 14, and a typical value of 1.0 dB/cm was assumed for the intrinsic waveguide loss [9]. Excited state absorption was neglected.

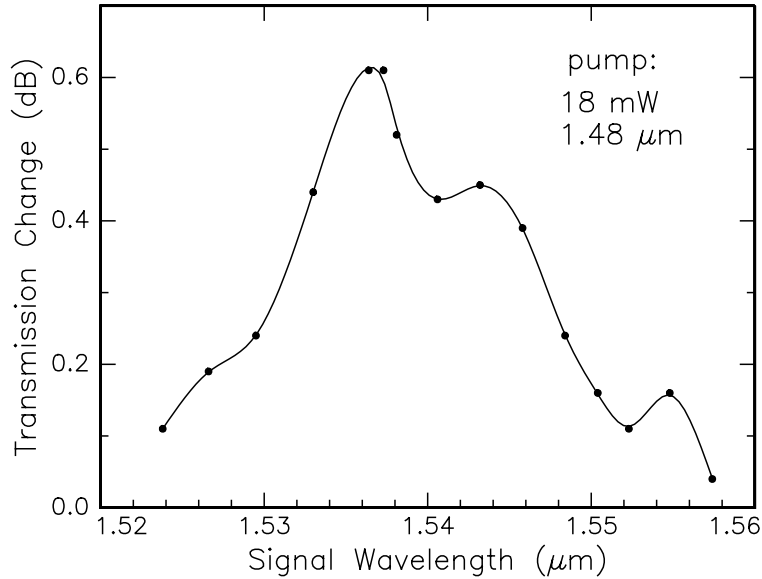


FIGURE 8: Transmission change as a function of signal wavelength. The pump power at $1.48 \mu\text{m}$ was 18 mW . The dots are measured data, the line is a guide for the eye.

A small signal approximation was made, meaning that the pump intensity fully determines the fraction n_2 of inverted Er ions. The calculations were performed using a constant (average) fraction of inversion over the cross section of the waveguide.

The solid line in Fig. 7 shows the result of the numerical calculation. The calculation fits the measured data very well, consistent with the results from the previous section which we obtained from the same waveguide. The unwanted effect of cooperative upconversion becomes clear from comparison with a calculation using the same parameters but without upconversion ($C = 0$, dashed line). Also indicated in the figure (dotted line) is the point at which the rate of signal absorption equals the rate of stimulated emission. The extrapolated pump power that is needed to reach that point is 70 mW . This was not available from the pump laser used. Without upconversion this point would be reached at a power of 25 mW .

4.2 Discussion and possible design improvements

The gain calculation in the previous section yields that the overlap between the signal mode and the Er profile – the only free parameter in the amplification model – is 0.4 times the overlap between the pump mode and the Er. This means that the signal mode is not well confined in the waveguide. Indeed, optical loss measurements as a function of wavelength in this waveguide (not shown) indicate that the cut-off wavelength in the Er implanted ion exchanged waveguides is at $1.540 \mu\text{m}$, close to the signal wavelength. This results in bad confinement of the light. The cut-off wavelength of the waveguides fabricated simultaneously in unimplanted sodalime

glass was above $1.6\ \mu\text{m}$. Apparently, the ion exchange parameters have changed as a result of the Er implantation. This may be due to selective outdiffusion of Na during implantation [21], which results in a lower K concentration after ion exchange, and therefore to a lower refractive index increase. The Er implanted waveguides may therefore be improved simply by performing the ion exchange for longer times, extending the cut-off to a longer wavelength. We estimate that the overlap between the signal mode-field and the Er profile doubles in waveguides with appropriate cut-off wavelength, resulting in an increased gain.

A second possible improvement that can be made is to increase the amount of Er in the waveguide. An increase in concentration leads to an undesirable reduction in the PL lifetime, as is shown in Chapter 2. However, the amount can be increased threefold without increasing the Er concentration by extending the Er profile into the depth, as can be seen in Fig. 2.

As a third suggestion for improvement, it is interesting to consider the pump wavelength. In the $1.48\ \mu\text{m}$ resonant pumping scheme as used here, the high power limit of Eq. (3) shows that the maximum degree of inversion is ~ 0.67 , due to stimulated emission by pump photons. This is a serious limitation for optical gain, despite advantages of this pump wavelength, such as low coupling and propagation losses. With 980 nm pumping (i.e. excitation to the ${}^4I_{11/2}$ manifold) near full population inversion can be reached. However, there may be additional depletion of the ${}^4I_{13/2}$ manifold due to excited state absorption of 980 nm photons leading to excitation of the ${}^4F_{9/2}$ level [13]. In our case, since the lifetimes of the levels above the ${}^4I_{13/2}$ manifold are thought to be low, we assume that such depletion is negligible.

The numerical model [20] can now be used to study gain prospects of the Er implanted sodalime channel waveguides, taking into account the three design improvements suggested above: extending the Er profile $3\times$ deeper in the waveguide, better overlap between pump and signal mode, and pumping at 980 nm. Figure 9 (dashed line) shows the result of the calculation of net signal gain for an Er concentration of 0.20 at.%, and a measured lifetime of 7.2 ms. The calculation takes into account a waveguide loss of 1.0 dB/cm (arrow in Fig. 9); furthermore, cooperative upconversion is included using $C = 3.2 \times 10^{-24}\ \text{m}^3/\text{s}$ as obtained in Sect. 3. As can be seen in Fig. 9, using 200 mW of 980 nm pump, a modest net gain of 3.0 dB (1.0 dB/cm) is achievable, enough to compensate the intensity loss in for instance a Y-splitter. The negative gain of nearly $-12\ \text{dB}$ at 0 pump power is due to the waveguide loss (3 dB) and the absorption by Er (9 dB). A calculation using a pump wavelength of $1.48\ \mu\text{m}$ (solid line) is also shown; no net gain is achievable in this way for pump powers below 300 mW.

Recently, Er-doped P-glass waveguides have been made by flame hydrolysis [22] and plasma-enhanced chemical vapour deposition (PECVD) [17], and show 0.65 and 0.33 dB/cm net gain, respectively, using $\sim 400\ \text{mW}$ pump power at 980 nm. These gain numbers – which are slightly lower than the $\sim 1\ \text{dB/cm}$ which would be

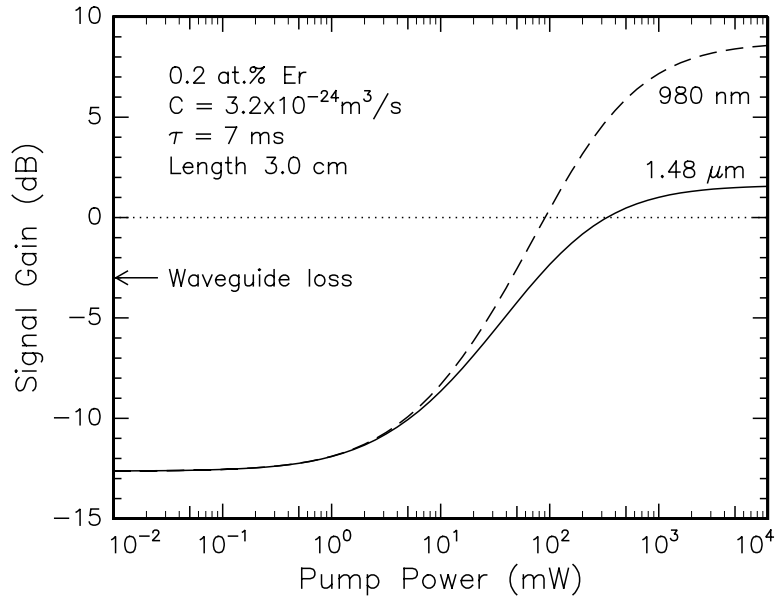


FIGURE 9: Calculated gain at $1.536 \mu\text{m}$ as a function of pump power in a 3 cm long waveguide, based on the design specifications given in the text. The waveguide loss (no Er) of 1.0 dB/cm is indicated by an arrow. The Er concentration is 0.2 at.%, the total amount of Er is $6 \times 10^{16} / \text{cm}^2$. The upconversion coefficient ($3.2 \times 10^{-24} \text{ m}^3/\text{s}$) and PL lifetime (7.2 ms) were determined in Sect. 3. The solid line shows the result for a $1.48 \mu\text{m}$ pump, and the dashed line for a 980 nm pump. Using 200 mW, a net gain of 3.0 dB can be achieved.

achievable in our sodalime waveguides – were obtained using only ~ 0.07 at.% Er, in order to avoid concentration quenching and to reduce cooperative upconversion [22]. Net gain was still feasible in those experiments due to the extremely low waveguide loss of only 0.2 dB/cm, as opposed to the ~ 1 dB/cm in our ion exchanged waveguide.

Measurements on Er-doped sodalime glass waveguides made using RF sputter deposition [23] have shown a net signal gain of 3.3 dB/cm at 280 mW; three times higher than calculated here. This difference may partly be explained by a difference in waveguide loss and diameter, and partly by a difference in the trade-off between Er concentration and PL lifetime. The effect of these parameters on the optical gain will be discussed in Chapter 6. The advantage of ion implantation is that the Er-profile can be centered at the optical mode in the waveguide, thereby reducing unwanted signal absorption in the tails of the optical modes. This will reduce the pump threshold for gain.

5. Conclusions

Ion-exchanged optical waveguides were fabricated in MeV Er implanted sodalime glass. Both the photoluminescence (PL) intensity and PL decay as function of time were measured in a channel waveguide, after excitation at $1.48 \mu\text{m}$ with pump inten-

sities up to ~ 30 kW/cm². The decay for low pump intensity is almost single exponential with $\tau = 7.2$ ms, whereas for high pump intensities a faster non-exponential decay is observed. This is explained in terms of a homogeneous upconversion effect; the upconversion coefficient is found to be $(3.2 \pm 0.8) \times 10^{-24}$ m³/s. This value is 30 times less than that observed for Er in phosphorous silicate glasses, which is partly attributed to the difference between the spectral shapes of the Er³⁺ manifolds of the two materials. Upconversion is unavoidable, and therefore it determines a fundamental limit to the optical gain per unit length in Er-based amplifiers. An extrapolation of measured optical signal gain shows that 1 dB/cm net gain is achievable in the present Er-implanted sodalime glass.

References

- [1] E. Desurvire, *Physics Today* **47** (1), 20 (1994).
- [2] B. J. Ainslie, *J. Lightwave Technol.* **9**, 220 (1991).
- [3] E. Desurvire, J. R. Simpson, and P. C. Becker, *Opt. Lett.* **12**, 888 (1987).
- [4] C. H. Henry, G. E. Blonder, and R. F. Kazarinov, *J. Lightwave Technol.* **7**, 1530 (1989).
- [5] W. J. Miniscalco, *J. Lightwave Technol.* **9**, 234 (1991).
- [6] J. C. Wright, in *Radiationless processes in Molecules and Condensed Phases*, edited by F. K. Fong (Springer, Heidelberg, 1976), Chapter 4.
- [7] G. Nykolak, P. C. Becker, J. Shmulovich, Y. H. Wong, D. J. DiGiovanni, and A. J. Bruce, *IEEE Phot. Techn. Letts.* **5**, 1014 (1993).
- [8] Chapter 2 of this thesis; E. Snoeks, G. N. van den Hoven, and A. Polman, *J. Appl. Phys.* **73**, 8179 (1993).
- [9] J. J. G. M. van der Tol, J. W. Verhoof, M. B. J. Diemeer, and E. C. M. Pennings, *Electron. Lett.* **27**, 379 (1991).
- [10] Chapter 8 of this thesis; E. Snoeks, T. Weber, A. Cacciato, and A. Polman, submitted to *J. Appl. Phys.*
- [11] E. Snoeks, G. N. van den Hoven, A. Polman, B. Hendriksen, and M. B. J. Diemeer, *Proc. Europ. Conf. Integr. Opt.*, Neuchâtel, Switzerland 1993, 3-38.
- [12] N. H. G. Baken, M. B. J. Diemeer, J. M. van Splunter, and H. Blok, *J. Lightwave Technol.* **8**, 576 (1990).
- [13] S. Hübner, *Optical Spectra of Transparent Rare-Earth Compounds* (Academic Press, New York, 1978).
- [14] $\sigma_a = 1.0 \times 10^{-21}$ and $\sigma_e = 0.5 \times 10^{-21}$ cm² at 1.48 μ m, and $\sigma_a = 4.1 \times 10^{-21}$ and $\sigma_e = 5.0 \times 10^{-21}$ cm² at 1.536 μ m; L. Cognolato, C. De Bernardi, M. Ferraris, A. Gnazzo, S. Morasca, and D. Scarano, *CSELT Techn. Rep.* **XIX**, 277 (1991), and W. J. Miniscalco, *J. Lightwave Technol.* **9**, 234 (1991).
- [15] A. M. Vredenberg and J. Shmulovich, Private communication.
- [16] P. Blixt, J. Nilsson, T. Carlнас, and B. Jaskorzynska, *IEEE Phot. Techn. Letts.*

- 3**, 996 (1991).
- [17] K. Shuto, K. Hattori, T. Kitagawa, and M. Horiguchi, Proc. 19th Europ. Conf. on Opt. Comm., Montreux, Switzerland, 1993, 53.
- [18] A. Polman, D. C. Jacobson, D. J. Eaglesham, R. C. Kistler, and J. M. Poate, J. Appl. Phys. **70**, 3778 (1991).
- [19] S. Zemon, G. Lambert, L. J. Andrews, W. J. Miniscalco, B. T. Hall, T. Wei, and R. C. Folweiler, J. Appl. Phys. **69**, 6799 (1991).
- [20] See Sect. 2 in Chapter 6 of this thesis.
- [21] P. Mazzoldi and G. W. Arnold, in *Ion Beam Modification of Insulators*, edited by P. Mazzoldi and G. W. Arnold (Elsevier, Amsterdam, 1987), Chapter 5.
- [22] T. Kitagawa, K. Hattori, K. Shuto, M. Yasu, M. Kobayashi, and M. Horiguchi, Tech. Dig. Topical Meeting on Optical Amplifiers and Applications, Santa Fe, NM, 1992, PD-1; T. Kitagawa, K. Hattori, M. Shimizu, Y. Ohmori, M. Kobayashi, and M. Horiguchi, Electron. Lett. **28**, 1818 (1992).
- [23] G. Nykolak, M. Haner, P. C. Becker, J. Shmulovich, and Y. H. Wong, IEEE Phot. Techn. Letts. **5**, 1185 (1993).

Chapter 6

Optimization of an Er-doped sodalime glass optical waveguide amplifier

The optical gain of an Er-doped optical waveguide amplifier is lowered by concentration quenching and cooperative upconversion, of which the parameters were determined in Chapters 2 to 5. In this chapter we show how much the gain performance can be improved when each of these deteriorating effects is reduced. The effect of lowering the waveguide loss and reducing the optical mode diameter is also demonstrated.

1. Introduction

In Chapters 2 to 5 of this thesis, the optical properties of Er-implanted sodalime silicate glass have been investigated. The radiative decay rate of the $1.54\ \mu\text{m}$ transition in Er^{3+} was determined to be $45\ \text{s}^{-1}$ [1], corresponding to a PL lifetime of 22 ms. Two Er-concentration dependent photoluminescence (PL) quenching mechanisms which lower the PL lifetime were found to be significant: 1) concentration quenching due to excitation migration from excited Er ions to unexcited Er ions, followed by quenching at hydroxyl impurities [2,3], and 2) cooperative upconversion, in which two excited Er ions interact non-radiatively [2-4]. In this interaction, one Er ion is promoted to a higher lying state, leaving the other in the ground state. This phenomenon becomes significant when the density of excited Er ions is high [5]. Both quenching mechanisms increase the decay rate of the metastable first excited state, thereby lowering the optical gain efficiency.

A calculation in Chapter 5 (Fig. 9), based on all parameters which were measured in Chapters 2 to 5, shows that a maximum gain of $\sim 1.0\ \text{dB/cm}$ may be achieved in an Er-implanted waveguide amplifier using 200 mW pump power at 980 nm. In this chapter, model calculations are presented to study the effect of reducing upconver-

sion or the density of quenching sites on the optical gain. The effect of optimizing the waveguide is also demonstrated.

2. Optical propagation model

In the present Er-implanted sodalime glass waveguides, the pump intensity decreases strongly along the waveguide length, due to waveguide losses and absorption by Er. Also the signal light is affected by waveguide losses. To accurately calculate the optical gain as a function of pump power for a certain waveguide length it is therefore important to first calculate the pump evolution in the Er-implanted waveguides as a function of waveguide length. Our calculations are based on the derivation of Digonnet [6], which we extended to account for cooperative upconversion.

It is assumed that the decay rates from all the higher lying levels to the metastable $^4I_{13/2}$ manifold are high compared to the de-excitation rate of the $^4I_{13/2}$ manifold to the ground manifold [5]. Under this assumption, a set of quasi two-level rate equations is sufficient to describe the populations of the two levels. For the case that the signal intensity is low compared to the pump intensity, the fraction n_2 of Er^{3+} in the metastable $^4I_{13/2}$ level is given by:

$$\frac{dn_2}{dt} = R_{\uparrow}(1 - n_2) - R_{\downarrow}n_2 - \frac{n_2}{\tau} - \rho C n_2^2. \quad (1)$$

Here, τ is the PL lifetime resulting from radiative- and non-radiative decay without upconversion, ρ is the Er density, C the cooperative upconversion coefficient, and R_{\downarrow} and R_{\uparrow} are rates of stimulated emission and absorption, both at the pump wavelength. The excited fraction in steady state is

$$n_2 = \frac{R_{\uparrow} + R_{\downarrow} + 1/\tau}{2\rho C} \left(\sqrt{1 + \frac{4\rho C R_{\uparrow}}{(R_{\uparrow} + R_{\downarrow} + 1/\tau)^2}} - 1 \right). \quad (2)$$

Using $R_{\uparrow} = I_p \sigma_p^a / h\nu_p$ and $R_{\downarrow} = I_p \sigma_p^e / h\nu_p$, with σ_p^a and σ_p^e the pump absorption and emission cross sections, I_p intensity, and $h\nu_p$ the energy of a pump photon [7], Eq. (2) can be used to calculate n_2 as a function of I_p .

The evolution of the pump intensity I_p along the z -axis (light-propagation direction) in the waveguide is determined by a differential equation which consists of contributions from the waveguide loss (α , in units of cm^{-1}), and absorption and stimulated emission due to Er^{3+} :

$$\frac{dI_p}{dz} = -\alpha I_p - \sigma_p^a (1 - n_2) I_p \int \mathcal{P}(x, y) dx dy + \sigma_p^e n_2 I_p \int \mathcal{P}(x, y) dx dy, \quad (3)$$

where

$$\mathcal{P}(x, y) = \rho(x, y) p_0(x, y)$$

in which $p_0(x, y)$ represents the pump intensity distribution across the waveguide, and is normalized such that $\int p_0(x, y) dx dy = 1$. After inserting Eq. (2) – which provides $n_2(I_p)$ – in Eq. (3), the solution $I_p(z)$ may be found by numerical integration. From $I_p(z)$, the fraction n_2 of excited Er^{3+} can then be determined everywhere in the waveguide.

It is then possible to determine the signal evolution. Starting from the differential equation for the normalized signal intensity $s(z)$, which is similar to Eq. (3), using in this case the emission and absorption cross sections at the signal wavelength, and the signal intensity mode $s_0(x, y)$, the gain function $g(z) \equiv \ln[s(z)]$ is found:

$$\frac{dg(z)}{dz} = \frac{ds(z)/dz}{s(z)} = -\alpha - \sigma_s^a(1 - n_2) \int \mathcal{S}(x, y) dx dy + \sigma_s^e n_2 \int \mathcal{S}(x, y) dx dy. \quad (4)$$

$\mathcal{S}(x, y)$ is defined for the signal mode, as $\mathcal{P}(x, y)$ above. This equation can be solved numerically, making use of the evolution of $n_2(z)$ along the waveguide as derived above.

3. Results and discussion

First, calculations will be presented which are performed using the parameters for luminescence lifetime [1,8], the effect of concentration quenching [8], the Er-concentration and doping profile [5], and cooperative upconversion [5] as they were determined in the previous chapters. Cross sections for absorption and emission of pump and signal photons were taken from literature [9]. Then, the effect of changes in several parameters on the optical gain is demonstrated. All calculations were performed for 1 cm long $\text{Na}^+ \leftrightarrow \text{K}^+$ ion exchanged waveguides (mode diameter 6 – 10 μm) and a pump wavelength of 980 nm.

3.1 Effect of removing non-radiative decay sites

Figure 1 shows calculations of the optical gain in a waveguide implanted with Er to a concentration of 0.2 at.% ($1.4 \times 10^{20} \text{ Er/cm}^3$). The full line is a calculation for the case that $0.8 \times 10^{19} / \text{cm}^3$ OH is present in the glass, which is the case in commercially available Fisher Premium sodalime glass [8]. In this case, the PL lifetime is 8.5 ms [8]. The dashed line corresponds to the case that all OH is removed from the silica, in which case the lifetime is expected to be ~ 22 ms [1,8]. In both calculations, the waveguide loss (no Er) is taken to be 1 dB/cm (indicated by an arrow in Fig. 1), and the upconversion coefficient $C = 3 \times 10^{-24} \text{ m}^3/\text{s}$ [5]. As can be seen, removal of OH has only a very small effect on the gain curve. The gain threshold (the minimum pump power to reach net gain) is reduced from 76 to 62 mW (-0.9 dB). At 200 mW pump power, the net optical gain improves from 1.2 to 1.4 dB/cm.

The effect of the removal of OH is small due to the fact that for Er concentrations above $\sim 2 \times 10^{19} \text{ at./cm}^3$, the de-excitation rate is dominated by cooperative

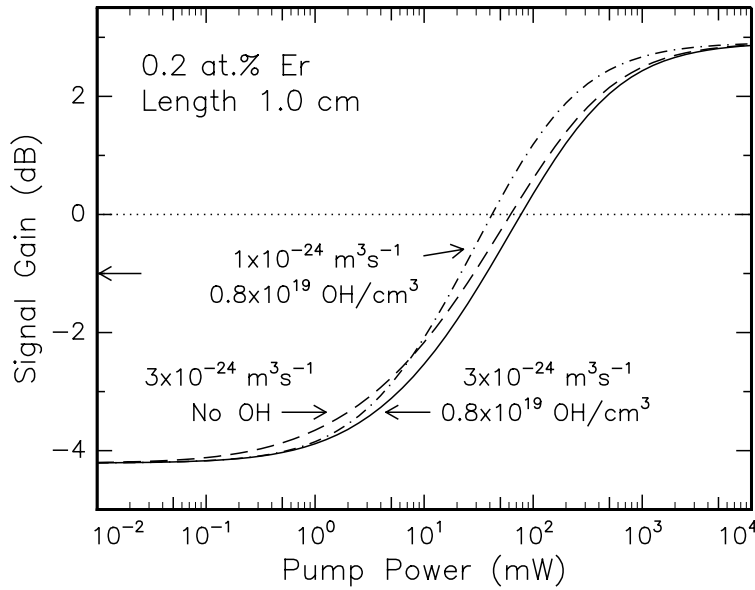


FIGURE 1: Calculated gain as a function of pump power at 980 nm in a 1 cm long waveguide in Fisher Premium sodalime glass. The solid line shows the result for sodalime glass with 0.8×10^{19} OH/cm³. The dashed line corresponds to the case in which no quenching sites are present in the glass. The arrow on the left axis indicates the waveguide loss (1 dB/cm). The Er concentration is 0.2 at.% (1.4×10^{20} at./cm³). In both cases, the measured upconversion coefficient $C = 3 \times 10^{-24}$ m³/s is used (See Ref. 5). The dot-dashed (— · —) line is calculated for $C = 1 \times 10^{-24}$ m³/s (and 0.8×10^{19} OH/cm³).

upconversion. Changing the spontaneous decay rate in highly doped waveguides therefore only has a minor effect on the optical gain. It is more important to focus on achieving low upconversion than to attempt to remove quenching impurities.

3.2 Reduction of upconversion

Figure 1 also shows a gain calculation for the case that the upconversion coefficient is reduced from $C = 3 \times 10^{-24}$ m³/s to $C = 1 \times 10^{-24}$ m³/s (— · — line). As can be seen, this threefold reduction of C has a large effect on the gain threshold power, which reduces from 76 to 43 mW (−2.5 dB). The net gain at 200 mW pump power increases from 1.2 dB/cm to 1.9 dB/cm.

It is therefore important to find host materials that show as low as possible cooperative upconversion. The upconversion coefficient is hard to control; it depends on the spectral overlap between the ${}^4I_{13/2} \rightarrow {}^4I_{15/2}$ and ${}^4I_{13/2} \rightarrow {}^4I_{9/2}$ transitions of Er³⁺, as well as the phonon spectrum in the host. The spectral overlap may be minimized if a glass is used in which the emission spectra are narrow. The effect of upconversion can also be reduced by lowering the Er concentration.

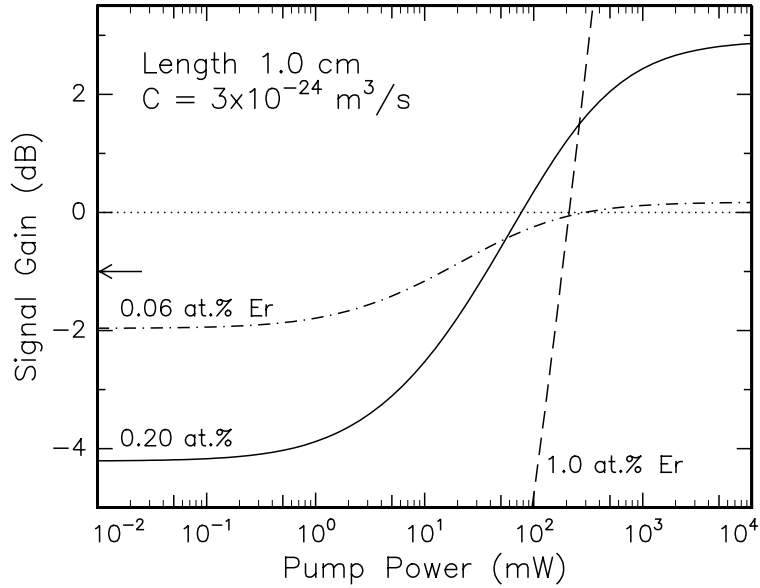


FIGURE 2: Calculations of net optical signal gain as a function of initial pump power at 980 nm, based on parameters measured in this thesis. Three cases are shown, for three Er concentrations: 0.06 at.% (— · — line), 0.20 at.% (solid line), and 1.0 at.% (dashed line). The other parameters are fixed, except for τ , which depends on the Er concentration. The arrow indicates the waveguide loss (1.0 dB/cm).

3.3 Effect of the Er concentration on the gain

In this section we will investigate the effect of increasing or decreasing the Er concentration on optical gain and gain threshold power. Figure 2 shows three gain calculations, using three different Er concentrations (0.06, 0.2 and 1.0 at.%).^a All other parameters were kept fixed, except for the PL lifetime, which depends on the Er density ρ due to concentration quenching as was shown in Chapter 4.^b As can be seen, the maximum achievable gain increases for increasing Er concentration, which is indeed expected under the condition that enough pump power is available to excite all Er. The gain threshold, however, shows a more complicated behavior as a function of Er density. For low Er concentration (0.06 at.%), the gain threshold is high (300 mW) because almost all Er must be inverted in order to produce sufficient signal gain to overcome the waveguide loss of 1.0 dB/cm. When the Er concentration is increased to about 0.2 at.%, net gain may be reached for a lower degree of inversion, resulting in a lower gain threshold power (76 mW). At even higher Er concentration (1.0 at.%) the luminescence lifetime τ decreases strongly due to concentration quenching and upconversion. Therefore, more pump power is required to reach a certain degree of inversion, and the threshold increases to 215 mW.

^a 1 at.% Er in sodalime glass corresponds to a density of $\sim 7 \times 10^{20}$ at./cm³.

^b For Fisher Premium sodalime glass, it was found that $\tau(\rho) = 1/(42 \text{ s}^{-1} + \rho \cdot 4.6 \times 10^{-25} \text{ m}^3/\text{s})$.

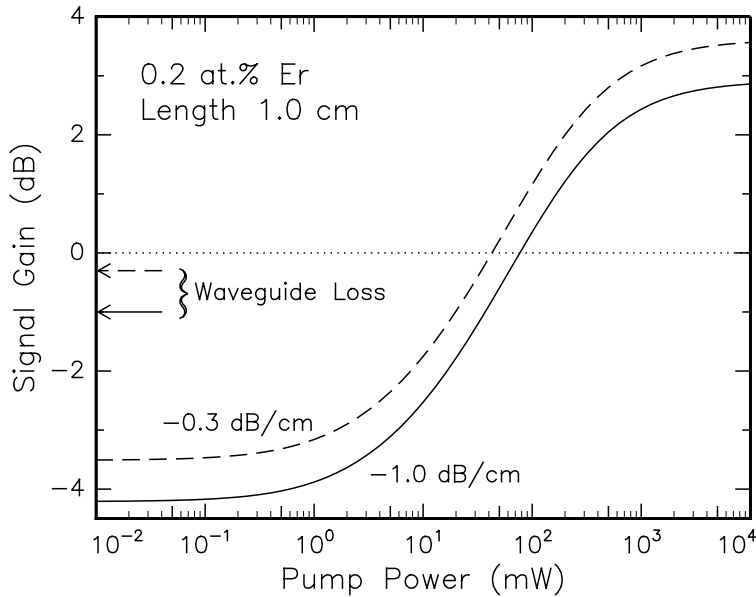


FIGURE 3: Calculation of net optical gain in an Er-doped planar waveguide with 1.0 dB/cm loss (full line), or 0.3 dB/cm loss (dashed line). All other waveguide parameters were the same as those used for the solid line in Fig. 1.

3.4 Optical confinement and waveguide loss

The optical gain and gain threshold of an Er-doped planar waveguide amplifier may also be improved by minimizing the optical losses in the waveguide. For instance, the typical waveguide loss in ion-exchanged optical waveguides is on the order of 0.5–1.0 dB/cm. To first order, any reduction in optical waveguide loss results in an equally large improvement in net gain. This is shown in Fig. 3. The solid line from Fig. 1 is replotted together with the result of a calculation in which the waveguide loss was reduced from 1.0 to 0.3 dB/cm. Net gain is now achieved at 43 mW. The net gain increases over the entire pump power range.

A second and completely different way to improve the optical gain performance is to reduce the dimensions of the optical modes. In this way, higher pump intensities are reached in the waveguide using the same pump power. This principle is used in Er-doped fiber amplifiers, in which the core diameter is ~ 3 μm rather than the $\sim 6 - 10$ μm in standard transmission fibers. In practice, reduction of the optical mode diameter is achieved by defining waveguides with a higher refractive index contrast, leading to stronger optical confinement. With the ion-exchange technique, this can be done by using for instance silver ions instead of potassium ions to define waveguides [10]. Ag^+ ion exchanged waveguides, however, are reported to show more optical loss than K^+ -exchanged waveguides, due to precipitation of Ag. More research is required to develop alternative low-loss high-index ion-exchanged waveguides. If the optical modes could be shrunk to a diameter of 3 μm rather than

the $\sim 10 \mu\text{m}$ which is presently the case, all pump power scales in Figs. 1-3 would be reduced by a factor of 10.

4. Conclusions

The most important Er photoluminescence decay process in highly Er-doped waveguide amplifiers operating at $1.54 \mu\text{m}$ is cooperative upconversion, rather than the spontaneous emission. A threefold reduction of the upconversion coefficient would lead to a twofold reduction of the pump threshold for net gain. Further improvements may be possible by reducing the waveguide propagation loss, as well as by reducing the optical mode dimensions. The concentration that provides the highest possible optical gain is determined by the trade-off between: 1) more signal gain due to a higher Er concentration, and 2) a higher pump threshold for gain due to more cooperative upconversion at high Er concentrations. The optimum Er concentration therefore depends on the amount of available pump power.

References

- [1] Chapter 3 of this thesis; E. Snoeks, A. Lagendijk, and A. Polman, Phys. Rev. Lett. in press.
- [2] F. Auzel, in *Radiationless Processes*, edited by B. DiBartolo (Plenum Press, New York, 1980).
- [3] J. C. Wright, in *Radiationless processes in Molecules and Condensed Phases*, edited by F. K. Fong (Springer, Heidelberg, 1976), Chapter 4.
- [4] W. J. Miniscalco, J. Lightwave Technol. **9**, 234 (1991).
- [5] Chapter 5 of this thesis; E. Snoeks, G. N. van den Hoven, A. Polman, B. Hendriksen, M. B. J. Diemeer, F. Priolo, submitted to J. Opt. Soc. Am. B.
- [6] M. J. F. Digonnet, IEEE. J. Quantum Electron. **26**, 1788 (1990).
- [7] A. Einstein, Ann. Phys. **17**, 132 (1905) [translation: Am. J. Phys. **33**, 367 (1965)].
- [8] Chapter 4 of this thesis; E. Snoeks, P. G. Kik, and A. Polman, submitted to Optical Materials.
- [9] $\sigma_p^a = 1.0 \times 10^{-21}$ and $\sigma_p^e = 0 \times 10^{-21} \text{ cm}^2$ at 980 nm, and $\sigma_s^a = 4.1 \times 10^{-21}$ and $\sigma_s^e = 5.0 \times 10^{-21} \text{ cm}^2$ at $1.536 \mu\text{m}$; L. Cognolato, C. De Bernardi, M. Ferraris, A. Gnazzo, S. Morasca, and D. Scarano, CSELT Techn. Rep. **XIX**, 277 (1991), and W. J. Miniscalco, J. Lightwave Technol. **9**, 234 (1991).
- [10] L. Roß, Glastechn. Ber. **62**, 285 (1989).

Part II

Mechanical properties

Chapter 7

Densification, anisotropic deformation, and plastic flow of SiO_2 during MeV heavy ion irradiation

The response of SiO_2 thin films and implantation masks to 4.0 MeV Xe irradiation is studied. Trenches etched in the silica deform dramatically after irradiation with 3×10^{15} ions/cm². *In-situ* wafer curvature measurements show that thin planar silica films first densify by 3.6 % during irradiation. The resulting stress then relaxes viscously by radiation-enhanced Newtonian flow. At a flux of 3×10^{10} Xe ions/cm²s the measured shear viscosity was 6×10^{13} Pa · s. We find evidence for an irradiation induced anisotropic deformation mechanism in the silica films. In equilibrium, this deformation leads to an average compressive saturation stress as large as 4.5×10^7 Pa.

1. Introduction

General studies of radiation damage in silica have been performed for many years [1], because of the potential use of silica in nuclear reactors and waste containers, and its current use in optical fibers. Some of these studies showed that ion irradiation causes densification of the amorphous SiO_2 , due to both ionization events and atomic collisions [1,2]. The densification eventually saturates with fluence. When a thin film of SiO_2 , constrained by a substrate, is irradiated, densification results in a tensile stress in the irradiated region. Stress can be relieved by radiation enhanced plastic flow, as shown for irradiation with Si and Au at energies below 800 keV [3]. Presently, ion implantation is being used to dope materials with heavy ions at MeV energies [4,5], for instance to modify optical properties. It is therefore important to determine the response of silica to irradiation with heavy ions at MeV energies.

In this chapter we present a study of deformation in amorphous SiO_2 films during 4.0 MeV Xe irradiation at room temperature. Scanning electron microscopy (SEM)

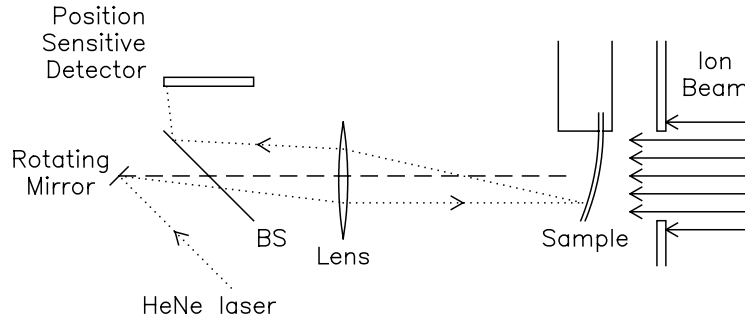


FIGURE 1: Schematic of the experimental setup for measuring the sample curvature during ion irradiation. The rotating mirror and the position sensitive detector are in the focal plane of the lens. BS is a beam splitter. From the angle of the reflected He-Ne laser beam that is scanned up and down on the back of the sample, the radius of curvature is determined while the sample is ion-irradiated at the front.

shows a dramatic macroscopic deformation of trenches in SiO_2 , after irradiation to a fluence above 10^{15} ions/cm². This observation is correlated to *in-situ* wafer curvature measurements of stress in planar SiO_2 films on Si during irradiation. Densification, plastic flow and a non-saturating anisotropic deformation phenomenon are observed.

2. Experimental

Experiments were performed on $1.85\ \mu\text{m}$ thick SiO_2 films, obtained by wet thermal oxidation (at 1100°C) of one side of double-side polished, undoped, (100) Si wafers. Trenches, $1.0\ \mu\text{m}$ deep and $5.0\ \mu\text{m}$ wide, were etched into such an SiO_2 film on a thick substrate ($325\ \mu\text{m}$) using reactive ion etching. The trenches were separated from each other by $15\ \mu\text{m}$. The trenches were studied in cross section by SEM with 12 keV electrons before and after Xe irradiation of the SiO_2 film at 4.0 MeV.

A thin Si substrate ($100\ \mu\text{m}$), also covered with $1.85\ \mu\text{m}$ SiO_2 , was used for *in-situ* stress measurements during ion irradiation. Rectangular pieces ($5 \times 25\ \text{mm}^2$) were cleaved and clamped at one end to a copper block, leaving the other end free to bend. By scanning a He-Ne laser beam up and down on the back of the sample, the sample curvature was measured *in-situ* while the sample was implanted at the front (see Fig. 1). Details of this technique are described in Ref. 6. The integrated in-plane stress S (in N/m) was derived from the measured radius of curvature R , using the Si-substrate thickness t_{Si} and the biaxial elastic modulus Y_{Si} of (100) Si^a [8]:

$$S = \frac{Y_{\text{Si}} t_{\text{Si}}^2}{6R}. \quad (1)$$

The average local stress in the film (σ , in Pascal) can be obtained by dividing the

^a $Y_{\text{Si}} = 181\ \text{GPa}$ (see Ref. 7)

FIGURE 2: Cross section SEM images of a 5.0- μm wide trench in a thermally grown SiO_2 film (a) before irradiation, and after 4.0 MeV Xe irradiation at (b) 1.0×10^{15} , (c) 3.0×10^{15} , and (d) 1.0×10^{16} / cm^2 . All images were taken with the same magnification. The ion beam was directed perpendicular to the surface.

integrated stress by the film thickness. Deviations of the laser beam due to the vacuum viewport and mirrors limited the resolution of the integrated stress measurements to ± 5 N/m. However, local variations in wafer and oxide thickness limit the absolute determination of the integrated stress to ± 15 N/m. The 4.0 MeV Xe^{4+} beam was electrostatically scanned through an aperture, at ion fluxes in the range of $0.8 - 15 \times 10^{10}$ ions/ cm^2s . All irradiations were performed at room temperature. The oxide thickness and ion range and concentration were determined by Rutherford backscattering spectrometry (RBS), using 4.0 MeV $^4\text{He}^+$.

3. Results and discussion

Figures 2a-d shows cross section SEM images of a 5.0 μm wide trench etched into SiO_2 before and after Xe irradiation. The irradiation fluences ranged from 1.0×10^{15} to 1.0×10^{16} Xe/ cm^2 . The silica shows a dramatic macroscopic deformation: the material expands in the plane perpendicular to the ion beam and contracts in the direction along the ion beam. A small effect is first seen in the near-surface region after 1.0×10^{15} / cm^2 . After 3.0×10^{15} / cm^2 the sides of the trench have almost col-

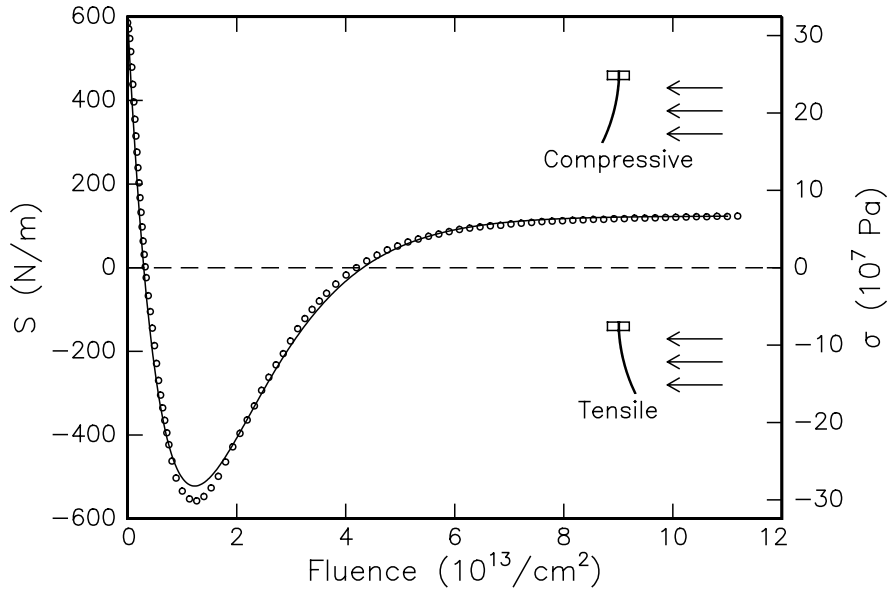


FIGURE 3: The integrated in-plane stress of an SiO_2 film on a Si substrate during irradiation with 4.0 MeV Xe. The right hand axis shows the average local stress. The solid line is a fit according to Eq. (2).

lapsed, and after $1.0 \times 10^{16} / \text{cm}^2$ the surface has deformed so much that the trench is nearly filled.

Figure 3 shows the integrated in-plane stress of a planar film, without trenches, during Xe irradiation at the same energy, but a much lower fluence. The right axis shows the corresponding average local stress. The initial integrated compressive stress ($S_0 = 580 \pm 15 \text{ N/m}$) is caused by the elastic strain due to the difference in thermal contraction of SiO_2 and the Si substrate upon cooling the wafer after oxidation. As the sample is irradiated, the stress first decreases, and becomes tensile. At a fluence of $1.3 \times 10^{13} / \text{cm}^2$ the integrated stress reaches a minimum of -550 N/m . For higher fluences the stress increases and finally saturates at a compressive value of 120 N/m , corresponding to $\sigma = 6.5 \times 10^7 \text{ Pa}$. The maximum implanted Xe concentration is $\sim 20 \text{ ppm}$, so that volume changes due to the implanted Xe can be excluded. The stress behavior was independent of ion flux, in the range of $0.8\text{--}3.1 \times 10^{10} \text{ ions/cm}^2\text{s}$.

Previous wafer-bending studies of SiO_2 during ion irradiation [1,2] have attributed the initial stress decrease to densification of the silica network. Densification is a result of both electronic- and nuclear stopping processes, and has been shown to saturate when $\sim 10^{20} \text{ keV/cm}^3$ is deposited into atomic collisions. Indeed, a Monte Carlo calculation of the implantation damage (TRIM '89) [9] at the observed minimum at $1.3 \times 10^{13} \text{ Xe/cm}^2$ shows that $1 \times 10^{20} \text{ keV/cm}^3$ is deposited in atomic collisions in the silica.

More recent measurements [3] have demonstrated an additional effect: stress in SiO₂ can relax without a density change by radiation-enhanced Newtonian plastic shear flow, in which the strain-rate is proportional to the stress. From these experiments it is inferred that ion irradiation can strongly reduce the effective shear viscosity compared to the thermal value. A similar relaxation is indeed observed in Fig. 3 for fluences $> 1.3 \times 10^{13} / \text{cm}^2$, but in this case the stress becomes compressive again. By viscous flow stress can only relax to zero, therefore in addition to densification and viscous flow, a third process must participate in the behavior. This is attributed to the higher beam energy with respect to that used in Ref. 3.

For very high energy ion irradiation (up to 360 MeV), anisotropic deformation was reported in a variety of amorphous materials [10,11] in which the materials contract along the direction of the beam, and expand in the perpendicular plane. The deformation was found to be non-saturating, and the rate of deformation was linearly dependent on the (electronic) energy loss, with a threshold of $\sim 2 \text{ keV/nm}$. The electronic energy loss for 4.0 MeV Xe ions in SiO₂ is $\sim 2.3 \text{ keV/nm}$, in addition to a nuclear energy loss of $\sim 0.8 \text{ keV/nm}$ [9]. Therefore, we suggest that the same anisotropic deformation found for bulk samples [10,11] plays a role in our thin films. The non-zero saturation in Fig. 3 is ascribed to a dynamic equilibrium determined by the rate of anisotropic deformation (expansion perpendicular to the beam) which increases the in-plane stress, and radiation enhanced flow, which serves to relax the stress. Note that in the 360 MeV experiments on bulk samples the ion range was much larger than the sample thickness, so that the deformation was uniform through the sample. In this case no stress builds up.

To demonstrate the idea of equilibrium, samples with non-equilibrium stress states were prepared by clamping samples in cylindrical armatures [6] with fixed radii of curvature (10.00 cm convex and 7.50 cm concave) and irradiating them with $5 \times 10^{14} \text{ Xe/cm}^2$ at 4.0 MeV. In this way, any changes in density should saturate, and plastic flow should occur, driven by the stress imposed by the armatures. When the samples were removed from the armatures, they had acquired different stress states (see the black dots in Fig. 4), indicating that plasticity indeed had occurred. No curvature was induced in samples clamped in the armatures for a similar length of time without being implanted, indicating that the flow was irradiation-induced rather than thermally activated.

Figure 4 shows the stress of the two ‘set’ samples during subsequent irradiation with 4.0 MeV Xe (circles). The integrated stress of the sample with an initial value of 45 N/m increases to a steady state value of $80 \pm 15 \text{ N/m}$ during irradiation. The stress of the other sample, set at a value of 200 N/m, decreases during irradiation and saturates at $93 \pm 15 \text{ N/m}$, within the error the same saturation value.

RBS shows that the Xe projected range in the $1.85 \mu\text{m}$ thick SiO₂ films, is $1.70 \mu\text{m}$. A fraction of the Xe ions have entered the Si substrate, damaging a $0.18 \mu\text{m}$ thick Si layer. This gives a small contribution to the measured integrated stress [6],

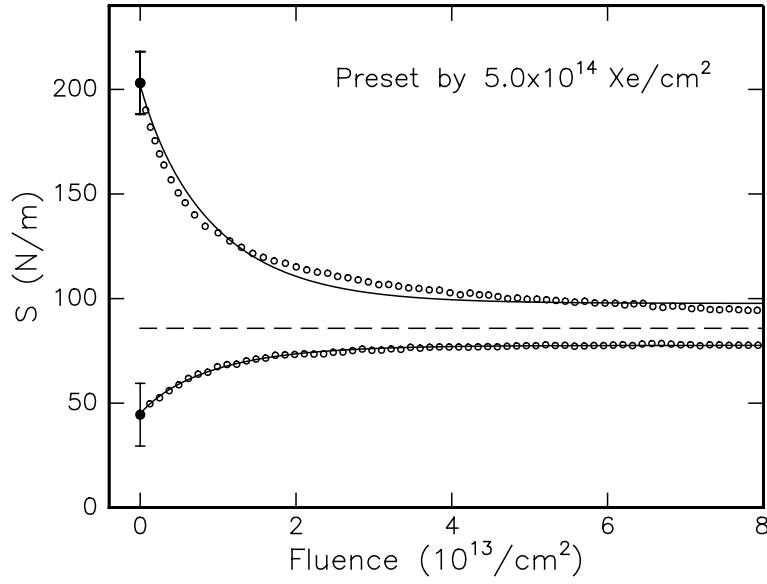


FIGURE 4: The integrated in-plane stress during 4.0 MeV Xe irradiation, of samples which were first set in two different stress states. The ‘set’ stress is indicated by the black dots. The solid lines are fits using Eq. (3). The dashed horizontal line denotes the equilibrium stress value.

which was found to be less than $+30$ N/m in S_{sat} by measuring the substrate curvature after etching the SiO_2 layer from the substrate after irradiation.

Under the assumption that the local stress is uniform through the oxide layer, the integrated in-plane stress in the SiO_2 film as a function of fluence ϕ can be described by a rate equation in which the three radiation induced processes (densification, anisotropic deformation, and radiation induced plastic flow) are included:

$$\frac{dS}{d\phi} = Y_{\text{ox}} t_{\text{ox}} \left(\frac{d\epsilon_{\rho}}{d\phi} + A \right) - \frac{Y_{\text{ox}}}{6\eta_{\text{rad}}} S. \quad (2)$$

Here, t_{ox} is the oxide layer thickness, Y_{ox} the biaxial elastic modulus of SiO_2 ,^b ϵ_{ρ} the strain due to densification, A the strain per ion due to non-saturating anisotropic deformation, and η_{rad} the radiation induced viscosity as defined in Ref. 3. Viscous flow is negatively proportional to the stress. When density changes have saturated, $d\epsilon_{\rho}/d\phi = 0$, the solution to Eq. (2) is

$$S(\phi) = S_{\text{sat}} + (S_0 - S_{\text{sat}}) \exp \left[-\frac{Y_{\text{ox}}}{6\eta_{\text{rad}}} \phi \right], \quad (3)$$

where $S_{\text{sat}} = 6A\eta_{\text{rad}}t_{\text{ox}}$ is the saturation stress. Fits, according to Eq. (3), are given in Fig. 4 by solid lines, and indeed describe the data reasonably well. The fits yield $\eta_{\text{rad}} = (1.67 \pm 0.17) \times 10^{23}$ Pa · ions/cm² (or a shear viscosity of 6×10^{12} Pa · s at

^bWe used $Y_{\text{ox}} = 100$ GPa.

3.1×10^{10} ions/cm²s). This is at least seven decades lower than the pure thermal viscosity at room temperature. The low viscosity presumably results from broken bonds either directly created by the incoming Xe ions, or indirectly by a local heating effect in the vicinity of the ion track. Indeed, such fluid behavior is found in a recent molecular dynamics (MD) simulation of low energy irradiation of Au [12]. The general behavior of these simulations may apply to silica as well. Using S_{sat} and η_{rad} from Fig. 4, the anisotropic deformation constant $A = (5.0 \pm 1.5) \times 10^{-17}$ cm² is derived.

Equation (2) can also be applied to model the behavior in Fig. 3. It is assumed that the densification is described by a damage overlap model, in which the densification rate exponentially decreases to zero, $d\epsilon_{\rho}/d\phi \propto \exp[-\phi/\phi_{\rho}]$, and that η_{rad} is constant. The solid line in Fig. 3 was fitted yielding a saturation density change of $(3.6 \pm 0.6)\%$, with $\phi_{\rho} = 1.0 \times 10^{13}$ /cm², $\eta_{\text{rad}} = (1.67 \pm 0.17) \times 10^{23}$ Pa · ions/cm² and $A = (5.7 \pm 1.5) \times 10^{-17}$ cm². As can be seen, the calculation resembles the measured data quite well. Small deviations for low Xe fluences may be explained by some variation of η_{rad} during densification [3]. The observed density increase agrees with previously established values [1]. The deformation constant and the radiation induced viscosity agree with values found above for Fig. 4. The radiation-induced viscosity is in the same range as the values found in Ref. 3 for irradiations with Si and Au below 800 keV. In absence of viscous flow, the deformation energy per unit length is equal to $Y_{\text{ox}} \cdot A$. In the case of 4.0 MeV Xe irradiation, this is ≈ 4 eV/nm, i.e. 0.1% of the total deposited energy for each ion is stored in the deformation.

An independent measure of A can be obtained from the SEM pictures in Fig. 2. From the relative length change of the 15 μm SiO₂ regions between adjacent trenches in Fig. 2, a lower limit for the in-plane expansion coefficient of $A = (2.9 \pm 0.5) \times 10^{-17}$ cm² can be extracted, which is consistent with the values obtained from Figs. 3 and 4. This leads to the conclusion that both the non-saturating anisotropic expansion seen in Fig. 2 and the final compressive stress observed in Figs. 3 and 4 are caused by the same mechanism. An extrapolation of A values obtained from very high energy experiments on bulk samples at 115 K [11], using the electronic stopping as a scaling parameter, yields $A \sim 3 \times 10^{-17}$ cm².

The deformation in Fig. 2 seems to be most pronounced in the very surface, where the electronic stopping power is high. Electronic stopping causes a local heating of a cylindrical ion track, with a strong temperature gradient perpendicular to the cylinder, which may result in anelastic expansion of the silica. Apparently, the beam-directional cylindrical symmetry, which occurs only at high beam energy, can give rise to anisotropy as observed. Note that a significant fraction of the ion energy is deposited in atomic collisions, which also contributes to the heating effect.

4. Conclusions

In conclusion, densification, anisotropic deformation, and radiation enhanced plastic flow have been observed in thin SiO₂ films at room temperature during 4.0 MeV Xe irradiation. These processes were flux independent in the range of $(0.8 - 3.1) \times 10^{10}$ ions/cm²s. Non-saturating anisotropic deformation is possibly caused by local heating and thermal expansion around the ion tracks. This causes a dramatic deformation of SiO₂ implantation masks, and may be observed for other materials as well.

References

- [1] W. Primak, *Studies in Radiation Effects in Solids* (Gordon and Breach, New York, 1975), Volume 4.
- [2] E. P. EerNisse, *J. Appl. Phys.* **45**, 167 (1974).
- [3] C. A. Volkert and A. Polman, *Mat. Res. Soc. Symp. Proc.* **235**, 3 (1992).
- [4] Part I of this thesis.
- [5] A. Polman, D. C. Jacobson, D. J. Eaglesham, R. C. Kistler, and J. M. Poate, *J. Appl. Phys.* **70**, 3778 (1991).
- [6] C. A. Volkert, *J. Appl. Phys.* **70**, 3521 (1991).
- [7] W. A. Brantley, *J. Appl. Phys.* **44**, 534 (1973).
- [8] P. A. Flinn, D. S. Gardner, and W. D. Nix, *IEEE. Trans. Electron Devices* **ED-34**, 689 (1987).
- [9] J. P. Biersack and L. J. Haggmark, *Nucl. Instrum. Methods* **174**, 257 (1980).
- [10] S. Klaumünzer, *Radiat. Eff.* **110**, 79 (1989).
- [11] A. Benyagoub, S. Löffler, M. Rammensee, and S. Klaumünzer, *Nucl. Instrum. Methods* **B65**, 228 (1992).
- [12] M. Ghaly and R. S. Averback, *Phys. Rev. Lett.* **72**, 364 (1994).

Chapter 8

Ion irradiation induced creation and relaxation of mechanical stress in silica

In-situ wafer curvature measurements were performed to study mechanical stress in amorphous SiO₂ during Xe, Ne, and Er ion irradiation at energies in the range of 0.27 – 4.0 MeV. Three phenomena are observed: network compaction, radiation induced viscous flow, and a non-saturating anisotropic deformation phenomenon. The radiation-induced *viscosity* is shown to be inversely proportional to the energy density deposited into atomic displacements. The relation between radiation induced flow and diffusion is discussed in the context of the Stokes-Einstein relation. Viscous flow serves to relax stress, yet a continuous non-saturating *anisotropic deformation* effect causes the stress in the irradiated layer to saturate at non-zero values: Xe irradiation at an energy below 3.6 MeV results in a tensile saturation stress; for higher energies a compressive stress builds up. These effects are explained in terms of competing bulk and surface deformation processes resulting from local heating of the SiO₂ around the ion tracks. The macroscopic effect of deformation phenomena is illustrated by showing the surface morphology after 4.9 MeV Er irradiation of silica through a contact implantation mask. Finally, an *in-situ* stress study of an alkali-borosilicate glass is presented. In this case a fourth radiation induced effect is observed, namely the generation and annihilation of volume occupying point defects. These defects are shown to anneal out at room temperature, following a broad spectrum of activation energies.

1. Introduction

The effect of ion irradiation on the structure of silica glass has been studied for many years [1,2]. Most of these studies involve irradiation energies up to several hundred keV. More recently, investigations using extremely high energy (~ 100 MeV) irradiation were reported [3,4]. The intermediate energy range (\sim MeV) however, has not been explored. This range is important in for example ion implantation of

optical waveguide materials, where MeV energies are needed to reach the required implantation depths of $2-5\ \mu\text{m}$ [5,6]. It is therefore important to study the response of silica to irradiation at these MeV energies.

Until now, three different radiation induced deformation phenomena are known in SiO_2 : densification [1,7], radiation enhanced viscous flow [8-10], and an anisotropic deformation phenomenon [3,10]. The origin of densification of amorphous SiO_2 is well known [1,2,7]. Atomic collisions cause the SiO_2 ring network to rearrange into smaller, compacter rings. The density increase eventually saturates with fluence. Densification results in a tensile stress if the irradiated region is constrained by a substrate.

Less is known about radiation enhanced viscous flow. Primak first suggested that stress in SiO_2 can relax viscously at room temperature under H and He irradiation [8]. Later Volkert and Polman demonstrated with *in-situ* wafer bending measurements that such radiation enhanced plastic flow in SiO_2 is Newtonian [9], i.e. the strain rate is proportional to the stress. The nature of the defects that cause radiation enhanced viscous flow, and their creation process are investigated in this chapter. Another manifestation of irradiation-induced atomic transport is ion-beam mixing. This phenomenon has been investigated for a number of years [11-13], and is described using a radiation-induced diffusion coefficient. In this chapter the relation between radiation induced flow and diffusion is discussed in terms of a radiation-induced analogue of the Stokes-Einstein relation [14].

In the previous chapter it was shown that a thin-film silica implantation mask collapses completely after irradiation with $1 \times 10^{16}\ \text{Xe}/\text{cm}^2$ at 4.0 MeV [10]. This is due to an anisotropic deformation effect, which is attributed to the high deposited energy density ($\sim 2.3\ \text{keV}/\text{nm}$ electronic and $0.8\ \text{keV}/\text{nm}$ nuclear energy loss). An anisotropic deformation process was also observed during irradiation of thin bulk materials with ions at very high energies (up to 360 MeV) such that the particle range was much higher than the sample thickness, and electronic energy loss was the only stopping process [3,4]. The nature and energy dependence of this deformation phenomenon is studied in this chapter for MeV ion irradiation of SiO_2 films on Si substrates. *In-situ* measurements of the sample curvature during irradiation are used to determine the stress in the irradiated SiO_2 . A large *compressive* saturation stress builds up after $6 \times 10^{13}\ \text{Xe}/\text{cm}^2$ at 4.0 MeV. For energies of 3.5 MeV and lower, a surprising result is obtained: a *tensile* saturation stress is observed. This indicates that an anisotropic deformation with opposite effect occurs.

Measurements are also performed on alkali-borosilicate glass. In addition to the three effects described above (densification, viscous flow, and anisotropic deformation) we find evidence for the creation and room-temperature annihilation of defects that are not related to the defects causing flow.

Finally, the macroscopic effect of the deformation phenomena is illustrated using measurements on sodalime silicate glass that had been implanted with 4.9 MeV Er

ions through a Au contact mask. Optical microscopy and surface profilometry reveal a dramatic change in the surface morphology, which can be explained by the same mechanisms as described above.

2. Experimental

In-situ wafer curvature experiments were performed both on SiO₂ films on a Si substrate, and on commercially available sodalime-borosilicate microscope cover slides (Chance CM5, 150 μm thick). The SiO₂ films, 1.85 μm thick, were obtained by wet thermal oxidation of one side of double-sided polished, undoped, (100) Si wafers of 100 μm thickness at 1100°C. Rectangular pieces (5 × 25 mm²) were clamped at one end to a copper block, leaving the other end free to bend. A He-Ne laser beam was scanned up and down on the back of the sample while the sample was implanted on the front [15].^a From the angle of the reflected beam the radius of curvature was determined during irradiation. In order to obtain measurable reflection from the transparent sodalime-borosilicate, a ~ 20 nm Al layer was evaporated on the backside.

When the thickness of the region modified by the ion beam (t_{ion}) is much smaller than the thickness t_s of the substrate, the integrated in-plane stress S can be calculated from the measured radius of curvature R using the biaxial elastic modulus Y_s of the substrate^b

$$S = \int_0^{t_{\text{ion}}} \sigma(x) dx = \frac{Y_s t_s^2}{6R}. \quad (1)$$

Here, $\sigma(x)$ is the local in-plane stress at a depth x . Deviations of the laser beam due to the vacuum viewport and mirrors limited the resolution of the integrated stress measurements to ± 5 N/m. However, local variations in wafer and oxide thickness limit the absolute determination of the integrated stress to ± 15 N/m. The *average* stress (σ , in Pa) in the irradiated region is obtained from the measured *integrated* stress (in N/m) by $\sigma = S/t_{\text{ion}}$. In this chapter, positive stress values refer to compressive stress, and negative values to tensile stress. The average in-plane elastic strain ϵ can then be calculated from the in-plane stress using the biaxial elastic modulus Y_{ion} of the implanted region $\epsilon = \sigma/Y_{\text{d}}$.^c The thickness of the ion-beam damaged layer t_{ion} is taken to be the projected ion range plus the half width at half maximum of the implantation profile.

Irradiations were done with Ne, Er, and Xe at room temperature with energies ranging from 260 keV to 4.0 MeV. The ion beam was electrostatically scanned

^a See Fig. 1 in Chapter 7.

^b For the (100) Si substrate underneath the SiO₂ film we used $Y_s = 181$ GPa [16], while for the bulk sodalime-borosilicate glass $Y_s = 90$ GPa was used [17].

^c In the case of pure SiO₂, $Y_{\text{ion}} = 100$ GPa was used, while $Y_{\text{ion}} = 90$ GPa was used for the borosilicate glass [17].

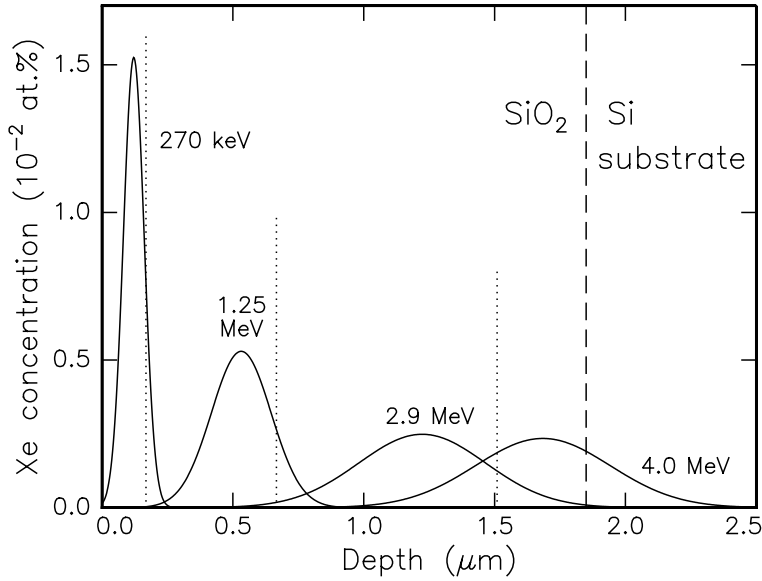


FIGURE 1: Xe concentration profiles in SiO_2 on Si after implantation to 1.0×10^{14} Xe/cm^2 at energies of 0.270, 1.25, 2.90, and 4.0 MeV. The lines are Gaussian fits to the data obtained by 4.0 MeV $^4\text{He}^+$ RBS. The SiO_2 film is 1.85 μm thick. The thickness t_{ion} of the ion beam modified regions (defined in the text) is indicated by dotted vertical lines.

through a $27 \times 27 \text{ mm}^2$ aperture, so that the full width of the sample was irradiated. The maximum ion current density was 20 nA/cm^2 . Ion ranges and SiO_2 film thickness were determined with Rutherford backscattering spectrometry (RBS) using 2.0 and 4.0 MeV $^4\text{He}^+$, and scattering angles of 169° and 160° , respectively. Monte Carlo code TRIM89 was used to calculate nuclear and electronic energy loss [18].

Finally, commercially available 1 mm thick sodalime silicate glass (Fisher Premium) was implanted with 4.9 MeV Er at room temperature to a fluence of $3 \times 10^{16} / \text{cm}^2$, using a gold thin-film implantation contact mask with 15 μm wide etched trenches. After irradiation, the glass surface was studied with optical microscopy and Taly step surface profiling.

3. Pure SiO_2

3.1 Results

First we will present measurements on the SiO_2 films on Si, irradiated with Xe at 0.27, 1.25, 2.9, and 4.0 MeV. Figure 1 shows the Xe concentration profiles for a fluence of $1 \times 10^{14} / \text{cm}^2$. Because of the noise level of the data measured by RBS, we show only the Gaussian profiles that fit the data. As can be seen, in all cases the Xe concentration is lower than 150 ppm, so that volume changes due to the implanted ions can be excluded for such low fluences. The oxide thickness (t_{ox}) was determined

to be $1.85\ \mu\text{m}$. The ion modified region (t_{ion}) extends from the surface to the dotted lines, indicated for each energy. Some of the 4.0 MeV Xe ions have entered the Si substrate.

Figure 2a shows the integrated stress of the SiO_2 films during Xe irradiation as a function of fluence, for different energies. As can be seen, the initial integrated stress before irradiation is $S_0 = 580 \pm 15\ \text{N/m}$, i.e. compressive. This corresponds to an average elastic strain in the SiO_2 film of 3.1×10^{-3} , and originates from the difference in thermal contraction between the SiO_2 and the Si substrate, upon cooling down from 1100°C to room temperature after thermal oxidation. The curves in Fig. 2a are a result of ion-beam induced stress changes, superimposed on a background stress from strained SiO_2 which lies deeper than the irradiated region. This background is equal to $S_0(t_{\text{ox}} - t_{\text{ion}})/t_{\text{ox}}$. By subtracting the background and dividing by t_{ion} , the data in Fig. 2a can be converted to an average stress in the ion-beam damaged layer (Fig. 2b). In this way, curves for different irradiation energies can be compared directly. As can be seen in Fig. 2b, the initial average local stress is $3.0 \times 10^8\ \text{Pa}$ and is identical for all samples. After the ion irradiation is started, the stress first decreases, and becomes tensile. At a fluence of about $1.2 \times 10^{13}\ \text{Xe}/\text{cm}^2$, the stress reaches a minimum, for higher fluences it starts to increase again and eventually saturates. The saturation stress depends on the irradiation energy, and varies from $-(2.6 \pm 0.3) \times 10^8\ \text{Pa}$ (tensile) at 270 keV, to $+(0.45 \pm 0.06) \times 10^8\ \text{Pa}$ at 4.0 MeV (compressive). Similar saturation stresses are also observed in bulk silica glass, where no background subtraction was necessary, as will be shown in Sect. 4.

Figure 1 shows that for the 4.0 MeV Xe irradiation some of the ions have entered the Si substrate. Indeed, channeling RBS showed that a $0.18\ \mu\text{m}$ thick Si layer was damaged near the SiO_2/Si interface. This gives a small positive contribution to the measured integrated stress [15], which was determined by measuring the curvature after etching the SiO_2 layer from the substrate after irradiation. It was found that this Si contribution was less than $30\ \text{N/m}$ ($0.16 \times 10^8\ \text{Pa}$) in the saturation stress, and in Fig. 2b this contribution was subtracted from the 4.0 MeV-data as a linearly increasing background [15].

All reported curves are independent of ion flux (not shown), at least between 0.9 and $3.1 \times 10^{10}\ \text{ions}/\text{cm}^2\text{s}$, indicating that there is no interaction between individual ion-damaged regions. When the ion beam was switched off at any point during the experiment, the stress remained unchanged.

Similar measurements were performed using Ne and Er ions at various energies. Qualitatively, the stress during irradiation showed the same behavior as described above. In the next section, these additional measurements will be used to obtain quantitative information on the stress creation and relaxation mechanisms.

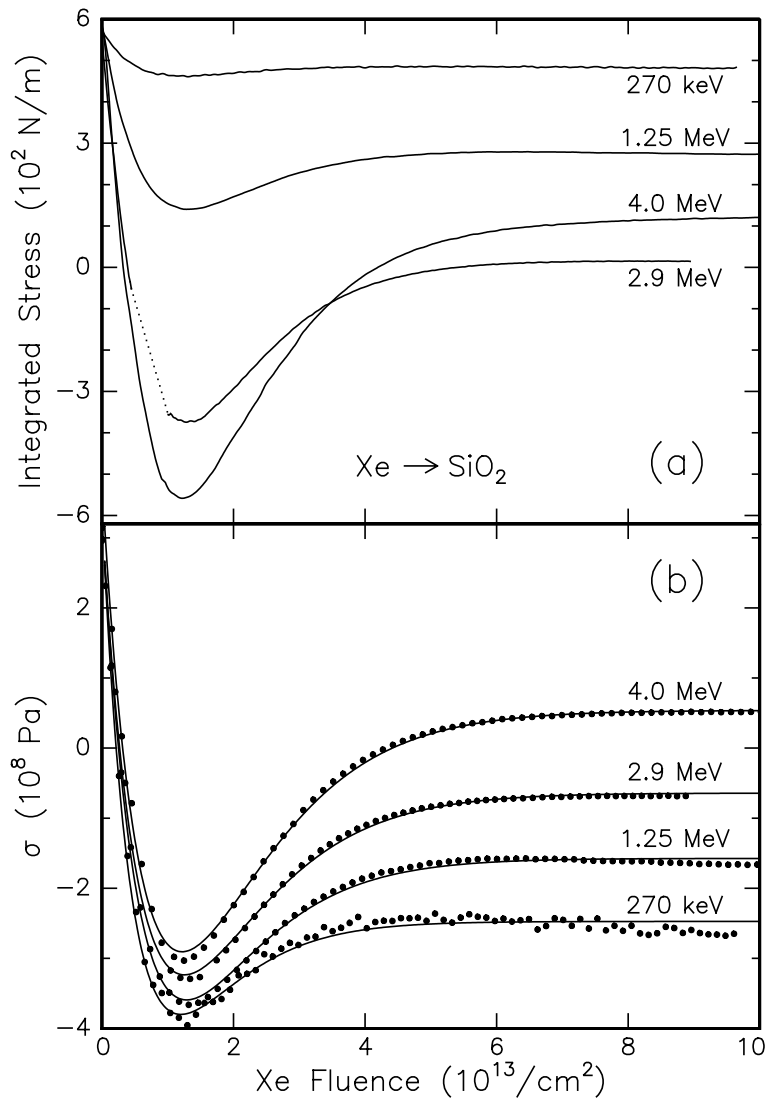


FIGURE 2: (a) Integrated stress in $1.85 \mu\text{m}$ thick SiO_2 films on $\text{Si}(100)$ during Xe irradiation at room temperature, as function of Xe fluence. *In-situ* measurements are shown for beam energies ranging from 0.27 to 4.0 MeV, all at constant Xe flux of 3.1×10^{10} ions/ cm^2s . (b) The same data represented as average stress in the ion-beam modified layer (solid data points). The solid lines are fits using Eq. (3).

3.2 Analysis

As was shown in Chapter 7, the general behavior in Fig. 2 can be described by a model that contains three basic mechanisms: *densification*, radiation enhanced *plastic flow*, and an *anisotropic deformation* mechanism. The rate equation for the average in-plane stress in the irradiated region with respect to fluence ϕ is

$$\frac{d\sigma}{d\phi} = Y_{\text{ion}} \left(\frac{d\epsilon_{\rho}}{d\phi} + A \right) - \frac{Y_{\text{ion}}}{6\eta_{\text{rad}}} \sigma. \quad (2)$$

Here, Y_{ion} is the biaxial elastic modulus of the irradiated layer, ϵ_{ρ} the elastic strain due to density changes, and A the anisotropic deformation rate. Viscous flow is described by a term negatively proportional to the stress and inversely proportional to η_{rad} , the radiation induced viscosity defined as $\eta_{\text{rad}} = \dot{\phi}\eta$, where η is the viscosity, and $\dot{\phi}$ is the ion flux. In this definition of η_{rad} , the areal density of incoming ions replaces the time unit which appears in the thermal viscosity η [9,15]. Note that the lower the viscosity, the ‘softer’ the material. It is assumed that η_{rad} is constant during the irradiation. It is further assumed that densification is described by a damage overlap model [19], in which the strain due to densification (from ρ to $\rho + \Delta\rho$) goes exponentially from zero to $\epsilon_{\text{sat}} = -\Delta\rho/3\rho$, i.e. $\epsilon_{\rho}(\phi) = \epsilon_{\text{sat}}[1 - \exp(-\phi/\phi_{\rho})]$ [1,7], with ϕ_{ρ} a characteristic fluence for densification. The anisotropic deformation rate A is independent of both ϕ and σ , and thus introduces a continuous source for stress. Using these assumptions, the solution of Eq. (2) is

$$\sigma(\phi) = (\sigma_0 - \sigma_{\text{sat}} + D) \exp\left(-\frac{Y_{\text{ion}}}{6\eta_{\text{rad}}}\phi\right) - D \exp(-\phi/\phi_{\rho}) + \sigma_{\text{sat}}, \quad (3)$$

in which $D = 6Y_{\text{ion}}\epsilon_{\text{sat}}\eta_{\text{rad}}/(6\eta_{\text{rad}} - Y_{\text{ion}}\phi_{\rho})$, and σ_0 and σ_{sat} are initial and final saturation stress, respectively. The latter is determined by the product of A and η_{rad} : $\sigma_{\text{sat}} = 6A\eta_{\text{rad}}$.

The drawn lines in Fig. 2b are fits according to Eq. (3). The fits describe the data quite well. The fit values for $\Delta\rho/\rho$ (which follows from ϵ_{sat}), ϕ_{ρ} , η_{rad} , and A are plotted in Fig. 3 as a function of irradiation energy. The only parameter that strongly depends on irradiation energy is the deformation rate A . The parameters for densification and the radiation induced viscosity are almost independent of the Xe energy. We will now discuss these four parameters in more detail.

3.3 Discussion

3.3.1 Densification

The amount of densification (Fig. 3a) is in the range of 2 – 3.5%. This agrees well with previously established values [1,2,7,20]. The characteristic fluence for densification is found to be $\phi_{\rho} = (0.7 - 1.1) \times 10^{13}$ ions/cm² for the Xe irradiations

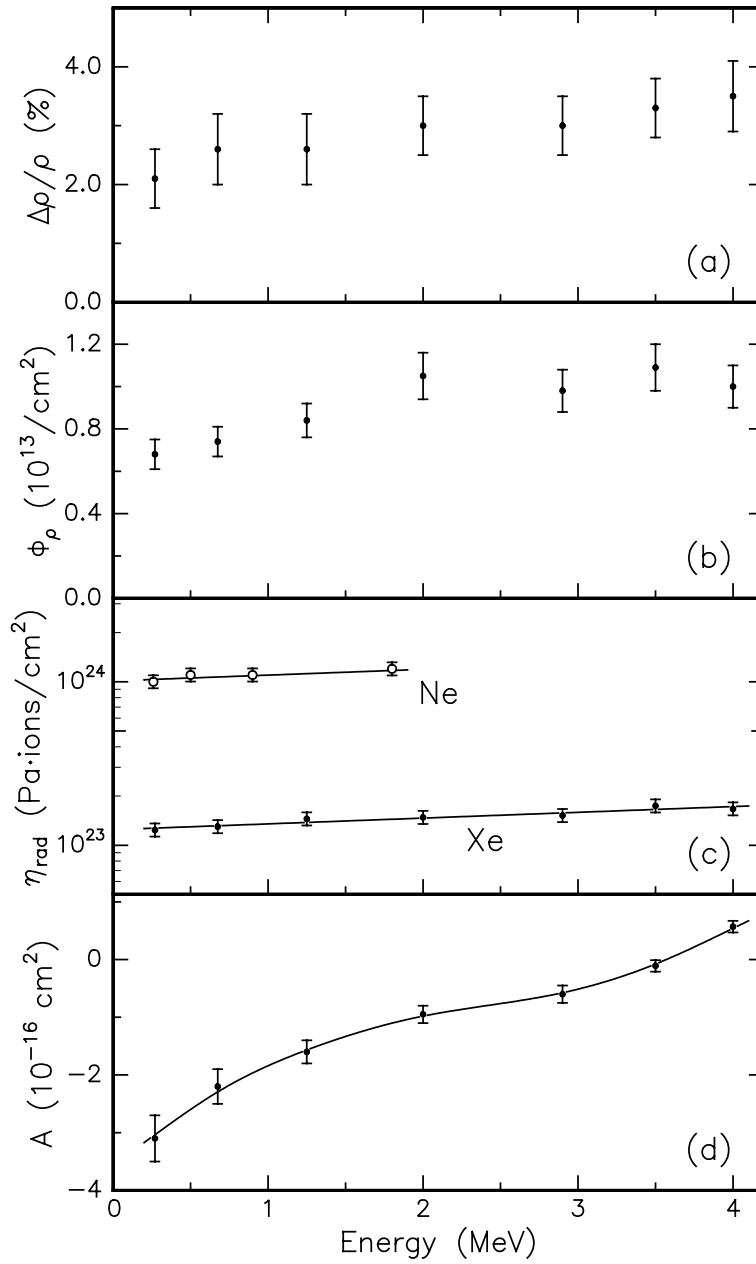


FIGURE 3: Fit parameters from Eq. (3) for the data in Fig. 2b, as a function of Xe irradiation energy (filled data points): (a) density increase, (b) characteristic fluence for densification, (c) radiation induced viscosity, and (d) anisotropic deformation rate. The radiation induced viscosity during Ne irradiation of SiO_2 (circles) is included in (c).

(Fig. 3b). For (0.26–1.8 MeV) Ne and 3.0 MeV Er irradiations, $\phi_\rho = (7.3 \pm 1.0) \times 10^{13}$ and $(0.8 \pm 0.1) \times 10^{13} / \text{cm}^2$ were found respectively. In all cases, the calculated total energy deposited in atomic collisions at the fluence ϕ_ρ is $(1.4 \pm 0.2) \times 10^{20} \text{ keV/cm}^3$, independent of the ion (Ne, Xe, or Er) [18]. This also agrees with previous work, which has shown that the typical energy density required to saturate volume changes in silica is $\sim 10^{20} \text{ keV/cm}^3$ [1,2,7].

3.3.2 Radiation enhanced viscous flow

The values for the Xe irradiation induced viscosity η_{rad} are plotted in Fig. 3c (solid data points). As can be seen, η_{rad} is roughly $1.5 \times 10^{23} \text{ Pa} \cdot \text{ions/cm}^2$, almost independent of irradiation energy in the range of 0.27 – 4.0 MeV. The electronic energy loss varies by a factor of 4 over this energy range, whereas the nuclear energy loss – which is of the same order of magnitude – remains almost constant over this energy range. Therefore, it is concluded that the defects introduced by electronic excitations do not contribute strongly to the viscous flow, and that atomic displacements via nuclear collisions are dominantly responsible for radiation enhanced flow. Additionally, Fig. 3c shows η_{rad} determined for Ne irradiated SiO_2 at energies in the range of 0.26 – 1.8 MeV. The maximum nuclear energy loss for the Ne irradiations is roughly 10 times lower than for Xe. Indeed the value of η_{rad} is almost 10 times higher, and again almost independent of energy.

Figure 4 summarizes the measured radiation induced viscosity η_{rad} in SiO_2 as a function of the maximum nuclear energy loss $F_{\text{n,max}}$, plotted as deposited energy density per ion/cm² for different ions. The values for Ne, Xe and Er are determined in this work. Wafer curvature data for Si and Au were taken from Ref. 9 and analyzed using Eq. (3). From this figure it is clear that η_{rad} decreases (i.e. the SiO_2 becomes more soft) with increasing nuclear energy loss (or ion mass).

The dashed line in Fig. 4 is a linear fit through the data. The slope is -1.1 , showing that the radiation-induced viscosity is almost inversely proportional to the nuclear energy loss. What does this imply for the atomic mechanism for radiation induced viscous flow? Earlier work has shown that there is no ion-flux dependence of η_{rad} . Therefore, there is no interaction between subsequent collision cascades and flow occurs due to defects created within single collision cascades [9]. Thus, the macroscopically defined η_{rad} is a result of a space-time average of the viscosity of SiO_2 at room temperature containing isolated fluid-like spikes. Viscosity is generally described as inversely proportional to the concentration of defects that contribute to viscous flow (flow defects) [22-24]. In the ion-beam case it is important to know the number of flow defects generated per unit length as well as the defect annihilation rate in the cascade. Before any defects have annihilated, the number of flow defects per unit length is proportional to the nuclear energy loss. The experimental result from Fig. 4 is that the averaged viscosity is inversely proportional to the number of

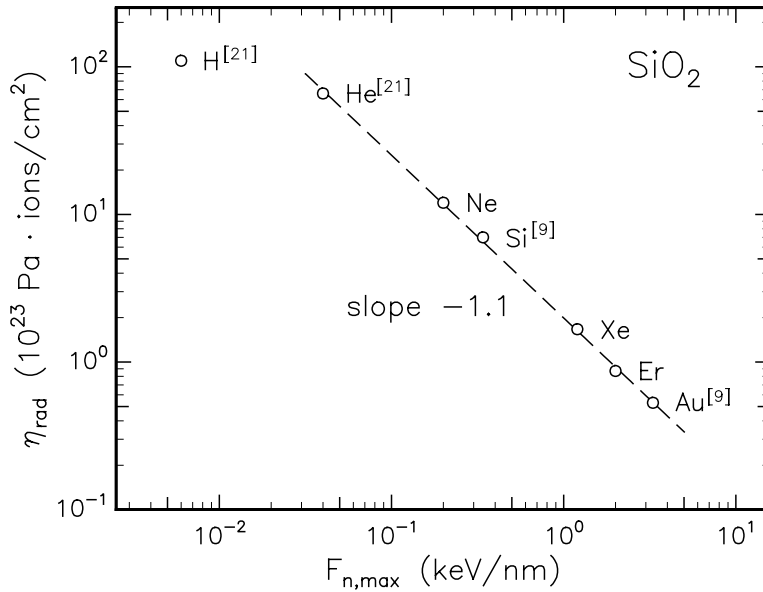


FIGURE 4: Radiation induced viscosity as a function of maximum energy density deposited by nuclear collisions, both plotted on logarithmic scales. Data for Ne, Xe, and Er are from this work, data for Si and Au are derived from Ref. 9, and data for H and He are taken from Ref. 21.

flow defects created per unit length. This implies that the defect annihilation rates must be the same in all the cascades that were used in Fig. 4. To understand this, two cases can be distinguished. 1) The annihilation mechanism is unimolecular. In this case the characteristic lifetime of flow defects is indeed constant. 2) The annihilation mechanism of flow defects is bimolecular, as is often the case for thermal flow in covalent materials [23,25]. The annihilation rate of defects in the cascade then depends on defect *density*. It can only be constant for all irradiation conditions in Fig. 4, if the volume of the cascade scales proportionally with nuclear energy loss. The present experiments cannot distinguish which is the annihilation mechanism of flow defects.

In thermally activated liquids, and in some glassy materials as well, the shear viscosity η is often related to the self diffusivity D by the Stokes-Einstein relation [14], which states that the product ηD is constant at any given temperature. To evaluate this product for radiation-induced atomic transport, we will use the radiation-induced diffusivity which is used to describe ion-beam mixing [11-13]. For room temperature irradiation of SiO₂, ion beam mixing can be described in terms of a purely ballistic effect [11], and the radiation induced diffusivity is given by the phenomenological relation:

$$D_{rad} \equiv \frac{D}{\phi} = 0.067 \frac{F_n R_d^2}{\rho E_d}, \quad (5)$$

where F_n is the energy per unit length deposited into atomic displacements, R_d

the mean range of displaced atoms, ρ the atomic density, and E_d the displacement energy. The ion flux $\dot{\phi}$ is used to relate diffusivity D to radiation-induced diffusivity D_{rad} , analogous to the definition of η_{rad} . As can be seen, D_{rad} is proportional to F_n . From Fig. 4 it was concluded that η_{rad} is proportional to F_n^{-1} . Therefore, the Stokes-Einstein product for radiation induced atomic transport in SiO_2 , $\eta_{\text{rad}}D_{\text{rad}}$, is constant, independent of ion and irradiation energy. This indicates that radiation-induced diffusion and flow are related atomic transport phenomena. Using typical values of $R_d = 10 \text{ \AA}$ and $E_d = 15 \text{ eV}$, we find $\eta_{\text{rad}}D_{\text{rad}} = 8 \times 10^{-11} \text{ N}$. This value can now be used to predict η_{rad} for cases in which D_{rad} is known, and vice versa.

Finally, Fig. 4 also shows values of η_{rad} for H and He irradiation, taken from Ref. 21, which were determined using x-ray reflectivity measurements of radiation induced surface smoothing with $\sim 1 \text{ keV}$ ions. As can be seen, extrapolation of our viscosity data towards low nuclear energy loss for H and He predicts the correct order of magnitude for η_{rad} . This suggests that the flow contribution to ion induced surface smoothing is related to the mechanism of ion beam induced flow from this work. However, the radiation induced viscosity of H does not exactly lie on the dashed line with slope -1.1 . This may be due to differences in collision cascade dimensions or a different role of the surface in the very low energy irradiations.

3.3.3 Anisotropic deformation

In the case of the present irradiations of SiO_2 films, the stress reaches an equilibrium value after $\sim 6 \times 10^{13} \text{ Xe/cm}^2$ (Fig. 2). The final steady state is due to a dynamic equilibrium of a continuous stress generating process, and radiation enhanced flow, which serves to relax stress [10]. Because this stress-generating phenomenon is unsaturable, it cannot be a density change but it must be a continuous anisotropic deformation. In the case of compressive saturation stress (4.0 MeV Xe irradiation), the irradiated SiO_2 expands in-plane and therefore has to shrink normal to the plane because the density is constant [10]; for tensile in-plane saturation stress ($< 3.6 \text{ MeV}$) the opposite is the case.

Figure 5 shows the total deformation effect, plotted as the depth-integrated value of the deformation rate A , as a function of Xe irradiation energy. It shows the negative integrated deformation rate causing tensile stress for energies $< 3.6 \text{ MeV}$, and the positive deformation rate causing compressive stress at 4.0 MeV. In the remainder of this section, we will speculate on the interpretation of these anisotropic deformation effects in terms of a combination of a near-surface phenomenon which causes tensile stress, and a bulk process that causes compressive stress.

The insets in Fig. 5 show schematic suggestions of what would happen in the region where an ion enters the SiO_2 . The insets correspond to low (a), intermediate (b), and high (c) energy irradiations. Inset (a) applies to Xe energies below 1.25 MeV. In this regime the sample becomes more curved for increasing energy,

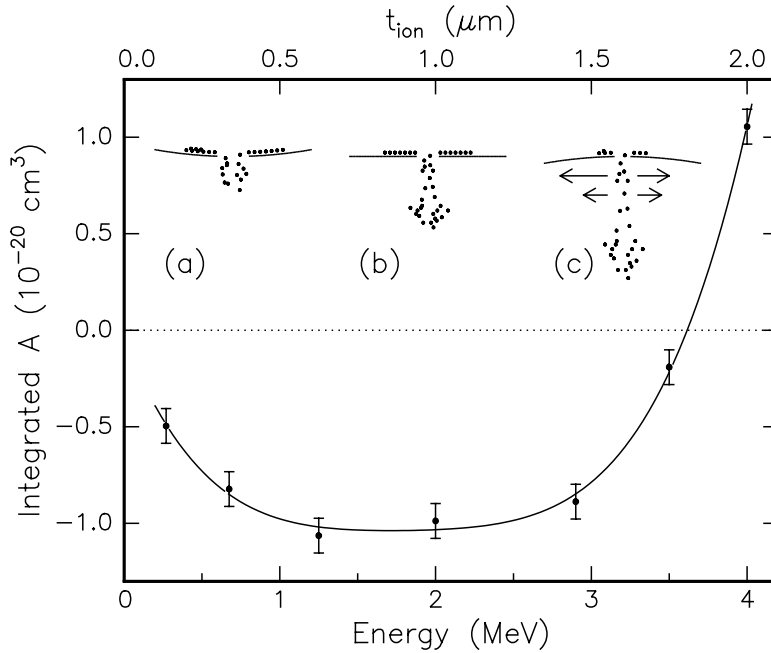


FIGURE 5: Integrated deformation rate, $A \cdot t_{\text{ion}}$, as a function of Xe irradiation energy. t_{ion} is indicated on the top axis. The three insets show how the SiO_2 may react to an incoming energetic ion, for the case of low (a), intermediate (b), and high (c) energy irradiation. The solid dots represent some of the displaced atoms in the cascade. The picture for (a) is derived from a MD simulation in Ref. 26.

bending towards the incoming ion beam. In the direct vicinity of the track where a Xe ion enters the SiO_2 , material is locally heated. This causes some atoms to be forced out of the locally hot region on to the surface, where they may condense. Material from the surrounding SiO_2 will then undergo a force to attempt to fill the vacant space that is left behind, causing a tensile stress as is observed. This idea is consistent with recent molecular dynamics (MD) simulations of 10 and 20 keV Au irradiation of Au, where the nuclear energy loss density in the substrate is comparable to the stopping density in our experiment [26]. These MD simulations show exactly what is sketched in inset (a).

For irradiation energies above 1.25 MeV, a competing process sets in. For these energies, the electronic stopping power near the surface exceeds the nuclear energy loss. The total deposited energy density in the cascade becomes higher, and the large ion range gives rise to a more cylindrically shaped ion track (Figs. 5b and 5c). The locally hot cylindrical region will try to expand, in order to relieve the thermal stress. Due to the cylindrical geometry, a net anisotropic deformation will take place, in which the material expands anelastically in the plane perpendicular to, and consequently shrinks in the direction of the cylindrical axis. This interpretation, which will lead to a compressive saturation stress, is based on a local heating effect.

Earlier work on anisotropic deformation phenomena at > 100 MeV energies has been interpreted in terms of a Coulomb repulsion effect of ionized atoms in SiO_2 [3,27]. More recently it has been suggested that momentum transfer from the incoming ions to the host may explain the observed deformation as well [28].

The wafer curvature technique yields the integrated stress, and consequently the *integrated* deformation rate. Therefore, the net measured deformation rate is determined by the sum of the competing surface contraction and bulk expansion. At ~ 3.6 MeV, where the net effect of deformation on the sample curvature is zero (see Fig. 5b), both effects are equally strong. At 4.0 MeV the in-plane expansion effect is larger than the surface contraction effect, resulting in the situation that the sample bends away from the ion beam (Fig. 5c).

4. Sodalime-borosilicate glass

4.1 Results

Figure 6 shows an RBS spectrum of the sodalime-borosilicate used in the second series of experiments which will be described from here. The spectrum agrees with the specified composition [29]: SiO_2 , Na_2O , CaO , K_2O , B_2O_3 , Al_2O_3 , MgO , TiO_2 , ZnO , Sb_2O_3 , and BaO . Because of the presence of heavy elements it was not possible

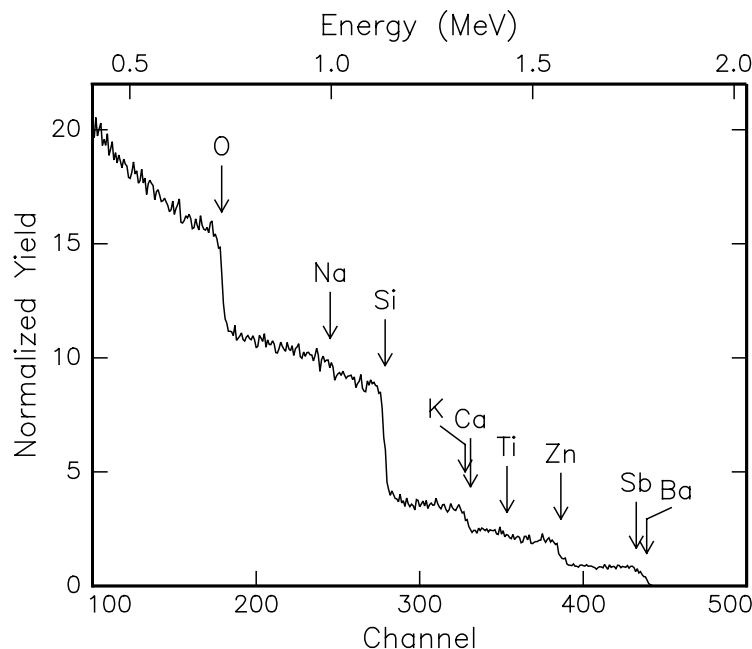


FIGURE 6: RBS spectrum of the used alkali-borosilicate glass (Chance CM5), taken using 2.0 MeV $^4\text{He}^+$. In addition to the indicated elements, B_2O_3 is a specified ingredient.

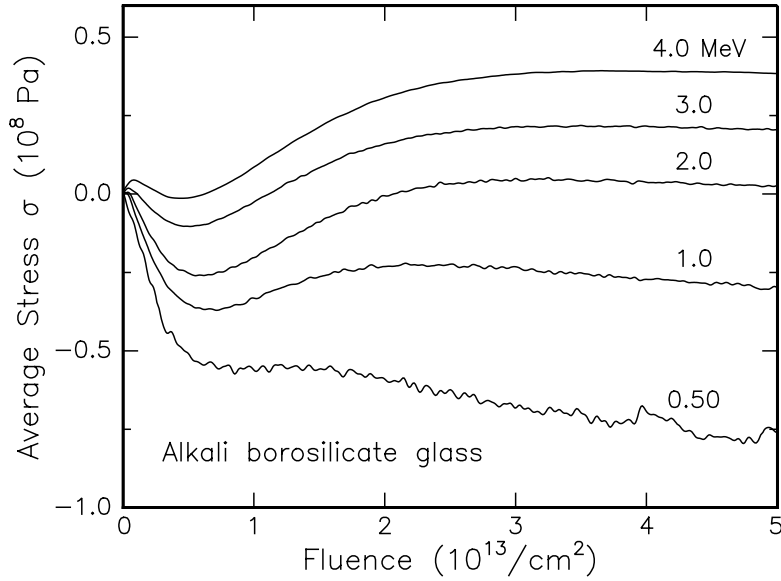


FIGURE 7: *In-situ* measurements of the average local stress σ of alkali-borosilicate glass during irradiation with Xe at energies ranging from 0.50 to 4.0 MeV, using a constant Xe flux of 3.1×10^{10} ions/cm²s.

to determine the Xe implantation profiles with RBS; the profiles were estimated using TRIM89 code.

Figure 7 shows the average local in-plane stress in the irradiated region of this glass for Xe energies in the range from 500 keV to 4.0 MeV. The average stress σ was obtained by dividing the measured integrated stress by $t_{\text{ion}} = 0.25, 0.48, 0.96, 1.44,$ and $1.90 \mu\text{m}$, depending of Xe energy. Prior to irradiation, the bulk samples were uncurved. As the samples are implanted above 1.0 MeV, the stress first shows a slight but rapid increase within the first $\sim 10^{12}$ ions/cm². The average stress then decreases, after which it increases again to finally saturate after $\sim 3 \times 10^{13}$ Xe/cm². For 4.0 MeV Xe irradiation, the saturation stress is $(0.39 \pm 0.04) \times 10^8$ Pa, compressive. The saturation stress decreases with irradiation energy, turning tensile below 2.0 MeV. For 500 keV the tensile saturation stress is $-(0.8 \pm 0.2) \times 10^8$ Pa. Apart from the initial transient, the behavior in Fig. 7 is qualitatively similar to that observed for pure silica in Fig. 2.

Figure 8 shows the integrated in-plane stress S of the alkali-borosilicate glass during irradiation with 4.0 MeV Xe as function of time. At $t = 0$ the irradiation starts, with a constant flux of 3.1×10^{10} ions/cm²s. The curve evolves as described above, until the beam is switched off after 2.1×10^3 s, corresponding to a fluence of 6.5×10^{13} ions/cm². It can be seen that the stress then decreases, first rapidly and then more slowly. This is an important difference compared to the results for SiO₂, where the stress remained at the same level as the beam was switched off. When the ion beam is switched on again, the stress increases very rapidly, and

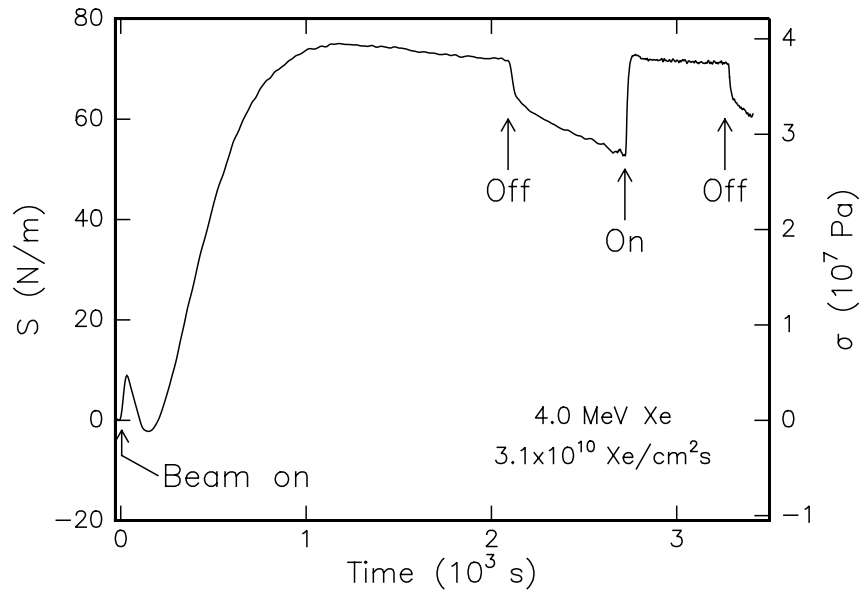


FIGURE 8: Integrated stress of sodalime-borosilicate glass during irradiation with 4.0 MeV Xe as a function of time. The beam was first switched on at $t = 0$. At certain moments, the ion beam with a flux of 3.1×10^{10} /cm²s was stopped and switched on again.

returns to the value it had before stopping the irradiation within 70 s, i.e. a fluence of 2×10^{12} ions/cm². A similar behavior is seen when the ion beam is switched off a second time.

Figure 9 shows the stress decrease after the ion beam was stopped in more detail, and over a longer time scale than in Fig. 8. The data are plotted as a function of time on a logarithmic scale for upto 40 hr. Two cases are shown: one after irradiation with 1.0 MeV Xe, which yields a tensile saturation stress, and one after irradiation with 4.0 MeV Xe which starts at a compressive stress. In both cases the stress continues to become more tensile for times as long as 40 hr. As can be seen, neither the time evolution nor the total change in average stress depends on the preceding irradiation energy, or the sign and magnitude of the stress.

The 'beam on' behavior is shown in more detail in Fig. 10 for two 4.0 MeV Xe fluxes of 1.6 and 3.1×10^{10} ions/cm²s, as a function of fluence. In both cases the beam was switched on after the stress had first relaxed to 60 N/m. As can be seen, the final saturation stress is equal for both irradiation fluxes. A small overshoot is seen for a flux of 3.1×10^{10} /cm²s before reaching equilibrium, whereas for the lower flux the rapid initial stress increase is followed by a slow approach to the equilibrium value. The fact that the same saturation stress is reached for both fluxes indicates that the curvature increase as the beam is switched on is not due to macroscopic beam heating of the sample surface.

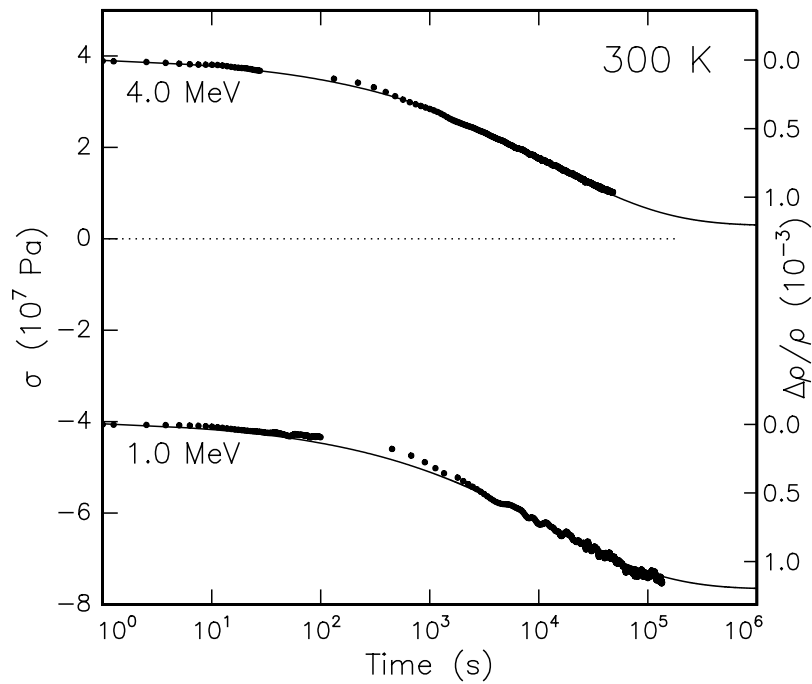


FIGURE 9: Evolution of the average stress after the beam was switched off. Data are plotted as a function of time on a logarithmic scale. The sodalime-borosilicate glass was first irradiated to the saturation stress, using 7×10^{13} Xe/cm² at 4.0 MeV or 1.0 MeV. The drawn lines are fits to a stretched exponential function.

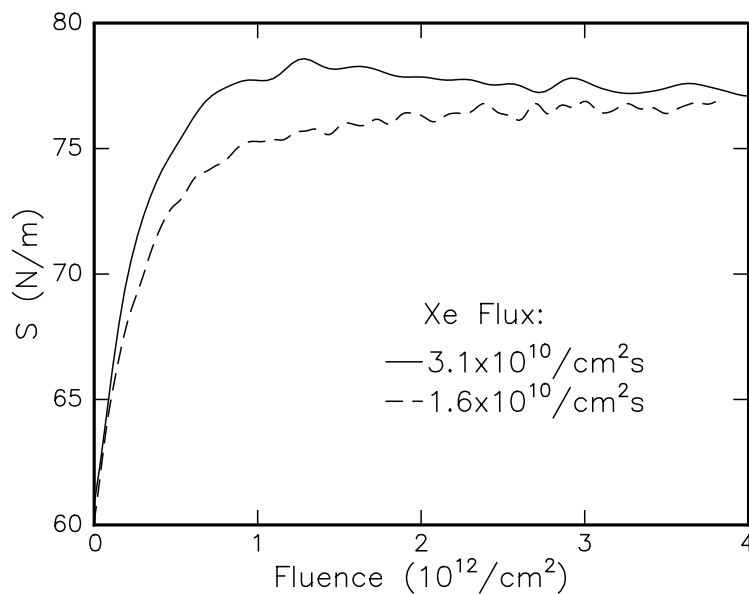


FIGURE 10: Integrated stress measured after the 4.0 MeV Xe beam was switched on. The sample was first irradiated with 7×10^{13} Xe/cm², causing saturation of the stress; then the beam was stopped, and the sample was relaxed to $S = 60$ N/m. Dose rates of 1.6 and 3.1×10^{10} ions/cm²s were used.

4.2 Analysis and Discussion

The most important difference between the stress evolution in the multicomponent glass compared to the behavior in the SiO₂ case (Sect. 3), is the transient behavior as the beam is switched on or off. Figure 9 shows that the direction and magnitude of the stress change as the beam is switched off, are independent of the initial stress (compressive or tensile) or ion energy with which the sample was irradiated. Therefore, this stress change can not be described in terms of viscous flow, as this can only cause relaxation of stress to zero. In fact, the observation that the absolute stress change as a function of time is identical for both curves implies that the stress changes shown in Fig. 9 are purely a result of structural relaxation [30]. Structural relaxation may result in a density increase due to the annihilation of volume occupying (point) defects, causing a more tensile stress, as observed. In the following we will refer to these defects as δ defects. The relative density change can be extracted from the change in average in-plane stress by [7]

$$\frac{\Delta\rho}{\rho} = -\frac{3\Delta\sigma}{Y_{\text{ion}}}, \quad (6)$$

where ρ is the density of the damaged region as the ion beam is switched off. The relative density increase, according to this interpretation, is shown on the right hand axis in Fig. 9; after 40 hr the material has densified by almost 0.12%. This number is in the same range as the observed density decrease of α -quartz due to the creation of E' centers (oxygen vacancies) [2,31]. Therefore, the long-time structural relaxation in irradiated alkali-borosilicate glass may be due to the annihilation of such vacancies. The room temperature annihilation of δ defects may be related to the presence of alkali cations, which are mobile in the network at low temperatures. It is also known that alkali atoms become more mobile during irradiation, and at much higher fluences ($\sim 10^{15}$ /cm²) than used in our experiments, they even show macroscopic depletion below the surface [32,33]. It is interesting to note that the δ defects do not have a large effect on the viscosity of the glass, as no significant viscous flow is observed during the annihilation period of these defects (Fig. 9).

Properties related to structural relaxation in glasses can often be described with a stretched exponential function $\Delta\rho/\rho \propto 1 - \exp[-(t/\tau)^\beta]$. A fit, yielding $\tau = (12.2 \pm 1.7) \times 10^3$ s and $\beta = 0.397 \pm 0.16$ is shown by the solid lines in Fig. 9. Stretched exponential behavior indicates that the relaxation is governed by a distribution of relaxation times [30], which means that the activation energies of the processes that contribute to the density increase are distributed over a continuous spectrum [34,35]. This is a common feature for structural relaxation in amorphous materials like oxides [30] and in amorphous Si [36]. In an isothermal annealing experiment, the time axis reflects the activation energies: at temperature T , relaxation processes with activation energies lower than $Q = kT \ln(\nu t)$ (ν is an attempt frequency) have taken place at time t [34]. Thus, in case of a flat spectrum of activated

processes, the measured property behaves linearly as a function of $\ln(\nu t)$. However, the data in Fig. 9 show a clear change in slope at $t \approx 2.0 \times 10^2$ s. Assuming an attempt frequency $\nu = 10^{12} \text{ s}^{-1}$, this corresponds to a sharp change in the defect annihilation kinetics at $Q = 0.7 \text{ eV}$. This can be a difference in the density of processes with activation energy above or below 0.7 eV , or a difference in the nature of the defects.

Finally, the data in Fig. 10 can be used to obtain information on the creation mechanism of the δ defects. The equilibrium stress value is independent of ion flux. This is due to the fact that once volume changes have saturated, radiation enhanced flow always relaxes the stress to the saturation value of $6A\eta_{\text{rad}}$, independent of density. We fitted an exponential function $S_0 + (S_{\text{sat}} - S_0)(1 - \exp[-\phi/\phi_\delta])$ to the curves in Fig. 10 between 0 and $1.5 \times 10^{12} \text{ Xe/cm}^2$. For both curves this yields $\phi_\delta = 2.6 \times 10^{11} / \text{cm}^2$, whereas the fluxes at which the curves were measured differ a factor of two. This means that the creation rate (in s^{-1}) of the defects is proportional to the ion flux.

The dependence of ϕ_δ on Xe irradiation energy is shown in Fig. 11. Irradiations were performed at energies in the range $0.5 - 4.0 \text{ MeV}$. The silica was first irradiated to a high enough fluence to reach the saturation stress. Then the beam was stopped in order to let the sample stress decrease, and subsequently switched on again in order to determine ϕ_δ . As can be seen, the δ defects are created faster at higher beam energy. The average electronic energy loss in Fig. 11 increases with energy, whereas the average nuclear energy loss is almost constant in the $0.5 - 4.0 \text{ MeV}$ energy range. Electronic energy loss processes therefore contribute to the creation of δ defects. This is not unusual for density changes in alkali silicates [37]. The energy dependence of ϕ_δ is opposite to that observed for ϕ_ρ (Fig. 3b) for densification, which is known to scale predominantly with nuclear energy loss [1,2,7]. This indicates that the density

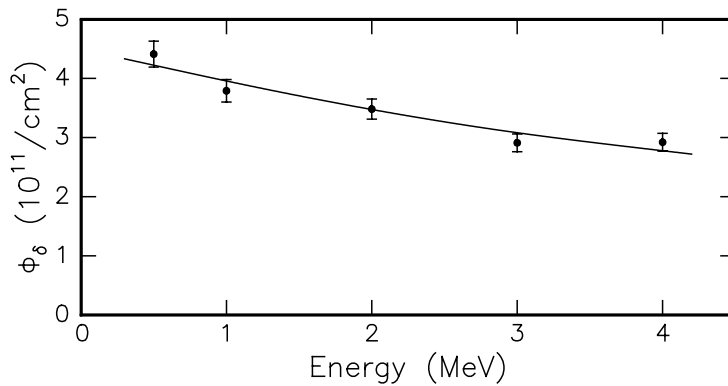


FIGURE 11: Characteristic $(1/e)$ fluences ϕ_δ at which the stress changes to the saturation level as the beam is switched on, as a function of Xe beam energy. ϕ_δ is obtained by fitting exponential functions to data like in Fig. 10.

changes due to network compaction are not related to the density changes due to the creation of δ defects, which is consistent with what is known about E' centers [2].

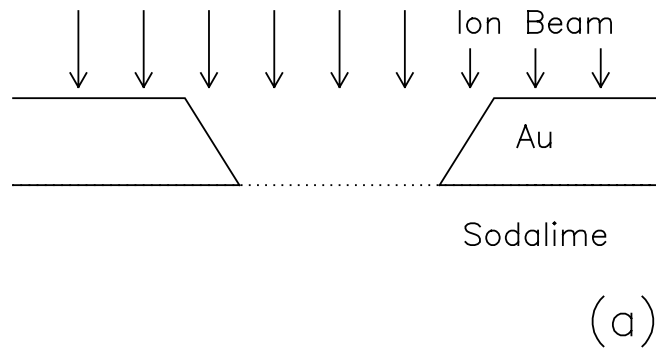
The complete development of the stress in the multicomponent glass (shown in Figs. 7 and 8) can now be understood by a combination of four different processes: *densification* of the silica network, radiation enhanced *viscous flow*, *anisotropic deformation*, and the creation of *volume occupying δ defects*. When the ion beam is first switched on, δ point defects are produced at a relatively high rate, resulting in a small compressive stress (initial increase in Fig. 8). However, at the same time densification of the ring network takes place whereby the glass network is transformed into a more compact state. When the concentration of the δ defects reaches a steady state (i.e. after 20 s in Fig. 8), a net stress decrease is observed due to the ongoing densification. After 0.5×10^{13} ions/cm², see Fig. 7, the net in-plane stress is increasing again (except for the 500 keV data). At this point the network densification has saturated, and no more density changes occur. The stress increase is explained by the net effect of the beam-directional anisotropic deformation and viscous flow. Finally a saturation stress is reached, determined by the balance of the rates of anisotropic deformation and viscous flow: $\sigma_{\text{sat}} = 6A\eta_{\text{rad}}$.

The radiation induced viscosity η_{rad} can be extracted from the data in Fig. 7 by fitting an exponential [see Eq. (3)] through the part of the data that is mainly determined by viscous relaxation, i.e. at fluences above 1.5×10^{13} Xe/cm². This yields $\eta_{\text{rad}} = (0.95 \pm 0.10) \times 10^{23}$ Pa · ions/cm². This value is almost the same as found for pure SiO₂ in Sect. 3. At a flux of 3.1×10^{10} ions/cm²s it corresponds to a viscosity $\eta = 3.1 \times 10^{12}$ Pa · s. This is comparable to the specified thermal viscosity of the alkali-borosilicate glass at 550°C. The specified transformation temperature for this glass is 573°C [29].

Using $\eta_{\text{rad}} = 0.95 \times 10^{23}$ Pa · ions/cm², the anisotropic deformation rate A can be extracted from the saturation stresses in Fig. 7, and ranges from $-(1.4 \pm 0.4) \times 10^{-16}$ to $+(0.667 \pm 0.018) \times 10^{-16}$ cm² for energies ranging from 0.5 to 4.0 MeV. The magnitude of A and its general behavior as a function of energy are very similar to that for pure SiO₂. This implies that the deformation phenomena are a general feature for silica glasses. In fact, these effects may be important in other materials (other glasses, semiconductors) as well.

5. Technological implication

The results of this study have important consequences for mask applications in high energy heavy ion implantation. As an example we will show results of 4.9 MeV Er implantation in sodalime silicate glass at room temperature. Prior to implantation, a 1.0 μm thick gold layer was deposited, after which photolithography and etching was used to define 15 μm wide trenches in the Au to create a contact mask (Fig. 12a) thick enough to fully stop 4.9 MeV Er ions. After irradiation with 3×10^{16} Er/cm²,



(b)

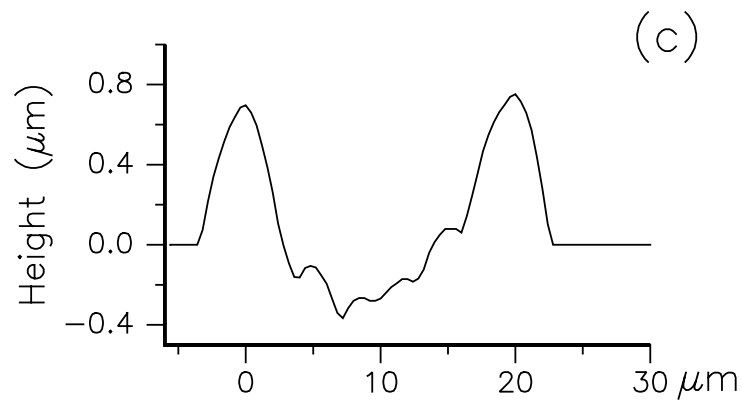


FIGURE 12: (a) Schematic cross section of a Au contact mask with a trench on sodalime glass. (b) Top view of the implanted glass after etching off the Au mask as seen with an optical microscope. (c) Surface profile measured perpendicular to the trench after etching off the Au mask.

the gold was etched off. Figure 12b shows a top view of an implanted stripe. The irradiated surface is very rough. The surface height across the implanted region is shown in Fig. 12c, and shows $0.6 \mu\text{m}$ high rims of material accumulated along the inside of the Au mask, as well as considerable roughness within the rims.

The accumulation of material along the sides of the implanted regions is consistent with the anisotropic deformation effect that is shown to be present during MeV heavy ion irradiation. After densification, the material in the irradiated region undergoes the anisotropic expansion in directions perpendicular to the ion beam, but is constrained on both sides of the trench by glass that is not irradiated. The only way to relax stress in the irradiated region is then to build up on the sides.

The roughness observed within the trench is attributed to the combined effect of expansion, sputtering, surface diffusion, and plastic flow. The surface roughness seems similar to roughening effects seen during low energy irradiation [21].

When such an implantation is used for doping of optical waveguides, this roughness will cause very high and undesirable optical losses due to scattering. Finally, we remark that deformation of silica implantation masks [10] and roughening of silica surfaces is significantly reduced when the implantation is performed around 300°C . This may be a result of a decrease in the radiation induced viscosity, in combination with a possible temperature dependence of the anisotropic deformation phenomenon [4]. The temperature dependences of η_{rad} and A are currently under investigation.

6. Conclusions

When silica glass is ion-irradiated at energies of the order of 1 MeV, three effects are observed: densification, anisotropic deformation, and radiation enhanced viscous flow. Using an empirical model, parameters that describe these processes were obtained.

The radiation-induced viscosity is inversely proportional to the energy lost per unit length in atomic collisions, over a range of at least two orders of magnitude. The product of the radiation-induced viscosity and ballistic diffusivity is constant: $\eta_{\text{rad}} D_{\text{rad}} = 8 \times 10^{-11} \text{ N}$, in an analogous way as in the Stokes-Einstein relation for thermally activated fluids. The data can be used to predict η_{rad} and D_{rad} for a large variety of irradiation conditions. The anisotropic deformation results in a compressive stress at high ($> 3.6 \text{ MeV Xe}$) energies, and in a tensile stress for lower ion energies. These effects are explained in terms of competing bulk and surface deformation processes resulting from local heating of the SiO_2 around the ion tracks.

A fourth irradiation induced phenomenon is observed in a multicomponent alkali-borosilicate glass, and is related to the presence of the high density of network modifiers, such as Na. It shows density changes up to 0.12 %, attributed to irradiation-induced volume occupying point defects, which may be oxygen vacancies (E' cen-

ters). Electronic energy loss processes contribute to the creation of these defects. The defects anneal out at room temperature, according to a broad spectrum of activation energies.

References

- [1] W. Primak, *Studies in Radiation Effects in Solids*, (Gordon and Breach, New York, 1975), Volume 4.
- [2] R. A. B. Devine, Nucl. Instrum. Methods **B91**, 378 (1994).
- [3] S. Klaumünzer, Radiat. Eff. **110**, 79 (1989).
- [4] A. Benyagoub, S. Löffler, M. Rammensee, and S. Klaumünzer, Nucl. Instrum. Methods **B65**, 228 (1992).
- [5] A. Polman, D. C. Jacobson, D. J. Eaglesham, R. C. Kistler, and J. M. Poate, J. Appl. Phys. **70**, 3778 (1991).
- [6] Chapter 5 of this thesis; E. Snoeks, G. N. van den Hoven, A. Polman, B. Hendriksen, M. B. J. Diemeer, and F. Priolo, submitted to J. Opt. Soc. Am. B.
- [7] E. P. EerNisse, J. Appl. Phys. **45**, 167 (1974).
- [8] W. Primak, J. Appl. Phys. **35**, 1342 (1964).
- [9] C. A. Volkert and A. Polman, Mat. Res. Soc. Symp. Proc. **235**, 3 (1992).
- [10] Chapter 7 of this thesis; E. Snoeks, A. Polman, and C. A. Volkert, Appl. Phys. Lett. **65**, 2487 (1994).
- [11] W. Bolse, Mat. Sci. and Eng. R **12**, 53 (1994).
- [12] M. Nastasi and J. W. Mayer, Mat. Sci. and Eng. R **12**, 1 (1994).
- [13] Yang-Tse Cheng, Materials Science Reports **5**, 45 (1990).
- [14] See for instance: P. A. Egelstaff, *An Introduction to the Liquid State* (Oxford University Press, Oxford, 1992.), Chapter 13.
- [15] C. A. Volkert, J. Appl. Phys. **70**, 3521 (1991).
- [16] W. A. Brantley, J. Appl. Phys. **44**, 534 (1973).
- [17] H. Scholze, *Glass* (Springer, Heidelberg, 1990).
- [18] J. P. Biersack and L. J. Haggmark, Nucl. Instrum. Methods **174**, 257 (1980).
- [19] F. F. Morehead, Jr. and B. L. Crowder, Radiat. Eff. **6**, 27 (1970).
- [20] J. Heibei and E. Voges, Phys. Stat. Sol. **57**, 609 (1980).
- [21] T. M. Mayer, E. Chason, and A. J. Howard, J. Appl. Phys. **76**, 1633 (1994).
- [22] N. F. Mott, Philos. Mag. **B56**, 257 (1987).
- [23] H. R. Lillie, J. Am. Ceram. Soc. **16**, 619 (1933).
- [24] S. S. Tsao and F. Spaepen, Acta Metall. **33**, 881 (1985).
- [25] A. Witvrouw and F. Spaepen, J. Appl. Phys. **74**, 7154 (1993).
- [26] M. Ghaly and R. S. Averback, Phys. Rev. Lett. **72**, 364 (1994).
- [27] S. A. Fedotov, V. S. Varichenko, A. M. Zaitsev, M. Ishimaru, Y. Hiroyama, and T. Motooka, Mat. Sci. and Eng. B **29**, 202 (1995).
- [28] L. Cliche, S. Roorda, M. Chicoine, and R. A. Masut, Proc. Ion Beam Modifica-

- tion of Mater., Canberra, Australia 1995, and private communication.
- [29] Data sheets for *Microscope Coverslip glass CM5*, Chance Propper Ltd., Warley, England.
- [30] G. W. Scherer, *Relaxation in Glass and Composites* (Wiley, New York, 1986).
- [31] K. Tanimura, T. Tanaka, and N. Itoh, *Phys. Rev. Lett.* **51**, 423 (1983).
- [32] P. Mazzoldi and G. W. Arnold, in *Ion Beam modification of Insulators*, edited by P. Mazzoldi and G. W. Arnold (Elsevier, Amsterdam, 1987), Chapter 5.
- [33] G. W. Arnold, *Nucl. Instrum. Methods* **B1**, 516 (1984).
- [34] M. R. J. Gibbs, J. E. Evetts, and J. A. Leake, *J. Mater. Sci.* **18**, 278 (1983).
- [35] W. Primak, *Phys. Rev.* **100**, 1677 (1955).
- [36] S. Roorda, W. C. Sinke, J. M. Poate, D. C. Jacobson, S. Dierker, B. S. Dennis, D. J. Eaglesham, F. Spaepen, and P. Fuoss, *Phys. Rev. B* **44**, 3702 (1991).
- [37] G. W. Arnold, *Radiat. Eff.* **98**, 221 (1986).